

**THREE-DIMENSIONAL OPTICAL AND THERMAL
ANALYSIS OF PARABOLIC TROUGH SOLAR
COLLECTOR: A NUMERICAL STUDY**

By

DONGA RAMESH KUMAR
(SAP: 500020671)

**SCHOOL OF ENGINEERING
DEPARTMENT OF MECHANICAL ENGINEERING**

Submitted

IN PARTIAL FULFILLMENT OF THE REQUIREMENTS

FOR THE DEGREE OF

DOCTOR OF PHILOSOPHY

TO



UNIVERSITY WITH A PURPOSE

UNIVERSITY OF PETROLEUM AND ENERGY STUDIES

DEHRADUN

May, 2019

Under the Guidance of

Dr. Suresh Kumar

Professor

Department of Mechanical Engineering

School of Engineering

University of Petroleum and Energy Studies

DECLARATION

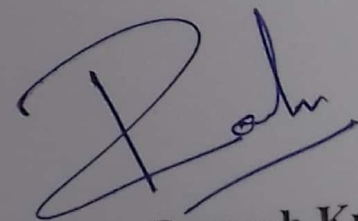
I hereby declare that this submission is my own work and that, to the best of my knowledge and belief, it contains no material previously published or written by another person nor material which has been accepted for the award of any other degree or diploma of the university or other institute of higher learning, except where due acknowledgment has been made in the text.

Donga Ramesh Kumar

May 2019

DECLARATION

I declare that the thesis entitled "Three-Dimensional Optical And Thermal Analysis Of Parabolic Trough Solar Collector: A Numerical Study", has been prepared by me under the guidance of Dr. Suresh Kumar, Professor of Mechanical Engineering, University of Petroleum & Energy Studies. No part of this thesis has formed the basis for the award of any degree or fellowship previously.




Donga Ramesh Kumar

THESIS COMPLETION CERTIFICATE

This is to certify that the thesis on **"Three-Dimensional Optical And Thermal Analysis Of Parabolic Trough Solar Collector: A Numerical Study"** submitted by **Donga Ramesh Kumar** in partial completion of the requirements for the award of the Degree of Doctor of Philosophy (Engineering) is an original work carried out by him under my supervision and guidance.

It is certified that the work has not been submitted anywhere else for the award of any other diploma or degree of this or any other University.


13.05.2019

Internal Guide: Dr. Suresh Kumar
Professor
Department of Mechanical Engineering
School of Engineering
University of Petroleum and Energy Studies
Dehradun.

CORPORATE OFFICE: 210, 2nd Floor,
Oshia Industrial Estate, Phase III,
New Delhi - 110 020, India
P: +91 11 47730151-53, 46022691/5
F: +91 11 47730154

ENERGY ACRES: Bisholi Via
Prem Nagar, Dehradun - 248 007
Uttarakhand, India
T: +91 135 2770137, 2776053/54/91, 2776201
F: +91 135 2776090/95

KNOWLEDGE ACRES: Kandoli Via
Prem Nagar, Dehradun - 248 007
Uttarakhand, India
T: +91 8771979021/2/3, 7066011775

upes.ac.in

ACKNOWLEDGMENT

I take this opportunity to express my sincere thanks to my supervisor **Dr. Suresh Kumar** for his guidance and support. I would also like to express my gratitude towards him for showing confidence in me by giving me a complete freedom to choose my own working path from topic selection to thesis completion. It was a privilege to have a great experience working under him in a cordial environment.

I am very much thankful to the University of petroleum and energy studies, for providing me the opportunity of pursuing Ph.D. in a peaceful environment. I would like to give special thanks to Dr. Abhay Kumar for his pleasant company and support.

In the end, I would like to acknowledge my wife, children, brother and sisters. Without their support, this work would not have been possible.

Donga Ramesh Kumar

TABLE OF CONTENTS

DECLARATION	i
THESIS COMPLETION CERTIFICATE.....	ii
ACKNOWLEDGMENT.....	iii
TABLE OF CONTENTS.....	iv
EXECUTIVE SUMMARY	vii
LIST OF SYMBOLS	x
LIST OF ABBREVIATIONS.....	xii
LIST OF FIGURES	xiii
LIST OF TABLES	xvii
CHAPTER 1 INTRODUCTION	1
1.1 Parabolic trough collector.....	3
1.1.1 Geometry of PTC	4
1.1.2 Heat Collection Element.....	5
1.2 Concentration ratio	6
1.3 Sun Tracking System.....	7
1.4 Heat transfer fluid	9
1.5 Efficiency of PTC	10
1.5.1 Optical losses.....	11
1.5.1.1 Optical efficiency	11
1.5.2 Thermal losses	12
1.5.2.1 Thermal efficiency	12
1.6 Thesis organization.....	13
CHAPTER 2 LITERATURE SURVEY.....	15
2.1 Optical and geometrical errors.....	15
2.1.1 Slope error	16

2.1.2 Tracking error	17
2.1.3 Absorber tube misalignment.....	18
2.2 Improving the heat transfer in the absorber tube	21
2.3 Improving the concentration ratio	22
2.4 Optical analysis.....	24
2.5 Thermal analysis	25
CHAPTER 3 NUMERICAL METHODOLOGY	27
3.1 Optical analysis.....	27
3.2 Thermal analysis	28
3.2.1 Governing equations.....	28
3.2.2 Simulation assumptions.....	31
3.2.3 Boundary conditions.....	32
3.2.4 Numerical simulation.	33
3.3 Validation	34
3.3.1 Validation of the optical analysis	34
3.3.2 Validation of the thermal analysis	35
CHAPTER 4 EFFECT OF ABSORBER TUBE MISALIGNMENT IN LS-2 COLLECTOR.....	37
4.1 Optical analysis.....	38
4.2 Thermal analysis	39
4.3 Results and discussion	40
4.3.1 Circumferential distribution of heat flux on the absorber tube	40
4.3.2 Optical efficiency of PTC.....	45
4.3.3 Receiver thermal performance	46
4.3.3.1 Streamlines and temperature contours	48
4.3.3.2 Circumferential distribution of temperature on the absorber tube	50

4.3.3.3 Collector efficiency	54
CHAPTER 5 EFFECT OF ABSORBER TUBE MISALIGNMENT AND SLOPE ERROR IN SENER TROUGH -2	58
5.1 Optical analysis.....	59
5.2 Thermal analysis	59
5.3 Results and discussion	60
5.3.1 Intercept factor.....	60
5.3.2 Heat flux distribution over the absorber tube	62
5.3.3 Temperature distributions in the absorber tube	65
5.3.4 Collector efficiency	67
CHAPTER 6 HEAT TRANSFER ENHANCEMENT IN PTC USING FINNED ABSORBER TUBE	73
6.1 Optical analysis.....	74
6.2 Thermal analysis	75
6.3 Results and discussion	76
CHAPTER 7 RHOMBUS TUBE ABSORBER	82
7.1 Application of edge ray principle	85
7.2 Dimensions of the rhombus tube absorber.	88
7.3 Comparison of results	89
CHAPTER 8 CONCLUSION AND FUTURE RESEARCH	95
8.1 Conclusion	95
8.2 Future Research	100

EXECUTIVE SUMMARY

Global warming issues and limited availability of conventional fuels leads the world to look for alternative energy sources. The energy from the SUN is abundant and free. It is also clean energy, as it does not produce any greenhouse gases. Concentrated solar power is one of the technique to harness solar energy. In which the solar energy is harnessed by concentrating a large number of sun rays on to a smaller receiver to achieve high operating temperatures. The high operating temperatures result in high thermodynamic efficiency. Parabolic trough collector (PTC) technology is well-commercialized electricity generation technology among the different concentrated solar power technologies available today. The efficiency of the PTC can be increased by improving the heat transfer in the absorber tube and/or by improving the concentration ratio.

To design a high efficient PTC, the optical, thermal and mechanical properties of the PTC components are vital. In practical conditions, although the properties of the PTC components are at the design values, the overall efficiency of the PTC is always below its designed value because of the optical and/or geometrical errors present in the PTC system. These errors occur during installation/operation of the PTC system. The high precision installation methods to avoid those errors are very expensive and complex. The important errors, which greatly affect the performance of the PTC, are curvature precision of the reflective (concentrating) mirror and absorber tube misalignment

This work presents the performance of PTC under the influence of absorber tube misalignment and reflector surface slope error. Optical and thermal performance of two different PTCs has been evaluated. Optical analysis

of the PTC has been done by using Monte Carlo ray tracing method in the SolTrace Software. Finite volume method has been used for the thermal analysis. Variable local heat flux, on the absorber tube, obtained from ray tracing simulations has been incorporated in finite volume method. The study has been conducted for LS 2 trough with 70 mm diameter absorber tube and for Sener trough 2 with two different diameters of the absorber tube, 70 mm and 80 mm. Simulations have been done for slope error and mass flow rate in the range of 0 to 3 mrad and 1 to 6 kg s⁻¹ respectively. The absorber tube misalignment up to 30 mm and each in two directions i.e. along the optical axis and lateral direction has been considered of the LS 2 collector. The intercept factor, Optical efficiency, temperature gradients in the absorber tube, thermal efficiency and overall collector efficiency of the PTC have been evaluated. It is found from the results that collector performance is affected by absorber tube misalignment, mirror slope error, and absorber tube diameter. It has been studied that intercept factor decreases by up to 11% under the influence of absorber tube misalignment by and slope error for 70 mm diameter absorber tube. Results also indicate that overall collector efficiency decreases by up to 11 % for 70 mm diameter tube with absorber tube dislocation in the presence of slope error.

This study also presents the improvement of heat transfer inside the absorber tube using fins. Longitudinal fins are employed inside the absorber tube of a PTC to increase the convective heat transfer. The PTC having 5 m aperture width and 1.84 m focal length with an absorber tube of 70 mm outer diameter is considered for the study. Results of a parametric study conducted on the conventional receiver and finned tube receiver, for a range of Re from 0.25×10^5 to 2.82×10^5 are compared. A significant improvement in heat transfer

has been observed for finned tube absorber. The maximum improvement in the Nusselt number is 40.1% and the maximum value of performance evaluation criteria for the tubular receiver is found to be 1.28 at Reynolds number 2.82×10^5 .

In this work, rhombus tube absorber tube has been proposed to improve the concentration ratio of the PTC. The concentration ratio of the PTC using rhombus tube absorber has been estimated and presented. An analytical technique has been developed to determine the optimum size of the rhombus tube for given trough dimensions. The optimum size of the rhombus tube absorber is 13.8% smaller than the circular tube absorber for the LS3 trough with no change in intercept factor. The maximum improvement in the concentration ratio is found to be 31.5% for the troughs with rim angle 90° in comparison to circular tube absorber. Results also indicate that rhombus tube absorber can be employed for a range of rim angle 75 to 90 degree.

LIST OF SYMBOLS

α_r	: absorptivity of the absorber tube
ϵ_{ao}	: emissivity of absorber coating
ρ_m	: mirror reflectivity
ρ_r	: absorber tube reflectivity
ρ_g	: glass tube reflectivity
σ_x	: normalized receiver misalignment in the x-direction
σ_y	: normalized receiver misalignment in the y-direction
ϕ_r	: rim angle (degrees)
τ_g	: glass tube transmissivity
τ_m	: mirror transmissivity
η_c	: collector efficiency
η_o	: optical efficiency
c_p	: specific heat of HTF ($J\ kg^{-1}\ K^{-1}$)
d_{ai}	: absorber tube inner diameter (mm)
d_{ao}	: absorber tube outer diameter (mm)
d_{ri}	: glass tube inner diameter (mm)
d_{ro}	: glass tube outer diameter (mm)
F	: focal length (m)
h	: heat transfer coefficient ($W\ m^{-2}\ K^{-1}$)
I	: direct normal irradiance ($W\ m^{-2}$)
L	: length of receiver tube (m)
\dot{m}	: HTF mass flow rate ($kg\ s^{-1}$)
q	: local heat flux on an absorber tube ($W\ m^{-2}$)
Re	: Reynolds number

T	: temperature (K)
T_a	: ambient air temperature (K)
T_{ao}	: absorber tube surface temperature (K)
T_{in}	: inlet temperature of HTF (K)
T_{max}	: maximum temperature on an absorber tube (K)
T_{out}	: outlet temperature of HTF (K)
T_{sky}	: external radiation temperature (K)
\bar{T}	: average temperature of HTF at a cross-section (K)
ΔT	: difference of maximum and minimum temperature on an absorber tube (K)
Δx	: offset of the receiver from focus in the x-direction (m)
Δy	: offset of the receiver from focus in the y-direction (m)
V_w	: wind velocity ($m\ s^{-1}$)
Q_c	: solar energy absorbed by HTF (W)
Q_{lost}	: heat loss (W)
w	: aperture width (m)

LIST OF ABBREVIATIONS

CR	: concentration ratio
CSP	: concentrated solar power
DNI	: direct normal irradiation
FVM	: finite volume method
HCE	: heat collection element
HTF	: heat transfer fluid
LCR	: local concentration ratio
MCRT	: Monte Carlo ray tracing
PTC	: parabolic trough collector

LIST OF FIGURES

Fig. 1.1 Schematic of the PTC solar power plant [8].....	2
Fig. 1.2 Kramer junction SEGS 3-7 plant, California. [9].....	3
Fig. 1.3 Parabolic trough collector [11]	4
Fig. 1.4 Cross-sectional view of the PTC	5
Fig. 1.5 Cross sectional view of the HCE.....	6
Fig. 1.6 Single axis tracking of PTC [13]	8
Fig. 1.7 Heat flow in the HCE	12
Fig. 2.1 Slope error	17
Fig. 2.2 Tracking error	18
Fig. 2.3 Absorber tube misalignment.....	19
Fig. 2.4 Visualization of ray tracing with secondary mirrors [56-59]	23
Fig. 3.1 Sample ray tracing simulation in SolTrace.....	28
Fig. 3.2 Validation of the optical analysis	35
Fig. 4.1 Absorber tube misalignment.....	38
Fig. 4.2 Mesh of HCE	40
Fig. 4.3 Heat flux distribution over the circumference of absorber tube for absorber tube misalignments $\Delta y = -10$ mm and $\Delta x = 10$ mm	41
Fig. 4.4 Heat flux distribution over the circumference of absorber tube for absorber tube misalignments $\Delta y = -30$ to 30 mm and $\Delta x = 0$	42
Fig. 4.5 Heat flux distribution over the circumference of absorber tube for receiver position errors $\Delta y = -30$ to 30 mm and $\Delta x = 10$ mm	43
Fig. 4.6 Heat flux distribution over the circumference of absorber tube for receiver position errors $\Delta y = -30$ to 30 mm and $\Delta x = 20$ mm	44

Fig. 4.7 Heat flux distribution over the circumference of absorber tube for receiver position errors $\Delta y = -30$ to 30 mm and $\Delta x = 30$ mm	44
Fig. 4.8 Optical efficiency for $\Delta x = 0$ to 30 mm and $\Delta y = -30$ to 30 mm	46
Fig. 4.9 Velocity profiles at different z locations for receiver position errors $\Delta x = \Delta y = 0$	47
Fig. 4.10 Circumferential distribution of temperature on absorber tube at $z = 1, 2, 3$ and 4 m for $\Delta x = \Delta y = 0$	47
Fig. 4.11 Temperature contours and streamlines at the outlet of the absorber tube.....	50
Fig. 4.12 Circumferential distribution of temperature on the outer surface of the absorber tube at $z = 4$ m for inlet temperature 373 K, $\Delta y = -30$ to 30 mm and $\Delta x = 0$ mm.....	52
Fig. 4.13 Circumferential distribution of temperature on the outer surface of the absorber tube at $z = 4$ m for inlet temperature 373 K, $\Delta y = -30$ mm to 30 mm and $\Delta x = 10$ mm	52
Fig. 4.14 Circumferential distribution of temperature on the outer surface of the absorber tube at $z = 4$ m for inlet temperature 373 K, $\Delta y = -30$ mm to 30 mm and $\Delta x = 20$ mm	53
Fig. 4.15 Circumferential distribution of temperature on the outer surface of the absorber tube at $z = 4$ m for inlet temperature 373 K, $\Delta y = -30$ mm to 30 mm and $\Delta x = 30$ mm	53
Fig. 4.16 Collector efficiency for $\Delta x = 0$ to 30 mm and $\Delta y = -30$ to 30 mm	55
Fig. 4.17 Variation of collector efficiency with respect to inlet HTF temperature for $\Delta y = -30$ to 30 mm and $\Delta x = 0$	56

Fig. 4.18 Variation of collector efficiency with respect to inlet HTF temperature for $\Delta y = -30$ to 30 mm and $\Delta x = 10$ mm	56
Fig. 4.19 Variation of collector efficiency with respect to inlet HTF temperature for $\Delta y = -30$ to 30 mm and $\Delta x = 20$ mm	57
Fig. 4.20 Variation of collector efficiency with respect to inlet HTF temperature for $\Delta y = -30$ to 30 mm and $\Delta x = 30$ mm	57
Fig. 5.1 Mesh of HCE	60
Fig. 5.2 Variation of intercept factor with absorber tube misalignment and slope error for $d_{ato} = 80$ mm	62
Fig. 5.3 Variation of intercept factor with absorber tube misalignment and slope error for $d_{ato} = 70$ mm	62
Fig. 5.4 Distribution of heat flux over the absorber tube for $\Delta x = 0$ and $\Delta y = 0$	63
Fig. 5.5 Distribution of heat flux over the absorber tube for $\sigma = 3$ mrad at $\Delta x = 0$	64
Fig. 5.6 Distribution of heat flux over the absorber tube for $\sigma = 3$ mrad at $\Delta y = 0$	65
Fig. 5.7 Distribution of temperature in the absorber tube for $Re = 2.76 \times 10^5$, $T_{in} = 650$ K and $d_{ato} = 80$ mm (slope error (σ) is in mrad, Δx and Δy are in mm)	67
Fig. 5.8 Collector thermal efficiency Vs absorber tube misalignment for $d_{ato} = 80$ mm	69
Fig. 5.9 Collector thermal efficiency Vs absorber tube misalignment for $d_{ato} = 70$ mm	69
Fig. 5.10 Overall collector efficiency Vs absorber tube misalignment for $d_{ato} = 80$ mm	70

Fig. 5.11 Overall collector efficiency Vs absorber tube misalignment for $d_{\text{ato}} = 70$ mm	70
Fig. 5.12 Temperature gradient in the absorber tube Vs. Re for 80 mm diameter absorber tube at $\sigma = 3$ mrad,	72
Fig. 6.1 Cross sectional view of receiver (a) AT1 (b) AT2 (c) AT3	74
Fig. 6.2 Boundary conditions and mesh of PTC receiver (a) boundary conditions (b) AT1 (c) AT2 (d) AT3	76
Fig. 6.3 Distribution of heat flux over absorber tube.....	77
Fig. 6.4 Temperature distribution over (a) AT1 (b) AT2 (c) AT3.....	78
Fig. 6.5 Variation of Nu and f with Reynolds number	80
Fig. 6.6 Variation of PEC with Reynolds number.	81
Fig. 7.1 Cross section view of the parabolic trough collector.	82
Fig. 7.2 Ray projections from the mirror.	83
Fig. 7.3 Schematic of rhombus tube absorber.....	84
Fig. 7.4 Comparison of the concentration ratio of rhombus tube absorber with circular tube absorber for the LS3 collector, $F = 1.7\text{m}$; $\theta = 0.69^\circ$	90
Fig. 7.5 Intercept factor and average flux Vs specularity error at tracking error zero.....	91
Fig. 7.6 Intercept factor and average flux Vs tracking error at specularity error of 3 mrad.	92
Fig. 7.7 Variation of the local heat flux over the absorber tube with specularity error at tracking error zero	93
Fig. 7.8 Variation of the local heat flux over the absorber tube with tracking error at specularity error of 3 mrad.	94

LIST OF TABLES

Table 1.1 Selective coatings [7].....	5
Table 1.2 Correlations for the HTF properties.....	10
Table 3.1 Validation of the present study with experimental data	36
Table 4.1 Dimensions of the LS-2 collector.	37
Table 4.2 Optical properties of the LS-2 collector	38
Table 5.1 Parameters of the Sener Trough 2.....	58
Table 6.1 Geometrical properties of the PTC system	73
Table 6.2 Optical properties of the PTC system [90]	75
Table 7.1 CR of commercially available troughs with circular tube absorber and rhombus tube absorber for the same acceptance angle	89

CHAPTER 1

INTRODUCTION

Global energy demand is increasing day by day to meet the electricity, heating and cooling requirements of society. Presently, the majority of energy demand is met by fossil fuels like natural gas, coal, and oil. However, the fossil fuels release greenhouse gases and its availability is limited. In order to meet the increasing global energy demand and combating global warming, it is important to explore renewable energy sources like solar, wind, hydro, geothermal and biomass. Among renewable energy sources, solar energy has the greatest potential to meet global energy demand.

Solar energy is abundant and it is available free of cost. It is also clean energy as it does not release any greenhouse gases [1]. Solar energy is being used in wide applications such as electric power generation, water heating, air heating, desalination processes, refrigeration, air conditioning, industrial processes heating, and food processing [2-4]. Photovoltaic (PV) and concentrated solar power (CSP) are two widely used technologies to harness solar energy for electric power generation [5]. In photovoltaics, the SUN light is directly converted into electricity by using semiconducting materials. In the concentrated solar power technology, solar energy is concentrated on a smaller area of the receiver by using reflectors [6]. The thermal energy of SUN rays is converted into heat in the receiver, which in turn is used to run the heat engines to generate the electricity [7].

CSP technologies being commercialized are solar tower, linear Fresnel collector, parabolic dish collector, and parabolic trough collector. Among these

parabolic trough collector (PTC) technology is well developed and most economical [7]. Fig. 1.1 shows the schematic of the typical PTC power plant. A PTC power plant comprises a PTC solar field, steam boiler, steam turbine, condenser, generator, and thermal energy storage system.

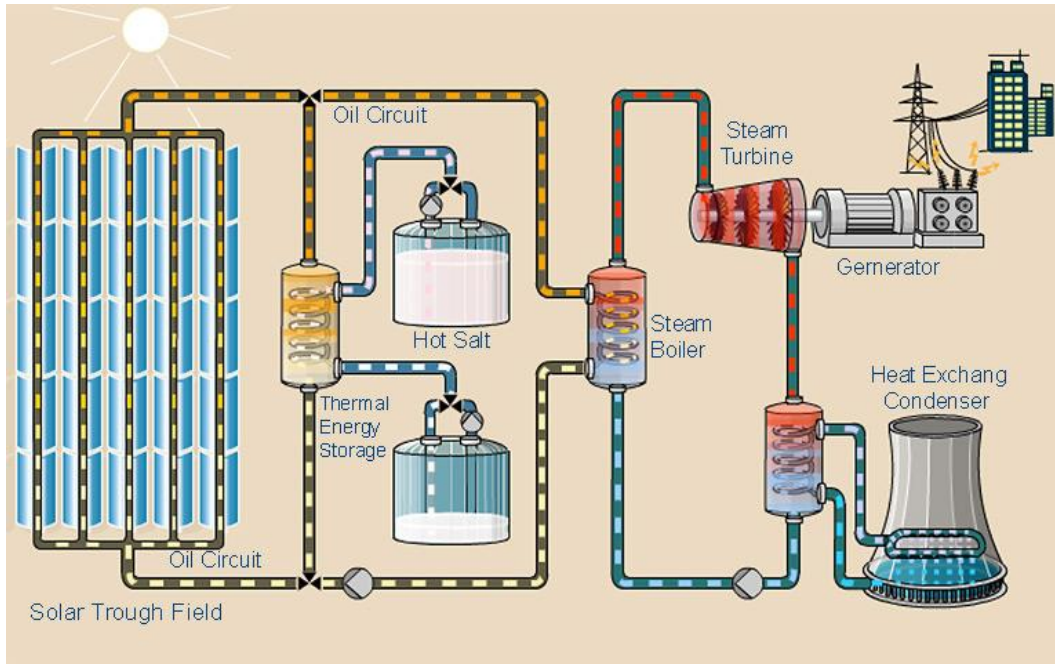


Fig. 1.1 Schematic of the PTC solar power plant [8]

The energy from the sunrays is captured in the PTC solar field for heating the heat transfer fluid (HTF). In the solar field, many numbers of PTCs are joined in series and parallel to achieve the required operating temperature and flow rate of the HTF respectively. High-temperature HTF (at $\sim 390^{\circ}\text{C}$) flows through the steam boiler, where the heat of HTF is transferred to water to generate high-pressure steam. The high-pressure steam is supplied to the steam turbine-generator to generate electrical power. The excess heat captured in the solar field during the daytime is stored by employing a thermal storage system. In a storage system, the thermal energy of the HTF is transferred to the molten salt in a heat exchanger. The heat of the molten salt is extracted during the night time to run the solar power plant. Fig. 1.2 shows the kramer junction solar

electric generating station (SEGS III-VII), California. It is a PTC solar power plant with a 150 MW of capacity.



Fig. 1.2 Kramer junction SEGS 3-7 plant, California. [9]

1.1 Parabolic trough collector

PTC is a line focused concentrated solar collector. The components of the PTC are shown in Fig. 1.3 [10]. The PTC comprises a cylindrical parabolic mirror, which focuses the incident solar rays on a heat collection element (HCE) i.e. Receiver. The axis of the receiver is concentric with the focal line of the parabolic trough. The HCE absorbs the energy from the concentrated sun rays and convert it into heat that is transferred to the HTF circulating through the solar field.

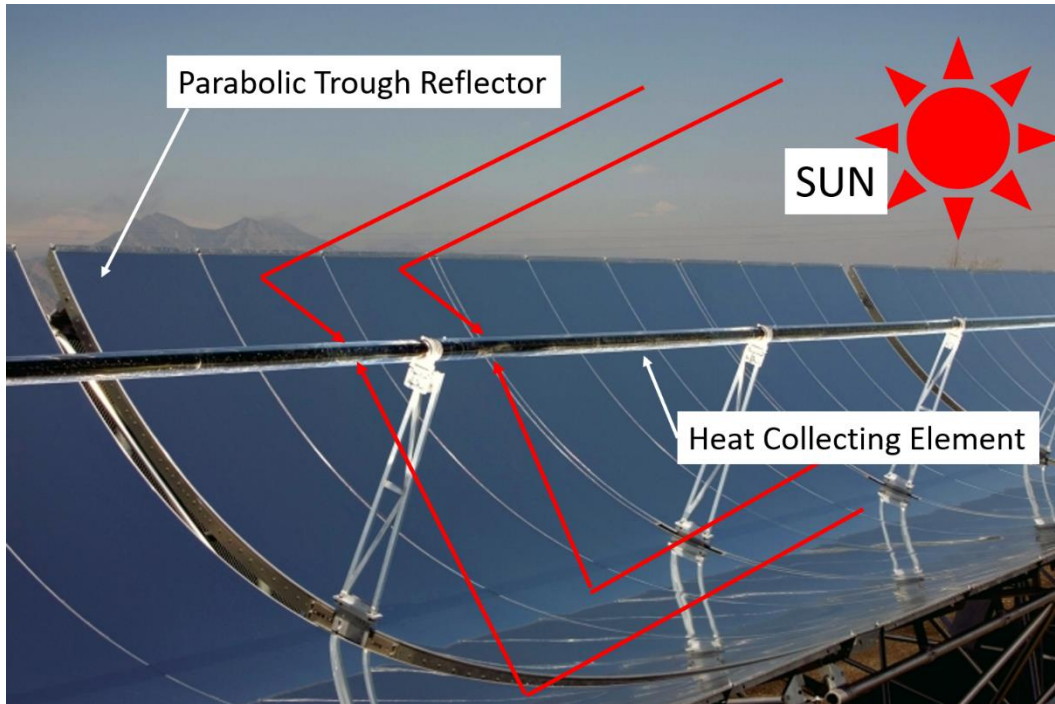


Fig. 1.3 Parabolic trough collector [11]

1.1.1 Geometry of PTC

The geometry of the PTC can be described by the following parameters i.e. aperture width (w), focal length (f), rim angle (ψ) and length of the trough (L) as shown in Fig. 1.4. The curvature of the parabolic concentrator (reflector) follows the Eqn. (1.1),

$$Y = F - \frac{X^2}{4F} \quad (1.1)$$

where “F” is the focal length of the parabola.

Aperture width is defined as the distance between two rims of the parabola. The rim angle is the angle between the optical axis and the line joining the parabola rim with the focal point. The rim angle can be calculated from the aperture width and focal length as given by Eqn. (1.2).

$$\psi = \tan^{-1} \left(\frac{w}{2 \left(F - \frac{w^2}{16F} \right)} \right) \quad (1.2)$$

Out of these three parameters (aperture width, focal length, and rim angle), any two parameters are required to determine the size of the parabola.

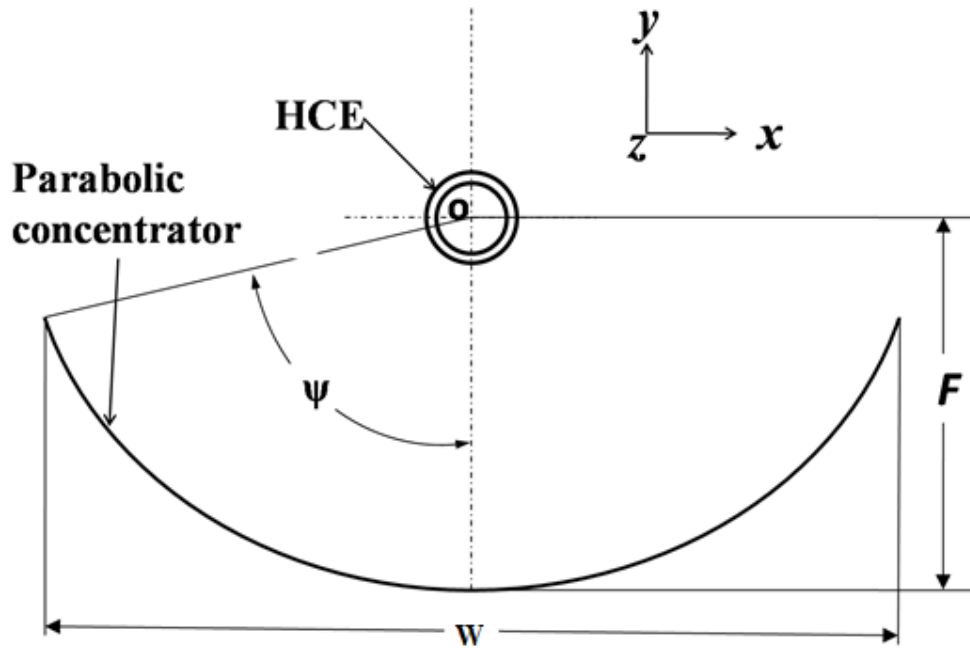


Fig. 1.4 Cross-sectional view of the PTC

1.1.2 Heat Collection Element

The HCE comprises a metal absorber tube enclosed within a concentric glass tube but separated by a vacuum space. The evacuated space in the HCE minimizes the convective heat losses. The glass tube allows the solar radiation, reflected from the parabolic mirror, to reach the absorber tube. The absorber tube absorbs the radiation to convert it into heat. The heat is transferred to the HTF circulating through the absorber tube. The outer surface of the absorber tube is coated with a material having high absorptivity and low emissivity to increase the absorption of radiation and to reduce the radiation heat loss from tube surface respectively. The optical characteristics of the selective coatings are presented in Table 1.1.

Table 1.1 Selective coatings [7]

HCE	Absorptance	Emittance
Luz Cermet	0.915	0.14
Solel UVAC	0.95 – 0.96	0.15

The cross-sectional view of the HCE is shown in Fig. 1.5, where d_{gi} is a glass tube inner diameter, d_{go} is a glass tube outer diameter, d_{ri} is the inner diameter of the absorber tube and d_{ro} is the outer diameter of the absorber tube.

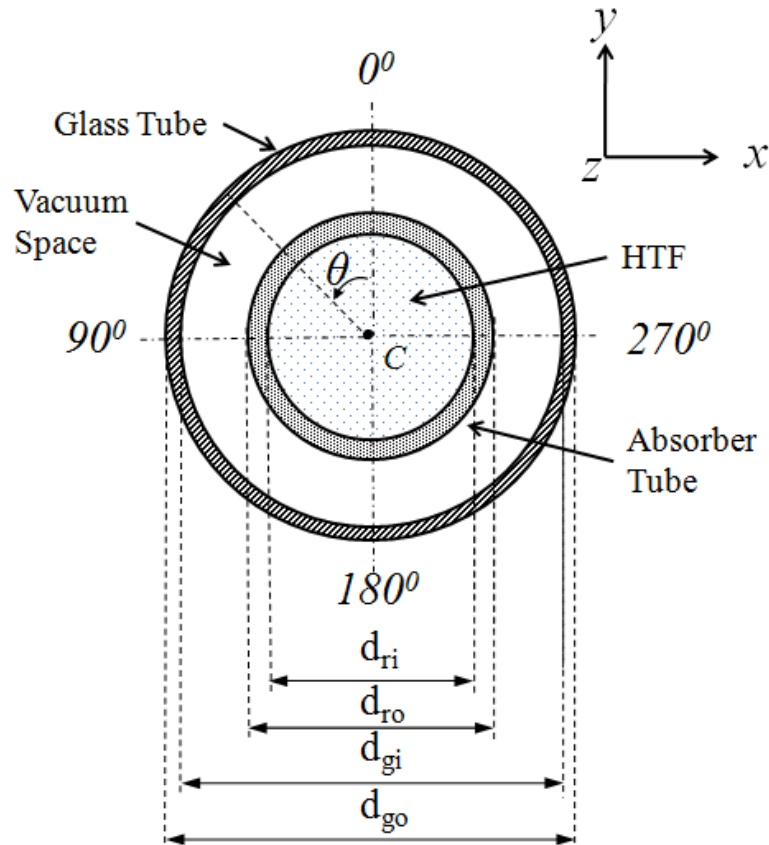


Fig. 1.5 Cross sectional view of the HCE

1.2 Concentration ratio

The concentration ratio (CR) is one of the important parameters in concentrating collectors. It is for achieving the operating temperatures in the power plant [12].

The CR represents the enhancement of solar energy received on the reflective surface of the concentrator. The higher CR leads to higher operating temperatures and results in a higher Rankin efficiency. The concentration ratio is classified as optical concentration ratio and geometrical concentration ratio.

The optical concentration ratio is defined as the ratio of average irradiance over

the absorber surface to the direct normal irradiation on the collector aperture. The geometrical concentration ratio is the ratio of the aperture area of concentrator and the surface area of the absorber. The geometrical concentration ratio is given by Eqn. (1.3)

$$CR = \frac{A_c}{A_a} = \frac{wL}{\pi dL} = \frac{w}{\pi d} \quad (1.3)$$

Where A_c is an aperture area of concentrator and A_a is the area of the outer surface absorber tube.

The optical concentration ratio is always lower than the geometrical concentration ratio on account of optical losses.

1.3 Sun Tracking System

Tracking of Sun is required to receive maximum direct solar radiation in case of concentrating collectors. As the PTC is a line-focused collector, the single axis sun tracking is required as shown in Fig. 1.6. The rotational axis is normally at the vertex line of the parabolic trough or in a parallel position to it. The parabolic troughs in the solar field can have any horizontal orientation. The north-south alignment with east-west tracking is preferred in power plants. East-west alignment with north-south tracking was used for experimental purposes only. Depending on the latitude where the power plant is installed, different orientations have different effects on the energy yield of the power plant. For latitudes below 40° and, generally, not too close to the equator (not below 15°), the following holds:

The East-west alignment has the following advantages and disadvantages:

- (i) The collector performance over the day is quite uneven. Due to large incidence angles, the collector performance is reduced considerably in the hours after sunrise and the hours before sunset. At noon, the full aperture always faces

the Sun. This means that the highest possible thermal peak power of the solar field at a given direct irradiance is always reached if it has east-west alignment (but not necessarily if it has a north-south alignment).

(ii) Energy yield differences between summer and winter are smaller than for north-south alignment.

(iii) Quite small tracking movements are required during the day.

(iv) The annual energy yield is lower than for north-south alignment.

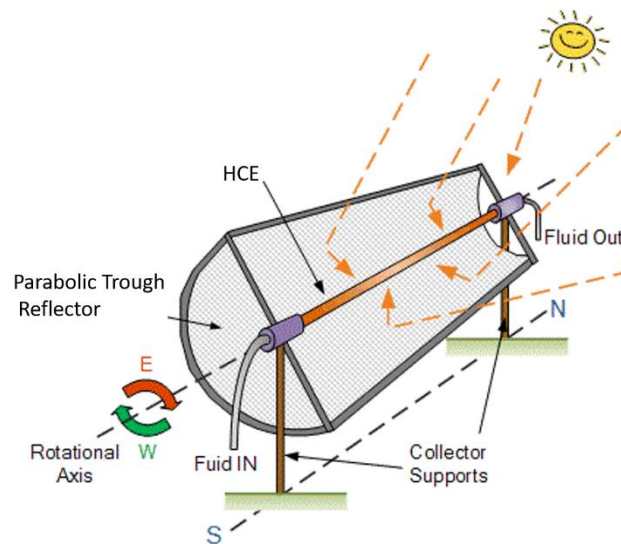


Fig. 1.6 Single axis tracking of PTC [13]

The North-south alignment has the following advantages and disadvantages:

(i) The collector performance over the day is quite even.

(ii) Due to incidence angle differences between summer and winter, the seasonal energy yield differences are larger than for east-west alignment.

(iii) The annual energy yield is higher than for east-west alignment.

The moment of the PTC is controlled by a drive unit, which moves the collector assembly in the sun direction. The drive units must be sufficiently strong to be able to move collector assemblies and to maintain them in the right position also

under wind conditions. Mechanically, the drive unit can be realized as a motor-gearbox unit determining the direction of rotation.

1.4 Heat transfer fluid

The function of HTF in a PTC power plant is to absorb the thermal energy in the PTC and transport it to the power generation block and realizing it in the boiler to generate the steam. However, there are two different types of heat transporting methods to transport the heat from the PTC to the power generation block. In the first method, the HTF is used to transport the heat from the PTC to the power block where the heat from the HTF is extracted to generate the steam to run the turbine. This is called indirect steam generation system. In the second method, the steam is directly generated in the PTC absorber tube. This is called direct steam generation system. In the direct steam generation systems, the heat transfer medium is water/steam of the Rankin cycle itself. In the indirect steam generation systems, synthetic oils are used as HTF. The commercial PTC power plants are usually equipped with indirect steam generation systems.

The HTF in indirect steam generation plants has to meet certain requirements. It should have a high evaporation temperature and low freezing temperatures so that it will not evaporate at high temperatures and no freezing protection devices are required if the temperatures in the solar field are very low. The HTF should have high specific heat so that a high amount of heat can be stored and transported. It should also have high thermal conductivity for quick heat transfer processes. Low viscosity is important to reduce pumping energy. Low investment costs and sufficient availability are also important criteria. Finally, environmentally friendly materials are preferable as well as

materials with low inflammability. Properties of some of the synthetic oils used as HTF in the commercial power plants are presented in Table 1.2.

Table 1.2 Correlations for the HTF properties.

HTF	Properties	$a + bT(K) + cT^2(K) + dT^3(K) + eT^4(K)$					Temperature (K)
		a	b	c	d	e	
Syltherm 800	$\rho(\text{kg m}^{-3})$	1.1E3	-4.1E-1	-6.06E-4	0.0	0.0	283.15–673.15
	$cp(\text{Jkg}^{-1}\text{K}^{-1})$	1.1E3	1.7	0.0	0.0	0.0	373.15–673.15
	$\lambda(\text{Wm}^{-1}\text{K}^{-1})$	1.9E-1	-1.87E-4	-5.75E-10	0.0	0.0	283.15–673.15
	$\mu(\text{Pa s})$	8.48E-2	-5.54E-4	1.38E-6	-1.56E-9	6.67E-13	283.15–673.15
Nitrate Salt	$\rho(\text{kg m}^{-3})$	2.26E3	-0.636	0.0	0.0	0.0	573.15–873.15
	$cp(\text{Jkg}^{-1}\text{K}^{-1})$	1.39E3	0.172	0.0	0.0	0.0	573.15–873.15
	$\lambda(\text{Wm}^{-1}\text{K}^{-1})$	3.91E-1	1.90E-4	0.0	0.0	0.0	573.15–873.15
	$\mu(\text{Pa s})$	7.55E-2	-2.77E-4	3.48E-7	-1.47E-10	0.0	573.15–873.15
Hitec XL	$\rho(\text{kg m}^{-3})$	1.67E3	-7.67E-2	0.0	0.0	0.0	477.15–755.15
	$cp(\text{Jkg}^{-1}\text{K}^{-1})$	2.81E3	0.0	0.0	0.0	0.0	294.15–866.15
	$\lambda(\text{Wm}^{-1}\text{K}^{-1})$	1.05	-6.58E-3	2.48E-5	-3.766E-8	1.92E-11	422.15–773.15
	$\mu(\text{Pa s})$	-7.58E-2	6.93E-4	-1.80E-6	1.95E-9	-7.87E-13	422.15–811.15
Therminol VP1	$\rho(\text{kg m}^{-3})$	1.34E3	-8.04E-1	-1.15E-3	2.36E-6	0.0	285.15–673.15
	$cp(\text{Jkg}^{-1}\text{K}^{-1})$	9.20E2	2.24	1.24E-3	-1.83E-5	4.41E-8	285.15–673.15
	$\lambda(\text{Wm}^{-1}\text{K}^{-1})$	1.45E-1	2.92E-5	-2.16E-7	3.30E-11	-7.2E-15	285.15–673.15
	$\mu(\text{Pa s})$	$10^{-6} \cdot e^{\left(\frac{544.149}{T(K)-273.15+114.43} - 2.59578\right)}$					285.15–673.15

1.5 Efficiency of PTC

PTCs are used to collecting the heat from the available solar radiation and transfer it to the HTF. Therefore, the collector efficiency of the PTC can be defined as the ratio of heat absorbed by the HTF to the amount of energy incident of the aperture area of the collector as given in the Eqn. (1.4)

$$\eta_c = \frac{\text{Heat gain by the HTF}}{\text{Energy incident on the aperture}} = \frac{Q_g}{I \cdot w \cdot L} \quad (1.4)$$

Where I is the direct normal irradiation, a is aperture width, L is the length of the collector and Q_g is heat gained by the HTF in the absorber tube and it can be calculated by using Eqn. (1.5)

$$Q_g = \dot{m} \cdot c_p (T_{in} - T_{out}) \quad (1.5)$$

The heat absorbed by the HTF in the PTC is always below the amount of energy incident of the aperture area of the collector because of energy losses at the various stages in the PTC. These losses include optical and thermal losses.

1.5.1 Optical losses

The total solar radiation incident on the aperture of the collector does not reach the absorber tube due to the optical losses in the PTC system. The optical losses occur due to the limited reflectivity of the mirror, absorptivity of the absorber tube and transmissivity of the glass tube. The optical losses also occur due to geometrical and optical errors present in the PTC system. During the construction and operation, the PTC system commonly encounters with these errors. The errors include receiver tube position error, profile error, local slope error, misalignment of the reflector and tracking error [14]. All these errors collectively reduce the intercept factor (γ). The optical performance of the PTC is commonly described by intercept factor and it is defined as the fraction of the number of the rays reflected by the collector that will be intercepted by the absorber [15].

1.5.1.1 Optical efficiency

The optical efficiency of the PTC can be defined as the ratio of amount radiation reaching the absorber tube to the radiation incident on the absorber. The optical efficiency of the PTC can be calculated using Eqn. (1.6) given by Guven and Bannerot [14]

$$Q_o = K(\theta) \rho_m(\tau_{gt}\alpha_{at})_n\gamma \quad (1.6)$$

1.5.2 Thermal losses

The HCE of the PTC is a complex heat exchanger, which converts the radiation into thermal energy. Thermal losses occur from the HCE to the atmosphere in the three modes of heat transfer; conduction, convection, and radiation. The thermal losses depend on the absorber tube temperature and ambient temperature. These losses increase with the increase of the temperature difference between the absorber tube and atmosphere. The energy flow in the HCE including losses is shown in Fig. 1.7.

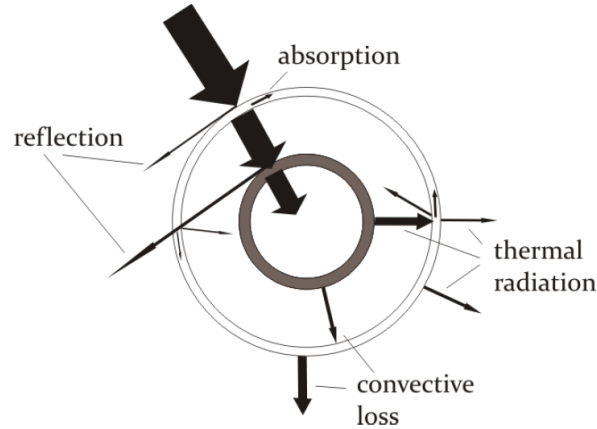


Fig. 1.7 Heat flow in the HCE

1.5.2.1 Thermal efficiency

The thermal efficiency of the collector is defined as the ratio of the heat absorbed by the HTF to the energy incident on the absorber tube and it is given in Eqn. (1.7)

$$\eta_t = \frac{\text{Heat gain by the HTF}}{\text{Energy incident on the absorber}} = \frac{Q_g}{q \cdot \pi \cdot d_{ro} \cdot L} \quad (1.7)$$

Where q is average heat flux over the absorber tube

1.6 Thesis organization.

The remaining chapters of this thesis have been organized in the following manner.

CHAPTER 2 deals with literature review related to common optical and geometrical errors encountered in PTC during the construction and operation of the PTC.

CHAPTER 3 explains the numerical methodology adopted in this study for optical analysis and thermal analysis. The validation of optical and thermal analysis results are also presented in this chapter.

CHAPTER 4 discusses the effect of absorber tube misalignment on the optical and thermal performance of the LS2 collector. Variation of optical efficiency, thermal efficiency and temperature gradients in the absorber tube for various operating conditions are presented.

CHAPTER 5 discusses the effect of absorber tube misalignment and slope error on the optical and thermal performance of the sener trough 2 collector. Variation of optical efficiency, thermal efficiency and temperature gradients in the absorber tube for various operating conditions are presented.

CHAPTER 6 discusses the improvement in the thermal performance of the PTC with finned absorber tube. Temperature gradients in the finned absorber tube and un-finned absorber tube are presented. The improvement in the Nusselt number, performance enhancement criteria are also presented.

CHAPTER 7 discuss the improvement in the concentration of the PTC with rhombus tube absorber. The improvement in the concentration ratio with rhombus tube absorber for different rim angles is presented. Variation of intercept factor with slope error is also presented.

CHAPTER 8 summarizes the major conclusions of the present study and offers the future scope of the work.

CHAPTER 2

LITERATURE SURVEY

The extraction of maximum thermal energy from available solar irradiation is one of the challenges in PTC. This can be achieved by improving the heat transfer in the absorber tube and/or by improving the concentration ratio. In the past few decades, many researchers [10, 15-20] have presented studies to improve the efficiency of the PTC; still, there is a scope for improvement in some aspects [21].

The thermal output of the PTC system depends on its optical efficiency and distribution of solar heat flux over the absorber tube. The optical efficiency and heat flux distribution of the PTC are significantly influenced by (i) the geometry of the collector, (ii) sun incident angle, (iii) optical properties of the materials used, (iv) optical and mechanical precision of the system elements [14, 22, 23]. To design a high efficient PTC, the optical, thermal, and mechanical properties of the PTC components are important [7, 24, 25]. In many cases, the optical performance of the PTC system is below the expectations even though the optical parameters such as reflectivity, specularity, transmissivity, and absorptivity are within the design values. It may be due to optical and geometrical errors present in the system. These errors occur during the installation/operation of the PTC system [14, 16, 22, 26]. The high precision installation methods are very expensive and complex [26].

2.1 Optical and geometrical errors

The important optical and geometrical errors, which extensively affects the intercept factor, are curvature precision of the reflective (concentrating)

mirror, tracking error, absorber tube misalignment and specularity of the mirror [15, 22-24, 26-30]. In some studies [15, 16], the errors were treated independently; random processes and their occurrences were approximated by Gaussian probability distributions. The total error is given by Eqn. (2.1).

$$\sigma_{tot}^2 = \sigma_{sun}^2 + (2 \times \sigma_{slo})^2 + \sigma_{mir}^2 + \sigma_{dis}^2 + \sigma_{tra}^2 \quad (2.1)$$

Where σ_{tot} represents the total error distribution, σ_{sun} is the standard deviation of the sun's energy distribution, σ_{slo} is the slope error distribution, σ_{mir} is the specularity error distribution, σ_{dis} is the receiver misalignment convolution distribution and σ_{tra} is the tracking error distribution. [10].

Guyen and Bannerot [14] studied different types of errors encountered and their influence on the optical performance of the PTC system. Thomas and Guven [31] proposed an analytical method to determine the effect of the receiver position error on the circumferential distribution of heat flux on the outer surface of the absorber tube. A series of experimental and analytical studies have been carried out to study the effect of optical and geometrical errors on the optical performance of the PTC [22, 26, 32-38].

2.1.1 Slope error

The curvature precision of the mirror is mainly described by two parameters profile error and local slope error. The profile error is the deviation of parabolic curvature from the designed shape and the slope error is the local deviations in the reflective mirror from the designed curvature as shown in Fig. 2.1. The deviations in the parabolic curvature occur due to the thermal expansion of mirror supporting structure, wind loading and gravity [39]. The slope error significantly degrades the optical performance of the PTC system [22, 27, 40]. Out of all these errors, the effect of slope error on collector

performance has been studied in detail [22, 27, 40]. Mwesigye, Huan [22] reported a numerical study on the effect of slope error on the optical, thermal and thermodynamic performance of the PTC system.

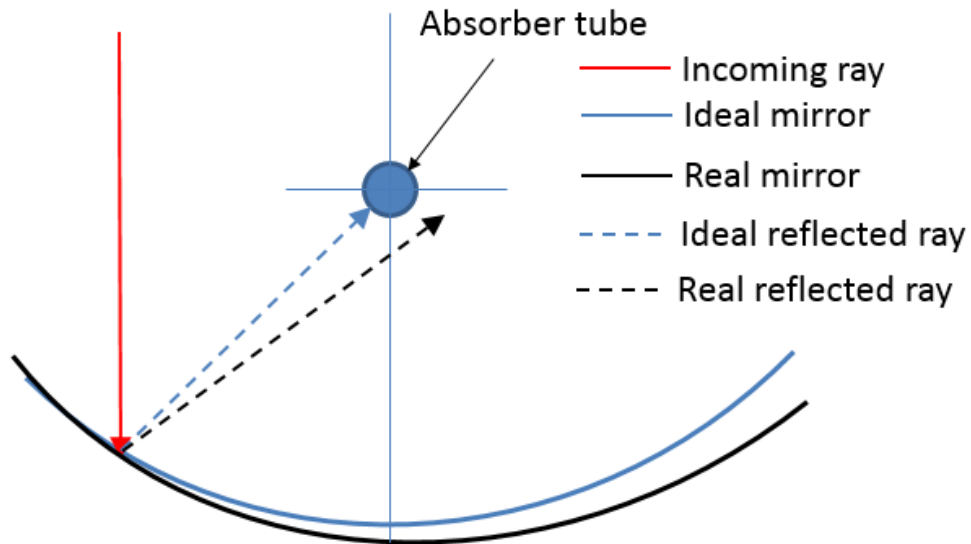


Fig. 2.1 Slope error

2.1.2 Tracking error

The Tracking error is defined as the deviation of the optical axis of the parabolic concentrator from the sun position [15] as shown in Fig. 2.2. The tracking error occurs due to improper tracking mechanisms of the PTC system. Zhao, Xu [26] reported that the tracking error significantly affects the heat flux distribution over the absorber.

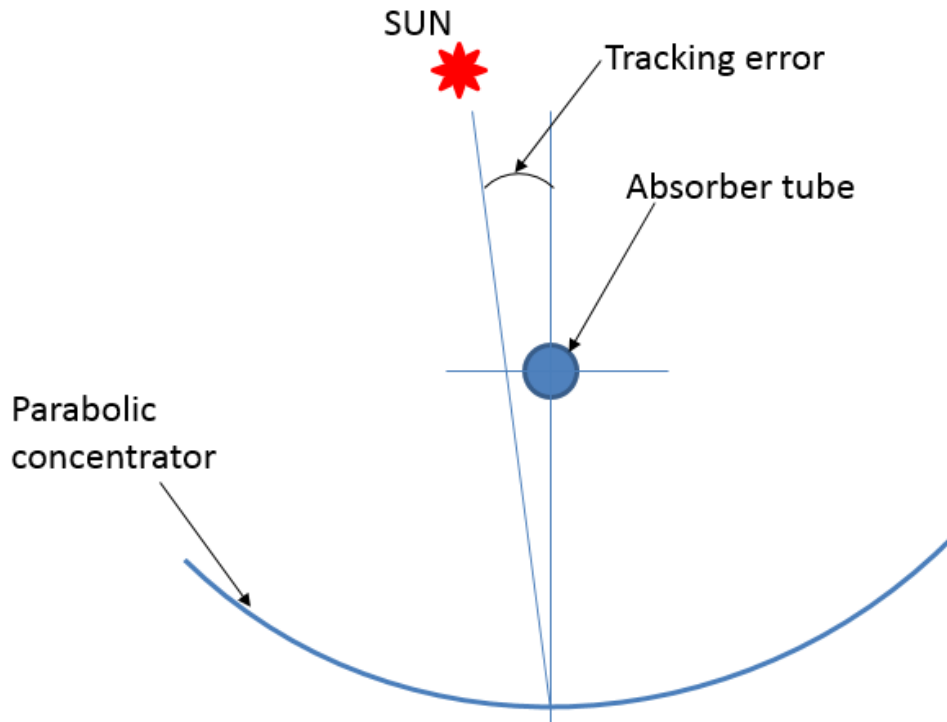


Fig. 2.2 Tracking error

2.1.3 Absorber tube misalignment

The absorber tube misalignment may be stated as the deviation of the axis of the absorber tube from the focal line of the cylindrical parabola. Due to the deviation of absorber tube from its ideal position the absorber tube may not receive all the radiation reflected from the reflecting surface as shown in Fig. 2.3. The effect of absorber tube misalignment on the optical performance of the PTC is well explored but its effect on the thermal performance of the PTC is unexplored.

The various probable reasons for absorber tube misalignment are : (i) improper mounting of the absorber tube-supporting frame [41], (ii) thermal stresses in the absorber tube [42, 43], (iii) variation in operating temperature from the designed value [24], (iv) distortion in the collector supporting frame due to wind load and gravity [23], (v) sagging of the absorber tube between the

supports due to its own weight and weight of the heat transfer fluid (HTF) [42, 44], (vi) sagging in the absorber tube-supporting frame due to dead weight of absorber tube and weight of HTF [24] and (vii) forces and torques from flexible tube connectors [45].

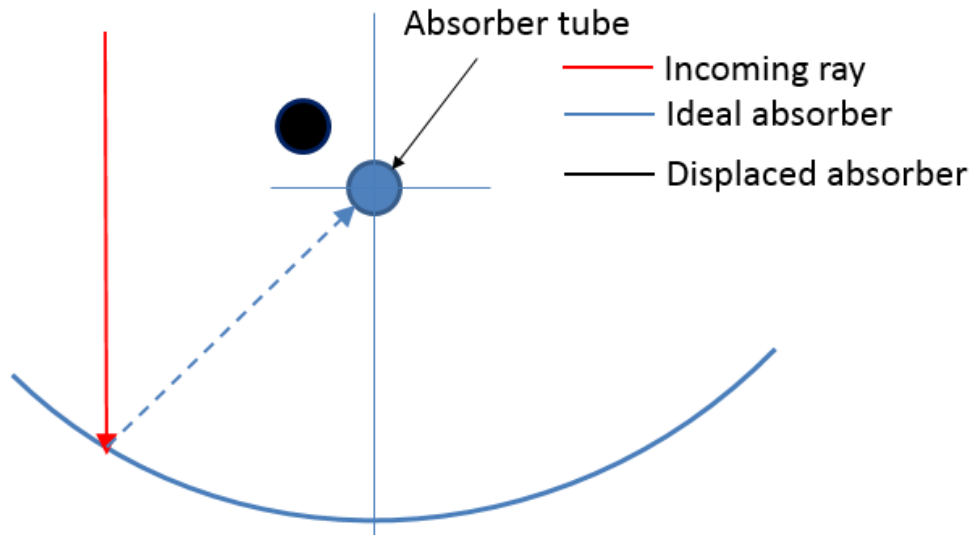


Fig. 2.3 Absorber tube misalignment

The absorber tube misalignment significantly degrades the optical efficiency of the PTC [23, 24, 46]. It also affects the heat flux distributions over the absorber tube [26], causing damage of the glass tube and malfunctioning of the tracking system [24, 47]. Some studies, experimental and analytical, on PTC performance with absorber tube misalignment without considering the surface slope error have also been reported in the literature. Treadwell [16], in 1976, had conducted an experimental study to determine collector efficiency by considering absorber tube misalignment. A PTC having an aperture width of 2 m, rim angle of 90° and absorber tube diameter of 25.4 mm was studied for the range of absorber tube misalignment from 0 to ± 30 mm. Treadwell and Grandjean [48] by using experimental data of the study of Treadwell [13]

developed a computer code to predict annual collector performance. In 2007, Lüpfer, Pottler [32] studied the influence of tracking error and absorber tube misalignment on the optical performance of the LS3 collector. Zhu [23] presented a FirstOPTIC analytical technique to analyze the effect of absorber tube misalignment on the intercept factor. Khanna, Kedare [27] presented an analytical technique to find the distribution of heat flux over the absorber tube with absorber tube misalignment. In 2016, Zhao, Xu [26] have studied the optical performance of the PTC with tracking error and absorber tube misalignment. In their study, the heat flux distribution over the absorber tube for different geometrical concentration ratios, tracking errors and receiver misalignments was presented.

From the above discussions, it is clear that the effect of absorber tube misalignment on the optical performance of the PTC is well studied [23, 26, 27, 32]. Detailed thermal analysis (heat flux distribution on absorber tube, temperature gradients in absorber tube and thermal efficiency) of the PTC with absorber tube misalignment by considering slope error has not been explored. The absorber tube misalignment substantially influences the heat flux distribution over the absorber tube and the local heat flux affects the heat transfer in the heat collection element (HCE) resulting variation of temperature gradients in the absorber tube. It is desirable to maintain the temperature gradient in the absorber tube within design limits to avoid the damage of the HCE due to thermal stress [49]. The detailed heat transfer analysis of the HCE is necessary to obtain the temperature gradients in the absorber tube and to know the overall performance of the PTC. Also for most of the accurate parabolic

trough collectors, a slope error of small magnitude may be expected hence slope error must be considered for performance evaluation of collectors.

2.2 Improving the heat transfer in the absorber tube

One of the most important challenges related to PTC is to increase the heat to be transferred from the absorber tube to the heat transfer fluid (HTF) [50, 51]. Improvement in heat transfer rate to HTF reduces the total number of receiver elements required in a solar field as the thermal output per an element increases [52]. Installation and operational costs are reduced with the lesser number of receiver elements thus improving the overall economics of the PTC system. Heat transfer rate in the absorber tube can be increased by providing more contact area to the fluid. Employing fins in the absorber tube is the best way to increase the fluid contact area and hence heat transfer rate. In active and passive methods, the passive method is widely accepted [53]. In passive method heat transfer rate is increased by increasing fluid contact area using fins. However, the pressure drop may increase with fins leading to more requirement of pumping power. Therefore, it is equally important to study both heat transfer and pressure drop in a receiver with fins.

Few studies have been reported in the past on improving heat transfer rate in the absorber tube by employing fins. Reddy, Kumar [50] were the first to study heat transfer characteristics of PTC receiver with longitudinal fins and porous fins. Longitudinal fins and porous fins were employed throughout the inner circumference of the tube. It was reported that inclusion of porous fins in receiver enhances the heat transfer by 17.5% on account of 2 kPa pressure drop. Cheng, He [54] have introduced the vortex generators inside the lower portion of the absorber tube to enhance the heat transfer and a maximum improvement

of 1.14 in the performance evaluation criteria are reported. Gong, Wang [55] had carried out a numerical study to enhance the heat transfer in a PTC receiver by using internal pin fin arrays and a 9% improvement in the average Nusselt number and 12% improvement in the overall heat transfer performance factor was reported. The studies [50, 55] suggest that pin fin can enhance the heat transfer but on the cost of significant pressure drop. Employing the longitudinal fins at the location of peak solar flux on the absorber tube may give better performance due to increased effective heat transfer area. A detailed heat transfer analysis needs to be conducted to evaluate the heat transfer enhancement and also the pressure drop.

2.3 Improving the concentration ratio

Improving the concentration ratio is one of the challenges in parabolic trough collector. From the Eqn. (1.3), it is clear that CR can be increased by increasing the size of the concentrator or decreasing the size of the absorber. The large size concentrators may have installation and operational issues such as structural stability under gravitational and wind loads. Also, high profile errors may be encountered during the operation of these PTCs. Over the decades the size of the concentrator has been increased and a maximum aperture size of 6.8 m is currently available commercially [12]. An added advantage of using smaller size absorber is a reduction in heat losses and improved thermal performance of PTC [12]. However, the minimum size of the absorber is limited by focal length, aperture width, Sun shape, slope error, specular error, receiver misalignment and tracking error of the PTC [12].

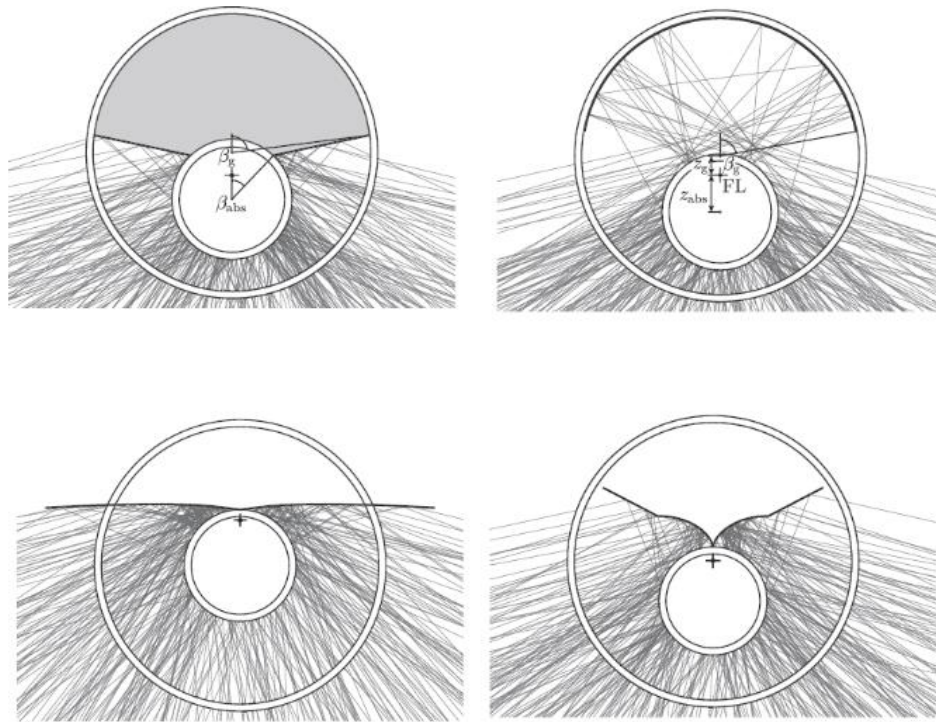


Fig. 2.4 Visualization of ray tracing with secondary mirrors [56-59]

Many solutions were proposed in the past to increase the concentration ratio of the PTC system by reducing the size of the absorber [56-59]. Use of the secondary mirrors of different shapes (flat and non-flat) behind the absorber tube is one of the techniques to decrease the size of absorber by sacrificing minimum reflected energy [12, 59-63]. Some of the proposed designs and shapes of secondary mirrors are shown in Fig. 2.4 [12, 56, 63-65]. The optical analysis performed on the PTC, with modified absorber, shows a 66% improvement in CR for LS1 collector with a 25% loss of total energy due to a shadow of the secondary mirror and loss of radiation through the gap between the absorber and secondary mirror [12]. Drawbacks of using a secondary mirror are increased cost and greater complexity of the receiver assembly. Secondary mirrors also produce a shadow on the absorber and/or concentrator thus constraining full capacity utilization of PTC. Modification in the shape of the absorber can be another option to increase CR without using secondary mirrors.

In the present study, a rhombus-shaped linear absorber is proposed for the PTC system to improve the geometrical concentration ratio, with almost same intercept factor as in circular tube absorber, by decreasing the size of the absorber, without using secondary mirrors. The intercept factor is defined as the ratio of solar energy reaching the absorber to the energy incident on the parabolic trough. A mathematical model has been developed to obtain the optimum size of rhombus tube absorber taking into account the acceptance angle, focal length and rim angle of the trough. A comparative study on CR of troughs using circular and rhombus tube absorber is also presented.

2.4 Optical analysis

As evident from the above literature, the receiver position error significantly affects the optical efficiency of the PTC and circumferential distribution of solar flux on the absorber tube, hence the thermal performance of the receiver.

The circumferential distribution of solar heat flux on the outer surface of the absorber tube is required as it is one of the boundary conditions in thermal analysis of the PTC receiver. Jeter [66] presented a semi-finite formulation technique for calculating the solar flux distribution on the circumference of the PTC receiver. Later on, Jeter [67] presented an analytical technique to calculate the circumferential solar flux distribution. Khanna and Sharma [40] presented an explicit analytical expression for the calculation of solar flux distribution on an undeflected absorber tube, by considering the sun shape and optical errors. Another technique to obtain the solar heat flux distribution is ray tracing. Monte Carlo ray trace (MCRT) method is widely used and it is a convenient technique to obtain the concentrated solar flux distribution [68]. Cheng et al. [69], He et al. [70] and Cheng et al. [71] have estimated the distributed solar flux by MCRT

method and the results of their studies were in good agreement with the analytical study of Jeter [66]. Ghomrassi et al. [72] used MCRT in SolTrace software to obtain the solar flux distribution for different absorber tube diameters. Mwesigye et al.[22] used the MCRT method in SolTrace software to estimate the solar flux distribution on the absorber tube for different values of local slope error and mirror specular error. Zhao et al. [26] also obtain the solar flux distribution for different receiver position errors, and tracking errors by using the MCRT method. Monte Carlo ray tracing (MCRT) method is the most extensively used technique in the optical analysis of the CSP devices in presence of geometrical/optical errors as it is more convenient and accurate [22, 26, 55, 68-79]. The same method has been adopted in the present study.

2.5 Thermal analysis

Many heat transfer models are available in the literature to analyze the heat transfer characteristics in the HCE of the PTC system. Some past models are based on the assumption of a uniform heat flux distribution [19, 80-86] over the absorber tube. These models do not predict temperature gradients in a glass tube and absorber tube. Recent models have considered the non-uniform heat flux distribution over the absorber tube [22, 37, 71, 87-89]. Non-uniform heat flux distribution can be obtained from an optical analysis to carry out heat transfer analysis. In the presence of absorber tube misalignment, the heat flux distribution over the absorber tube can be obtained by using analytical techniques [23, 27, 40]. Cheng, He [69] modeled the heat transfer in HCE by coupling MCRT with Finite volume method (FVM) and found very good agreement with the experimental results of Dudley, Kolb [90]. It was concluded that the simulated results [69] were in close agreement with the experimental

data [90], and the average relative error of collector efficiency was found within $\pm 2\%$ [69]. Subsequently, many researchers [22, 55, 69-72, 74-76, 91-94] have used the MCRT method coupled with FVM in their numerical studies for the thermal performance evaluation of the PTC system. A good agreement between the results of numerical studies [22, 69-71] and experimental studies [90] has been reported. As MCRT coupled with FVM technique is well studied and validated same has been adopted in the present study.

CHAPTER 3

NUMERICAL METHODOLOGY

In order to evaluate the overall performance of the PTC, the optical analysis of the PTC and the thermal analysis of the HCE are need to be conducted separately. The combined results present the overall performance of the PTC. The numerical optical analysis involves the ray tracing simulation of the PTC for a given geometrical and optical properties PTC components. The intercept factor, optical efficiency, and heat flux distribution over the absorber tube can be obtained from the optical simulation of the PTC.

The heat flux distributions obtained from the optical analysis are used in the heat transfer analysis of the HCE to simulate the heat transfer including conduction, convection, and radiation. The heat transfer analysis provides the temperature of the HTF, temperature gradients in a glass tube and absorber tube, heat loss from the HCE, heat gain by the HTF and pressure loss of the HTF in the HCE.

3.1 Optical analysis

The optical analysis of the PTC has been performed by using Monte Carlo Ray Tracing method in SolTrace software. The SolTrace software allows the user to simulate the PTC optically with optical and/or geometrical errors. The sun shape also can be specified in the software. A sample ray tracing simulation of the PTC using SolTrace software is shown in Fig. 3.1.

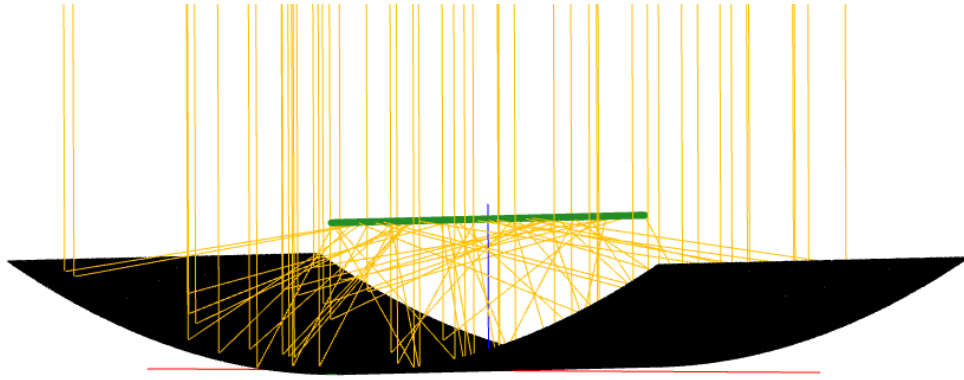


Fig. 3.1 Sample ray tracing simulation in SolTrace

3.2 Thermal analysis

The thermal analysis of the HCE has been carried out using the finite volume method (FVM) in Fluent[®] software. The value of distributed concentrated solar heat flux obtained by the MCRT method is introduced as a boundary condition in Fluent[®] software for successive thermal analysis. The results of numerical simulations have been used for the calculation of thermal efficiency and overall collector efficiency.

3.2.1 Governing equations

Reynolds-averaged Navier-Stokes (RANS) equations have been used to analyze the thermal performance of the receiver in FVM in the present study [95, 96]. Those are time-averaged equations of the turbulent flow for the conservation of mass, momentum, and energy given by Eqn. (3.1) - (3.3) in Mwesigye et al. [22] and Fluent[®] [95].

Continuity equation:

$$\frac{\partial}{\partial x_i} (\rho \bar{u}_i) = 0 \quad (3.1)$$

Momentum equation:

$$\frac{\partial}{\partial x_j} (\rho \bar{u}_i \bar{u}_j) = -\frac{\partial \bar{p}}{\partial x_i} + \frac{\partial}{\partial x_j} \left[\mu \left(\frac{\partial \bar{u}_i}{\partial x_j} + \frac{\partial \bar{u}_j}{\partial x_i} - \frac{2}{3} \delta_{ij} \frac{\partial \bar{u}_l}{\partial x_l} \right) - \rho \overline{u'_i u'_j} \right] \quad (3.2)$$

$$- \rho_0 g_i \beta (\bar{T} - \bar{T}_0)$$

Energy equation:

$$\frac{\partial}{\partial x_i} (\rho \bar{u}_i C_p \bar{T}) = \frac{\partial}{\partial x_j} \left[\frac{\partial \lambda \bar{T}}{\partial x_j} + \frac{\mu_t}{\rho r_t} \frac{\partial C_p \bar{T}}{\partial x_j} \right. \quad (3.3)$$

$$\left. + u_i \left(\mu \left(\frac{\partial \bar{u}_i}{\partial x_j} + \frac{\partial \bar{u}_j}{\partial x_i} - \frac{2}{3} \delta_{ij} \frac{\partial \bar{u}_l}{\partial x_l} \right) - \rho \overline{u'_i u'_j} \right) \right] + S_h$$

In the above equation, the term $-\overline{u'_i u'_j}$ (Reynolds stresses) calculated by eddy viscosity model which uses the Boussinesq hypothesis for correlating Reynolds stress to mean velocity gradients. The Reynolds stresses is calculated using Eqn. (3.4).

$$-\overline{u'_i u'_j} = \mu_t \left(\frac{\partial u_i}{\partial x_j} + \frac{\partial u_j}{\partial x_i} \right) - \frac{2}{3} \left(\rho k + \mu_t \frac{\partial u_k}{\partial x_k} \right) \delta_{ij} \quad (3.4)$$

Where k is turbulent kinetic energy obtain by Eqn. (3.5) and μ_t is eddy viscosity obtain by Eqn. (3.6). The Boussinesq hypothesis assumes turbulent viscosity (μ_t) is an isotropic scalar quantity. This model is relatively involve a low computational cost for estimating the value of turbulent viscosity (μ_t). The realizable $k - \varepsilon$ eddy viscosity model has been used to compute the eddy viscosity (μ_t). Two additional transport equations, turbulent kinetic energy (k) given in Eqn. (3.7) and turbulent dissipation rate (ε) given Eqn. (3.8) are solved to find the k and ε , these values are substituted in Eqn. (3.6) to find μ_t [97].

$$k = \frac{1}{2} \overline{u'_i u'_i} \quad (3.5)$$

$$\mu_t = \rho C_\mu \frac{k^2}{\varepsilon} \quad (3.6)$$

Turbulent kinetic energy (k) equation:

$$\frac{\partial}{\partial x_j}(\rho k u_j) = \frac{\partial}{\partial x_j} \left[\left(\mu + \frac{\mu_t}{\sigma_k} \right) \frac{\partial k}{\partial x_j} \right] + G_k - \rho \varepsilon \quad (3.7)$$

Turbulent dissipation rate (ε) equation:

$$\frac{\partial}{\partial x_j}(\rho \varepsilon u_j) = \frac{\partial}{\partial x_j} \left[\left(\mu + \frac{\mu_t}{\sigma_\varepsilon} \right) \frac{\partial \varepsilon}{\partial x_j} \right] + \rho C_1 S_\varepsilon - \rho C_2 \frac{\varepsilon^2}{k + \sqrt{\nu \varepsilon}} \quad (3.8)$$

Where

$$C_1 = \max \left[0.43, \frac{\eta}{\eta + 5} \right], \quad \eta = S \frac{k}{\varepsilon}, \quad S = \sqrt{2 S_{ij} S_{ij}}$$

G_k is generation of turbulence kinetic energy due to the mean velocity gradients given in Eqn. (3.9)

$$G_k = -\rho \overline{u'_i u'_j} \frac{\partial u}{\partial x} = \mu_t S^2 \quad (3.9)$$

The turbulent model constants for the realizable $k - \varepsilon$ model are: [95]

$$C_2 = 1.9, \quad \sigma_k = 1.0, \quad \sigma_\varepsilon = 1.2$$

$$C_\mu = \frac{1}{A_0 + A_s \frac{k \sqrt{\tilde{S} + \tilde{\Omega}_{ij} \tilde{\Omega}_{ij}}}{\varepsilon}}$$

Where,

$$A_0 = 4.04$$

$$A_s = \sqrt{6} \cos \left[\frac{1}{3} \cos^{-1} \left(\sqrt{6} \frac{S_{ij} S_{jk} S_{ki}}{\tilde{S}^3} \right) \right]$$

$$\tilde{S} = \sqrt{S_{ij} S_{ij}}, \quad \text{and } S_{ij} = \frac{1}{2} \left(\frac{\partial u_j}{\partial x_i} + \frac{\partial u_i}{\partial x_j} \right)$$

In addition to the conservation of mass, momentum and energy equations, the radiative heat transfer equation (RTE) is modeled using the discrete ordinates (DO) radiation model. The discrete ordinates radiation model solves the radiative transfer equation (RTE) for a finite number of discrete solid angles,

each associated with a vector direction \vec{s} fixed in the global Cartesian system. In the present study, all the surfaces of the receiver tube are assumed gray. Eqn. (3.10) shows the Radiative transfer equation (RTE) for gray radiation in the direction \vec{s} as a field equation [95].

$$\begin{aligned} \nabla \cdot (I(\vec{r}, \vec{s})\vec{s}) + (a + \sigma_s)I(\vec{r}, \vec{s}) \\ = an^2 \frac{\sigma T^4}{\pi} + \frac{\sigma_s}{4\pi} \int_0^{4\pi} I(\vec{r}, \vec{s}')\Phi(\vec{s}, \vec{s}')d\Omega' \end{aligned} \quad (3.10)$$

Where \vec{r} is position vector, \vec{s} is direction vector, \vec{s}' is scattering direction vector, 'a' is absorption coefficient, 'n' refractive index, σ_s is scattering coefficient, σ is Stefan-Boltzmann constant, I is radiation intensity, T is temperature, Φ is phase function and Ω' is the solid angle.

3.2.2 Simulation assumptions

The following assumptions are made in the FVM analysis: (i) steady state, (ii) isotropic and homogeneous material properties, (iii) turbulent flow, (iv) all surfaces are gray and diffusive, (v) negligible buoyancy generated turbulent kinetic energy, (vi) incompressible fluid, (vii) only radiative heat transfer between the outer surface of the absorber tube and inner surface of the glass tube is considered, and (viii) heat transfer fluid used was syltherm800. The physical properties of syltherm800 are considered as a polynomial function of temperature. The density (ρ), specific heat (c_p), thermal conductivity (λ) and viscosity (k) are given in Eqn. (3.11), (3.12), (3.13) and (3.14) respectively [71].

$$\begin{aligned} \rho = 1.105702 \times 10^3 - 4.15349 \times 10^{-1}T - 6.06165 \\ \times 10^{-4}T^2 \text{ (kg m}^{-1}\text{)} \end{aligned} \quad (3.11)$$

for $283.15 \leq T \leq 673.15$

$$C_p = 1.107798 \times 10^3 + 1.708T \text{ (J kg}^{-1} \text{K}^{-1}\text{)} \quad (3.12)$$

for $373.15 \leq T \leq 673.15$

$$\lambda = 1.90021 \times 10^{-1} - 1.875266 \times 10^{-4}T - 5.753496 \times 10^{-10}T^2 \quad (W \ m^{-1} \ K^{-1}) \quad (3.13)$$

for $283.15 \leq T \leq 673.15$

$$\mu = 8.486612 \times 10^{-1} - 5.541277 \times 10^{-4}T - 1.388285 \times 10^{-6}T^2 - 1.56600 \times 10^{-9}T^3 + 6.671331 \times 10^{-13}T^4 \quad (Pa \ s) \quad (3.14)$$

for $283.15 \leq T \leq 673.15$

3.2.3 Boundary conditions

The boundary conditions are defined as follows:

(i) *HTF inlet at absorber tube*: mass flow rate, Temperature (T_i)

(ii) *HTF outlet at absorber tube*: a fully developed flow governed by the following equation

$$\frac{\partial u}{\partial z} = \frac{\partial v}{\partial z} = \frac{\partial w}{\partial z} = \frac{\partial \varepsilon}{\partial z} = \frac{\partial k}{\partial z} = \frac{\partial T}{\partial x} = \frac{\partial p}{\partial x} = 0.$$

(iii) *End surfaces of the absorber tube, glass tube, and annular space (at $z=0$ and $z=4m$)*: adiabatic walls.

(iv) *the outer surface of the absorber tube*: nonuniform circumferential heat flux obtained from SolTrace was introduced by using user-defined functions [98], the emissivity of the coated material on the outer surface of the absorber tube was computed using Eqn. (3.15) which is given by Dudley, Kolb [90] and Forristall [19].

$$\varepsilon_{ro} = -0.065971 + 0.000327T_{ro} \quad (3.15)$$

(v) *The inner surface of the absorber tube*: no-slip boundary condition.

(vi) *The outer surface of the glass tube*: convection and radiation boundary condition. Radiative heat transfer from the outer surface of the glass tube to the

sky was calculated using Stefan-Boltzmann law. The sky was considered as a large enclosure and its effective temperature was calculated by Eqn. (3.16) [22, 72]

$$T_{sky} = 0.0552T_a^{1.5} \quad (3.16)$$

Convective heat loss from the outer surface of the glass tube was calculated by specifying the heat transfer coefficient and ambient temperature. Heat transfer coefficient was determined by using Eqn. (3.17) given by Mullick and Nanda [99]

$$h = V_w^{0.58} d_{go}^{-0.42} \quad (3.17)$$

The ambient temperature was taken as 298 K and wind velocity was taken as 2 m s⁻¹ for all the simulations in this study.

3.2.4 Numerical simulation.

The governing equations specified in the section 3.2.1 have been solved using FVM with boundary conditions specified in section 3.2.3. Realizable k-ε eddy viscosity model is used to model turbulent flow. Since this model cannot be applied near the solid wall, an enhanced wall treatment is employed near the wall regions. The geometry of the receiver has been generated in SolidWorks software. The generated geometry has been later imported in ICEM CFD [100], where structured mesh with hexahedral elements has been generated. A very fine mesh has been generated near the wall to capture the velocity and temperature gradients. The non-dimensional distance (y^+) near the wall has been maintained less than one for all simulations.

The generated mesh is then imported into Fluent to perform the FVM analysis. Pressure based coupled algorithm is used to couple the velocity and

the pressure fields. Since the momentum and pressure-based continuity equations are solved simultaneously in the coupled solver, the solution converges in less time with higher stability than the segregated solver. A second-order upwind scheme has been used for discretizing the momentum and energy equation, whereas pressure has been discretized using PRESTO scheme. Turbulent kinetic energy, turbulent dissipation rate, and discrete ordinates equations are discretized using the first-order upwind scheme. The convergence criteria for scaled residuals (mass, momentum, turbulent kinetic energy and turbulence dissipation rate) is taken less than 10^{-5} , while the discrete ordinates residuals and energy residuals are taken less than 10^{-8} for all the simulations.

3.3 Validation

3.3.1 Validation of the optical analysis

In order to valid the SolTrace software the distribution of local concentration ratio (LCR) on the circumference of absorber tube of the parabolic trough concentrator has been obtained from SolTrace software by considering the optical and geometrical properties of components of the PTC system from the study of Jeter [66] and He et al. [70]. The results thus obtained are validated with the results of Jeter [66] and He et al. [70] as shown in Fig. 3.2.

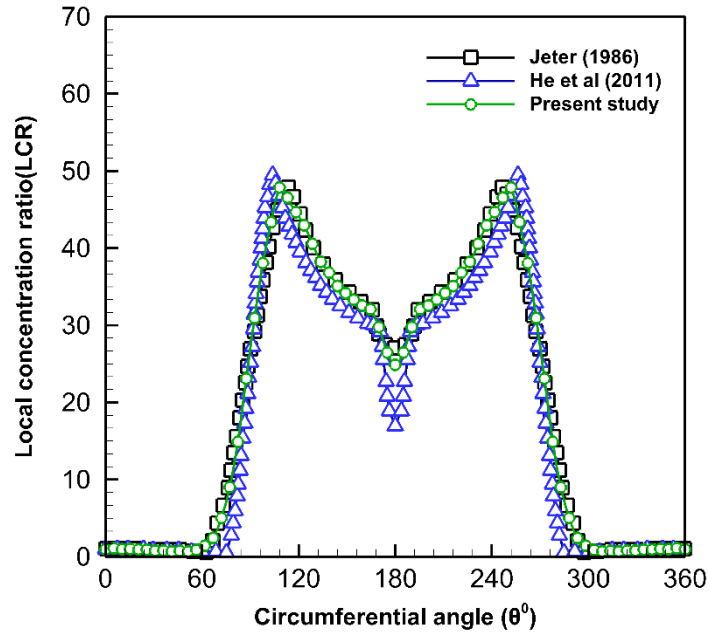


Fig. 3.2 Validation of the optical analysis

A direct normal irradiance (DNI) of 1000W/m^2 is assumed and the local concentration ratio (LCR) has been calculated by using the equation given as

$$LCR = q/DNI \quad (3.18)$$

Where ‘q’ is local heat flux in Wm^{-2} , DNI is direct normal irradiation of sun in Wm^{-2}

3.3.2 Validation of the thermal analysis

The numerical model has been validated by comparing the simulated results with the experimental data of Dudley et al. [90]. The simulations are performed for the optical, geometrical and operating parameters considered in the study of Dudley et al. [90]. The simulated are compared with results are found to be in close agreement with experimental results as shown in Table 3.1.

Table 3.1 Validation of the present study with experimental data

	DNI (Wm^{-2})	Flow rate (L min^{-1})	Wind speed (ms^{-1})	Air tempera ture ($^{\circ}\text{C}$)	T_{in} ($^{\circ}\text{C}$)	T_{out} ($^{\circ}\text{C}$) (Experiment al)	T_{out} ($^{\circ}\text{C}$) (Present study)	% error
1	933.7	47.7	2.6	21.2	102.2	124	128.08	3.29
2	937.9	55.5	1	28.8	297.8	316.9	318.22	0.41
3	920.9	56.8	2.6	29.5	379.5	398	398.64	0.16
4	880.6	55.6	2.9	27.5	299	317.2	318.02	0.82
5	909.5	54.7	3.3	26.2	250.7	269.4	270.8	0.51
6	968.2	47.8	3.7	22.4	151	173.3	175.6	1.32
7	982.3	49.1	2.5	24.3	197.5	219.5	221.75	1.02

CHAPTER 4

EFFECT OF ABSORBER TUBE MISALIGNMENT IN LS-2 COLLECTOR

This chapter presents the effect of absorber tube misalignment on the optical and thermal performance of the LS-2 collector. The LS-2 collector is a parabolic trough collector developed by Luz. It is used in SEGS III to SEGS VII power plants with SCHOTT PTR70 receiver. The dimensions of the LS-2 collector are presented in Table 4.1. The absorber tube misalignments in x -direction and y -direction are specified by ' Δx ' and ' Δy ' respectively and shown in Fig. 4.1. The range of Δx is considered from 0 to 30 mm and for Δy it is considered from -30 to 30 mm. As parabolic trough is symmetric about the y -axis, Δx in the negative direction is not considered.

Table 4.1 Dimensions of the LS-2 collector.

Parameter	Value
W	5m
L	4m
d_{gi}	0.109 m
d_{go}	0.115 m
d_{ri}	0.066 m
d_{ro}	0.070 m
F	1.84 m

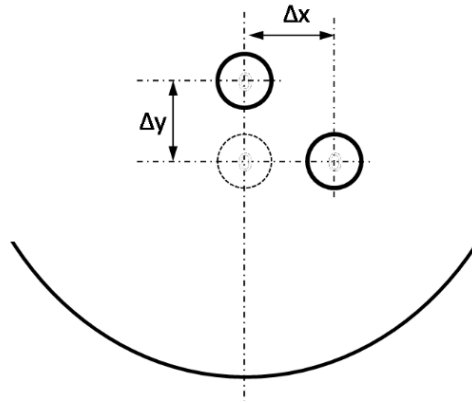


Fig. 4.1 Absorber tube misalignment

4.1 Optical analysis

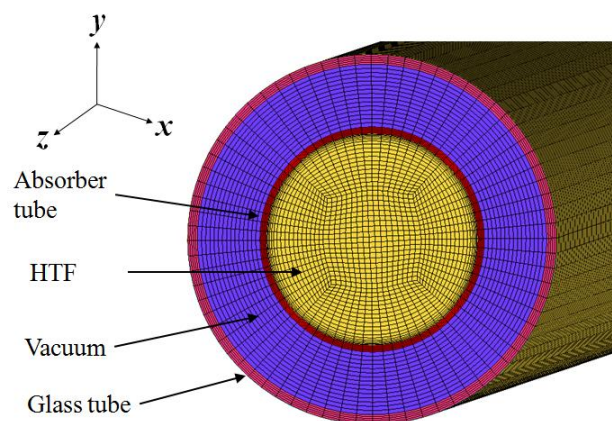
The optical analysis of the LS-2 collector has been carried out by using SolTrace software for different absorber tube positions (Δx and Δy). The details of the using SolTrace software is discussed in section 3.1. In SolTrace, the sun shape has been modeled as CSR0 measurement as suggested by Neumann, Witzke [101]. For simplifying the simulation, the profile error in parabolic curvature, mirror specularity error and local slope error of the parabolic concentrator are neglected. In SolTrace, the number of ray interactions and the maximum number of generated sunrays has been set to 10^6 and 10^8 respectively to obtain the accurate heat flux distribution. A direct normal irradiance (DNI) of 1000W/m^2 is assumed for all the cases presented in this chapter. The optical properties of the components of the LS-2 collector are listed in Table 4.2.

Table 4.2 Optical properties of the LS-2 collector

Parameter	Value
α_r	0.92
ρ_r	0.08
τ_g	0.935
ρ_g	0.045
ρ_m	0.93
τ_m	0

4.2 Thermal analysis

The thermal analysis of the PTC heat collection element has been carried out by using the Fluent[®] software. The details of the steps involved in the thermal analysis are discussed in section 3.2. The governing equations specified in the section 3.2.1 have been solved using FVM with boundary conditions specified in section 3.2.2. The inlet fluid velocity is 0.388 m/s, inlet temperature (T_i) ranges from 327 to 573 K. The structured mesh of the receiver assembly with hexahedral elements has been generated as shown in Fig. 4.2 to perform the numerical analysis. In order to capture the high velocity and temperature gradients near the wall, a very fine mesh has been generated at the wall. The non-dimensional distance (y^+) near the wall has been maintained less than one for all simulations. Simulations are carried out for different mesh sizes to find the mesh independent solution and 857,472 elements have been found optimal.



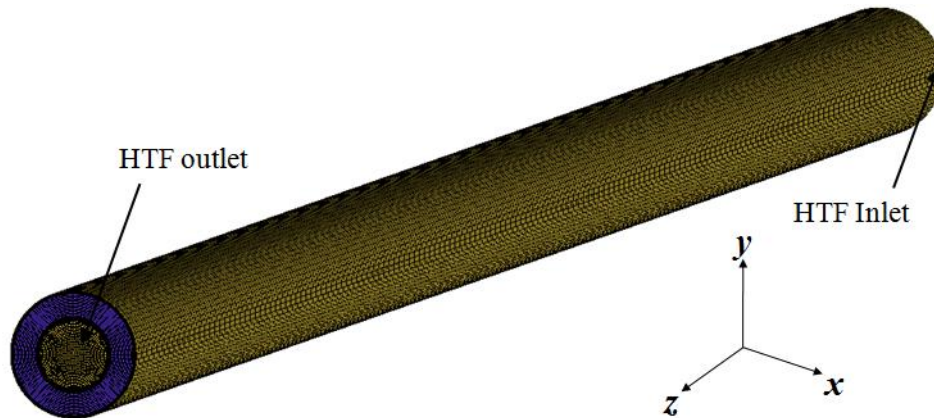


Fig. 4.2 Mesh of HCE

4.3 Results and discussion

4.3.1 Circumferential distribution of heat flux on the absorber tube

The circumferential distribution of heat flux over the absorber tube has been calculated by using SolTrace software. The procedure has been discussed in section 3.1. The ideal position of the receiver is taken as $\Delta x = 0$ and $\Delta y = 0$ i.e. the receiver is concentric with the focus of the parabolic trough. Fig. 4.3 shows the circumferential distribution of heat flux on the outer surface of the absorber tube for $\Delta x = 10$ mm and $\Delta y = -10$ mm. The circumferential heat flux distribution has been divided into two major regions 'A' and 'B' for discussing the pattern of heat flux distribution on the absorber tube as shown in Fig.6. Further, the regions 'A' and 'B' are divided into sub-regions namely shadow effect region represented by A_1 and B_1 , increasing solar flux area represented by A_2 and B_2 , reducing solar flux area represented by A_3 and B_3 and the direct radiation area represented by A_4 and B_4 . The peak flux in region A is termed as q_{PA} , the peak flux in region B is termed as q_{PB} and minimum heat flux in shadow effect area is termed as q_C . The regions 'A' and 'B' are separated at the location of q_C on the circumference of the absorber tube.

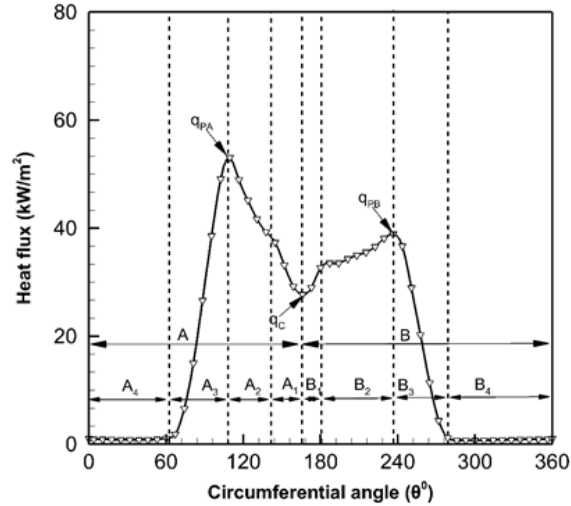


Fig. 4.3 Heat flux distribution over the circumference of absorber tube for absorber tube misalignments $\Delta y = -10$ mm and $\Delta x = 10$ mm

The distribution of heat flux on the circumference of the absorber tube with respect to the circumferential angle θ is shown in Fig. 4.4 for $\Delta x = 0$ and for a range of $\Delta y = -30$ to 30 mm. It can be observed that the distributed heat flux is symmetric about $\theta = 180^\circ$. The values of peak fluxes q_{PA} and q_{PB} are equal and increase when the receiver is displaced from $\Delta y = 0$, in positive y -direction i.e. away from the trough and decrease when the receiver is offset in the negative y -direction (towards the trough). As Δy changes from -30 to 30 mm, the angle spans of region A_4 and B_4 increase whereas the angle spans of A_3 and B_3 decrease. The angle span refers to the sector of the circular cross-section of the absorber tube. The angle span $(A_1 + B_1 + A_2 + B_2)$ between two peak fluxes decreases when the absorber tube is displaced in the y -direction from $\Delta y = -30$ to 20 mm. The angle span is zero between two peaks at $\Delta x = 20$ mm and for higher values of Δy only one peak is obtained. Thus it can be said that due to the displacement of the receiver, from the focus, away from the trough, concentrated rays fall on a smaller circumferential portion of the absorber tube and a bigger circumferential portion is exposed to the direct sun

radiation. Therefore, the peak flux increases as observed in Fig. 4.4 and vice versa occurs when the receiver is displaced, from the focus, towards the trough.

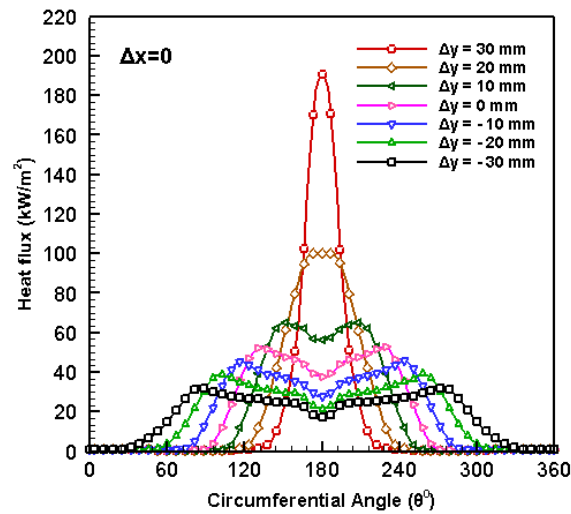


Fig. 4.4 Heat flux distribution over the circumference of absorber tube for absorber tube misalignments $\Delta y = -30$ to 30 mm and $\Delta x = 0$

Fig. 4.5 shows the distribution of heat flux for $\Delta x = 10$ and for a range of $\Delta y = -30$ to 30 mm. It can be seen that the distribution of heat flux is not symmetric. The region 'A' contracts and region 'B' expands with peaks q_{PA} and q_{PB} skewed towards left with respect to the ideal position of the receiver. The value of q_{PA} is higher than the value of q_{PB} for a whole range of Δy , however, both the heat fluxes are increase as Δy changes from -30 to 30 mm. The difference between the values of q_{PA} and q_{PB} is very small when Δy is equal to -30 and it drastically increases until Δy attains a value of 10 and for higher values of Δy only one peak is obtained. The shift of peak flux towards left with respect to the ideal position of the receiver occurs due to increase in the concentration of falling rays on the lower left a portion of the absorber tube because of the receiver displacement in positive x-direction ($\Delta x > 0$).

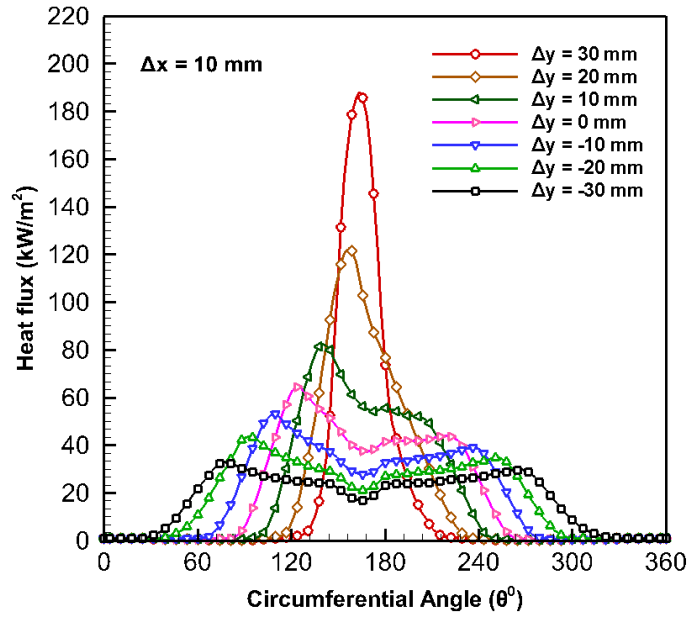


Fig. 4.5 Heat flux distribution over the circumference of absorber tube for receiver position errors $\Delta y = -30$ to 30 mm and $\Delta x = 10$ mm

Fig. 4.6 shows the distribution of heat flux for $\Delta x = 20$ mm and a range of $\Delta y = -30$ to 30 mm. It is observed that there is more shift in heat flux peaks in comparison to Fig. 4.5. The value of q_{PA} is lower than the value of q_{PB} for $\Delta y = -30$ mm, whereas the value of q_{PA} is higher than the value of q_{PB} for a range of $\Delta y = -20$ to 0 , and only one peak exists for $\Delta y > 0$.

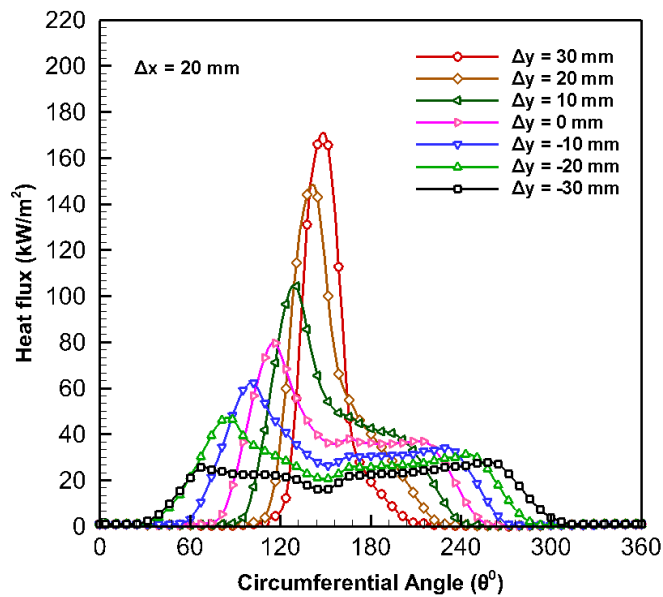


Fig. 4.6 Heat flux distribution over the circumference of absorber tube for receiver position errors $\Delta y = -30$ to 30 mm and $\Delta x = 20$ mm

Fig. 4.7 shows the distribution of heat flux for $\Delta x = 30$ mm and for a range of $\Delta y = -30$ to 30 mm. A similar trend of heat flux distribution is observed in Fig. 4.7. However, there is a slight decrease in the values of peak fluxes with an increase in the skewness of peaks more towards the left with respect to the ideal position. From the observations of Fig. 4.4 to Fig. 4.7 it is found that for a range of $\Delta y = -20$ to 10 mm, the value of q_{PA} increases and is skewed with an increase in receiver position error in the x-direction, for a range of $\Delta x = 0$ to 30 mm, because the same amount of rays reaches on the reduced area on the lower left portion of the absorber tube. However, the value of q_{PA} decreases at Δy equal to -30 and 30 mm when Δx increases in the range 0 to 30 mm.

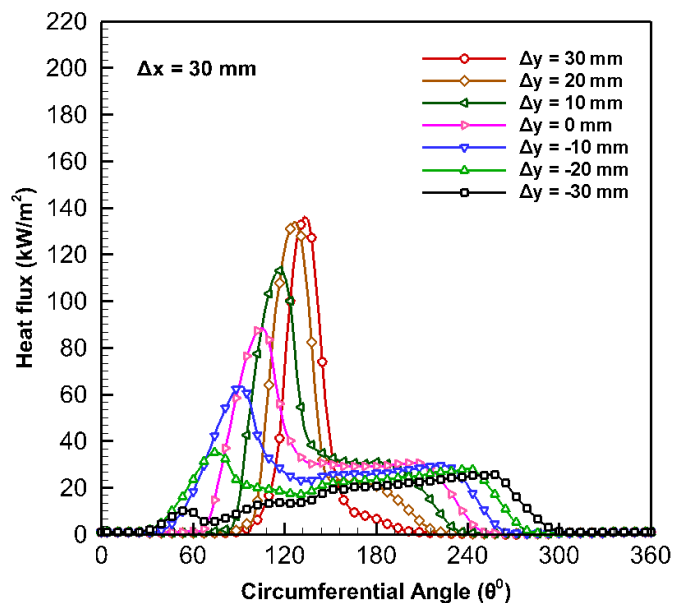


Fig. 4.7 Heat flux distribution over the circumference of absorber tube for receiver position errors $\Delta y = -30$ to 30 mm and $\Delta x = 30$ mm

4.3.2 Optical efficiency of PTC

The value of optical efficiency of the LS-2 collector has been calculated for a range of $\Delta x = 0$ to 30 mm and for a range of $\Delta y = -30$ to 30 mm and shown in Fig. 4.8. For all the receiver positions in the x-direction ($\Delta x = 0$ to 30 mm), the optical efficiency is almost the same when absorber tube is offset by the same amount in the positive or negative y-direction. It is observed from Fig. 4.4 to Fig. 4.7 that, at $\Delta x = -30$ mm, the magnitude of peak flux is low but the concentrated heat flux is distributed over a wider surface area of the absorber tube in comparison to the heat flux distribution at $\Delta y = 30$ mm where the case is reversed. Since the areas under the heat flux curves are equal (for $\Delta y = -30$ mm and 30 mm) same optical efficiency is obtained when the receiver is displaced equally either in the positive or negative y-direction. A similar observation is also found for the pair $\Delta y = -20$ mm, 20 mm and $\Delta y = -10$ mm, 10 mm as shown in Fig. 4.8. It is also observed that the values of the optical efficiency of the collector are similar for the same amount of displacement of the receiver in the lateral y-direction for different values of Δx , therefore $\pm \Delta y$ notation is used for discussion. It has been observed that at $\Delta y = 0$ there is no variation in the optical efficiency, when Δx changes from 0 to 20 mm, thereafter efficiency slightly decreases. In addition, no significant variation in the efficiency is observed for $\Delta y = \pm 10$ mm when Δx changes from 0 to 20 mm after that, the efficiency decreases till Δx changes to 30 mm. In comparison to $\Delta y = \pm 10$ mm, no significant drop in efficiency is observed at $\Delta y = \pm 20$ mm and for a range of Δx from 0 to 10 mm. A continuous fall in the efficiency is observed at $\Delta y = \pm 30$ mm as the Δx varies from 0 to 30 mm.

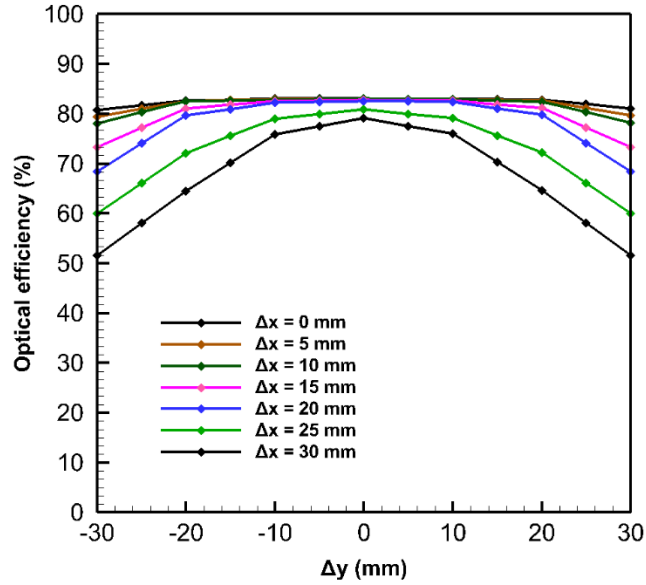


Fig. 4.8 Optical efficiency for $\Delta x = 0$ to 30 mm and $\Delta y = -30$ to 30 mm

4.3.3 Receiver thermal performance

The thermal analysis of the parabolic trough collector HCE has been carried out for the range of $\Delta x = 0$ to 30 mm and for a range of $\Delta y = -30$ to 30 mm. The detailed discussion about the thermal analysis is given in section 3.2. The Fig. 4.9 shows the velocity profile of HTF in yz -plane passing through the centerline of the receiver at z -locations equal to 0.5, 1, 1.5, 2, 2.5 and 3 m. It can be observed that a fully developed flow is obtained after 2 m from the inlet of the absorber tube, which satisfies the condition of fully developed flow.

Fig. 4.10 shows the circumferential distribution of the temperature on the outer surface of the absorber tube at $z = 1, 2, 3$ and 4 m for inlet fluid temperature equal to 373 K. As shown in Fig. 4.10, the variation in temperature distribution is negligible in the z -direction in comparison to the variation in temperature in θ -direction due to non-uniform circumferential heat flux distribution. Therefore, only the temperature distribution in θ -direction at $z = 4$ m is discussed for different receiver position errors (Δx and Δy).

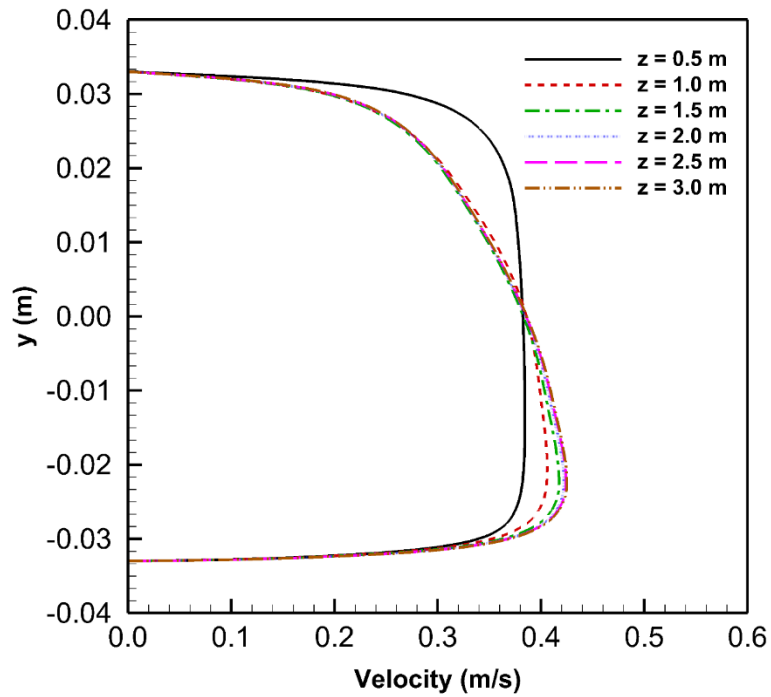


Fig. 4.9 Velocity profiles at different z locations for receiver position errors $\Delta x = \Delta y = 0$

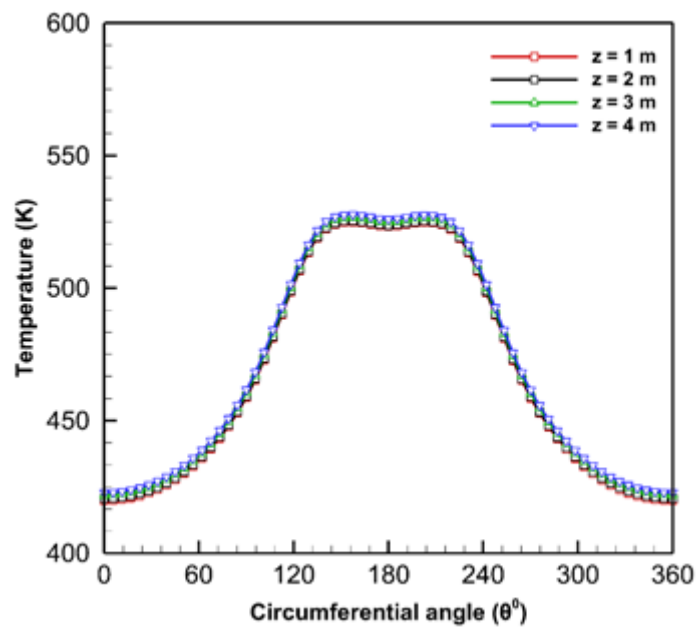


Fig. 4.10 Circumferential distribution of temperature on absorber tube at $z = 1, 2, 3$ and 4 m for $\Delta x = \Delta y = 0$

4.3.3.1 Streamlines and temperature contours

The spatial distribution of the temperature and streamlines at the outlet of the absorber tube ($z = 4$ m) are shown in Fig. 4.11 (a) - (t) for five receiver position errors in y-direction ($\Delta y = -30$ mm, -20 mm, 0 , 20 mm and 30 mm) and for four receiver position errors in x-direction ($\Delta x = 0$, 10 mm, 20 mm and 30 mm). It has been observed that in Fig. 4.11 (a) – (t), the value of the temperature in the lower portion of the absorber tube (facing the trough) is higher than that of in the upper portion (exposed to direct sun radiation) due to variation in concentrated heat flux. Because of this reason the HTF flowing over the lower surface of the absorber tube experiences differential heating. The increase in the temperature of the HTF decreases its density causing it to move upwards along the sidewall of the absorber tube due to buoyancy forces (see the pattern of streamlines in Fig. 4.11). At the upper region of the absorber tube, the streamlines along the sidewall of the absorber tube interact with each other in opposite direction, thus enhancing the mixing of fluid. Since the HTF at the bottom of the absorber tube moves upward along the sidewall of the absorber tube, the colder fluid from the central region rushes to fill it. This cyclic movement of the fluid creates two counter-rotating vortices in xy-plane. Therefore, any change in the distribution of heat flux over the absorber tube changes the orientation of streamlines and thus the shape and inclination of counter-rotating vortices. The ideal position of the receiver ($\Delta x = \Delta y = 0$) is shown in Fig. 4.11 (c). When $\Delta x = 0$, for a whole range of Δy the vortex streamlines and temperature distributions are symmetrical as seen in Fig. 4.11 (a) – (e) due to symmetric heat flux distribution. When Δx increases to 10 mm in Fig. 4.11 (f) – (j) for all values of Δy , the streamlines are asymmetric due to

the skewness of the heat flux distributions and higher value of q_{PA} compared to q_{PB} as observed in Fig. 4.5 (b). Because of this, the left vortex moves upward and the right vortex moves downward. The upward and downward movement of vortices is directly correlated to the difference between q_{PA} and q_{PB} and skewness of flux distributions. Similar trends are also observed in Fig. 4.11 (k) – (o) for $\Delta x = 20$ mm and Fig. 4.11 (p) – (t) for $\Delta x = 30$ mm due to the skewness of flux distribution and differences between the q_{PA} and q_{PB} as observed in Fig. 4.6 and Fig. 4.7 respectively.

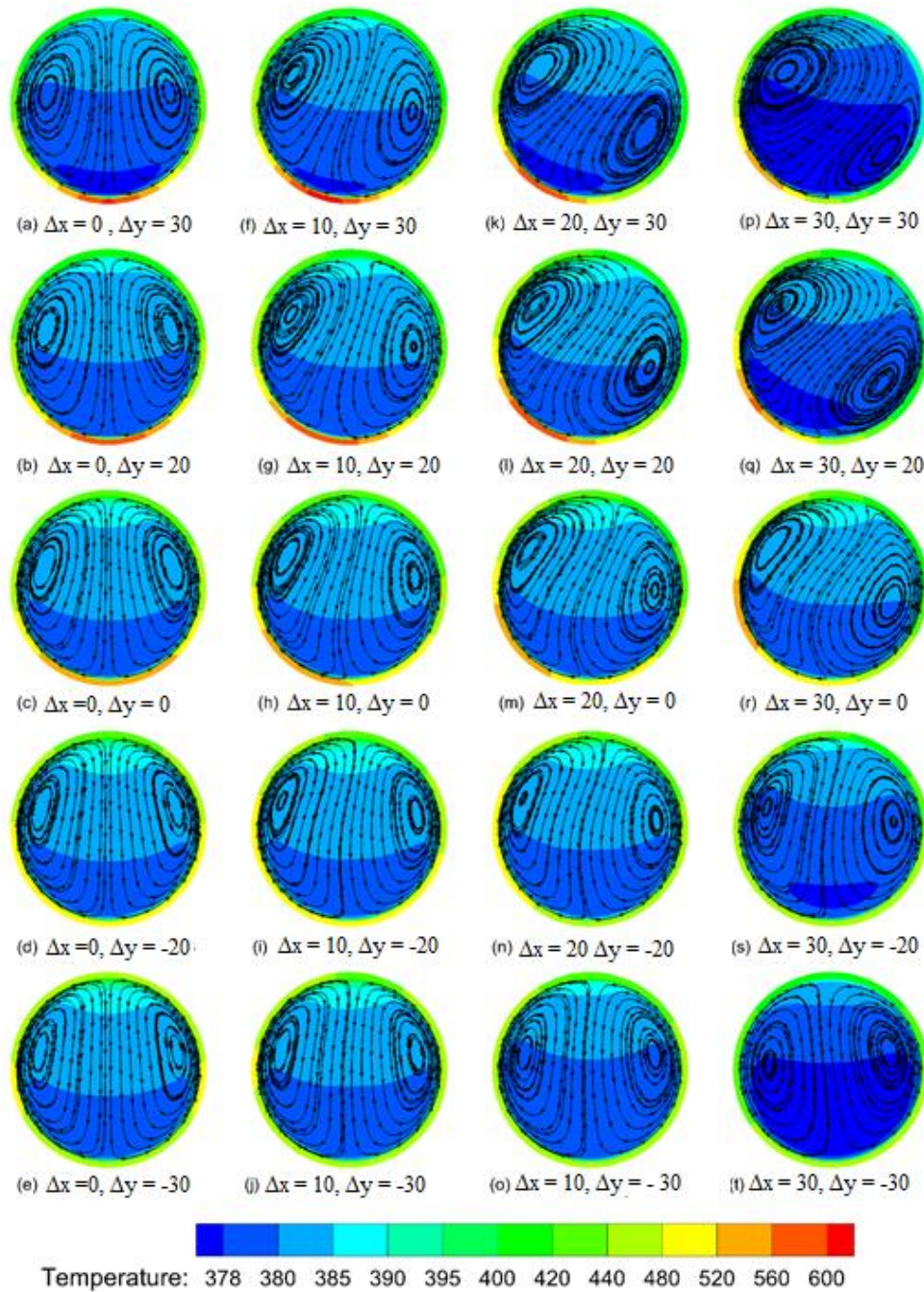


Fig. 4.11 Temperature contours and streamlines at the outlet of the absorber tube

4.3.3.2 Circumferential distribution of temperature on the absorber tube

The effect of the receiver position error on the circumferential distribution of temperature on the outer surface of the absorber tube at $z = 4$ m, for inlet fluid temperature of 373 K, is shown in Fig. 4.12 to Fig. 4.15. The temperature

distribution follows similar trends of heat flux distribution, but the curves of the former one are flatter than those of the latter one. Fig. 4.12 shows the temperature profile on the absorber tube for $\Delta x = 0$ and for a range of $\Delta y = -30$ mm to 30 mm. It can be seen that the maximum temperature (T_{\max}) and the difference between the maximum and minimum temperature on the absorber tube (ΔT) increase when the receiver is offset in the positive y-direction from the focus i.e. away from the trough. These decrease when the receiver is displaced in the negative y-direction from the focus of the parabolic trough. When the receiver is at an ideal position, the computed values of T_{\max} and ΔT at the outlet are found to be 527.7 K and 104.8 K respectively. When the value of Δy is equal to -30 mm, the T_{\max} and ΔT are found to be 482.7 K and 42 K respectively. At Δy equal to 30 mm, T_{\max} and ΔT are found to be 606.4 K and 199.7 K respectively. So the positive y-direction errors (displacement of the receiver away from the trough) should be avoided to protect the receiver from overheating and thermal stresses. Fig. 4.13, Fig. 4.14 and Fig. 4.15 shows the temperature profile on absorber tube for $\Delta x = 10$ mm, $\Delta x = 20$ mm and $\Delta x = 30$ mm respectively. As shown in Fig. 4.13 to Fig. 4.15 the temperature profile is asymmetric and follows the similar trends of the heat flux but the temperature in the right side is slightly lower than the left side. That is mainly because of convective currents caused by asymmetric heat flux distribution as shown in Fig. 4.11.

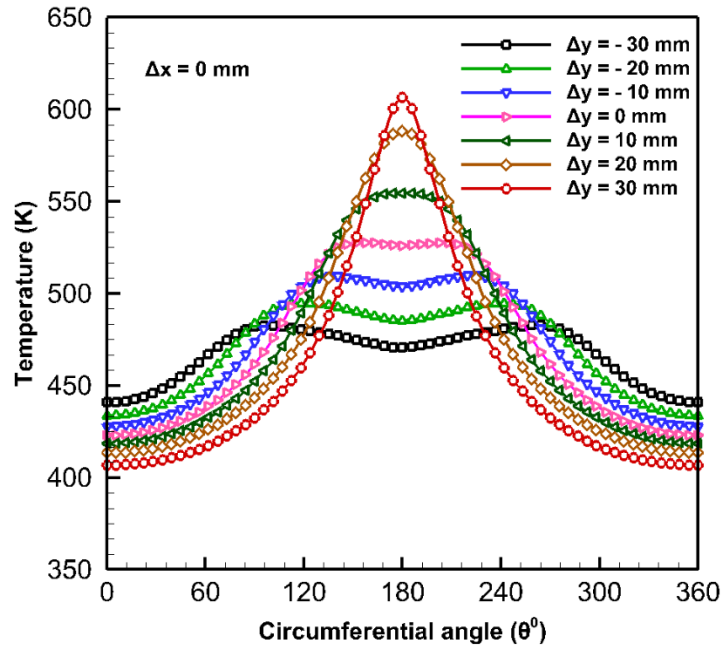


Fig. 4.12 Circumferential distribution of temperature on the outer surface of the absorber tube at $z = 4$ m for inlet temperature 373 K, $\Delta y = -30$ to 30 mm and $\Delta x = 0$ mm

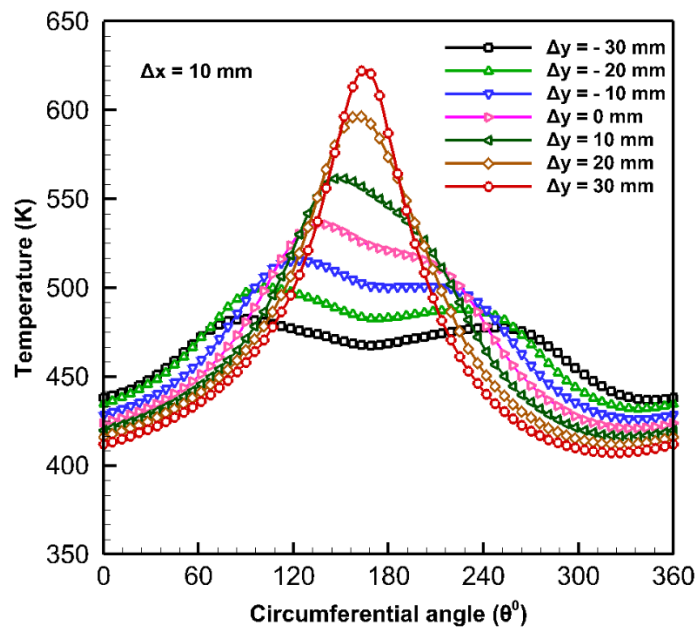


Fig. 4.13 Circumferential distribution of temperature on the outer surface of the absorber tube at $z = 4$ m for inlet temperature 373 K, $\Delta y = -30$ mm to 30 mm and $\Delta x = 10$ mm

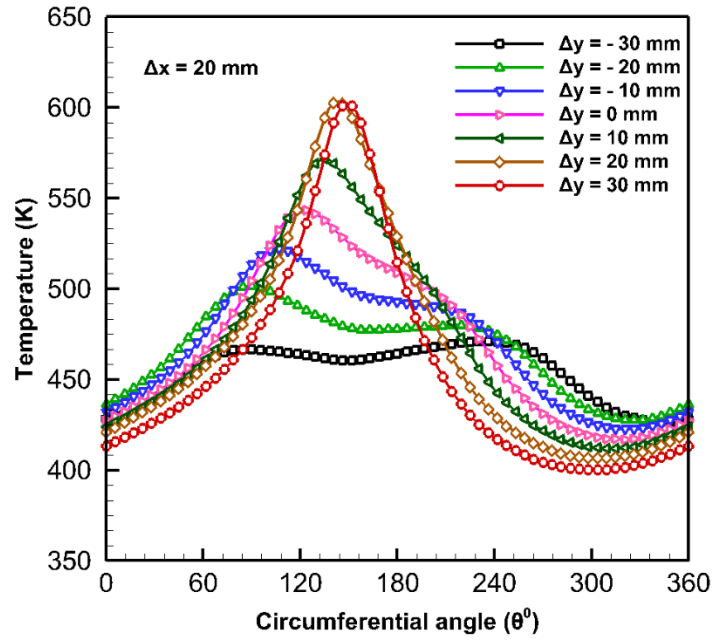


Fig. 4.14 Circumferential distribution of temperature on the outer surface of the absorber tube at $z = 4$ m for inlet temperature 373 K, $\Delta y = -30$ mm to 30 mm and $\Delta x = 20$ mm

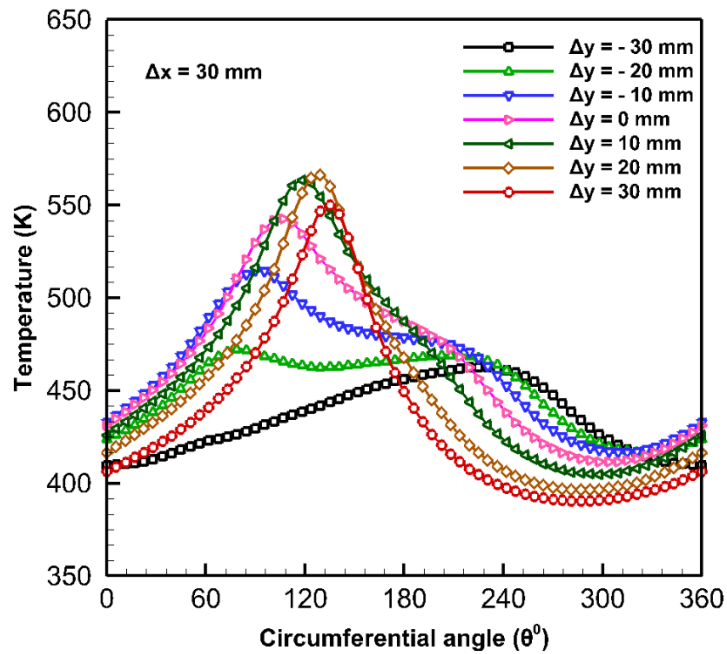


Fig. 4.15 Circumferential distribution of temperature on the outer surface of the absorber tube at $z = 4$ m for inlet temperature 373 K, $\Delta y = -30$ mm to 30 mm and $\Delta x = 30$ mm

4.3.3.3 Collector efficiency

The effect of the absorber tube misalignment on the collector efficiency is calculated using Eqn. (1.4) and shown in Fig. 4.16. The parameters considered for calculating the collector efficiency are: inlet fluid temperature = 373 K, range of receiver position error for $\Delta x = 0$ to 30 mm and for $\Delta y = -30$ mm to 30 mm. It has been observed that the efficiency may increase with increase or decrease in the receiver position error. For the ideal position of the receiver ($\Delta y = 0$ and $\Delta x = 0$), the computed value of collector efficiency is 78.1%. Whereas, when Δx increases to 30 mm keeping Δy equal to zero, a 3% fall in collector efficiency is observed. However, when Δy increases from 0 to 30 mm keeping Δx equal to zero, a 14% fall in the collector efficiency is observed due to the increase in non-uniformity of heat flux. In other condition when Δy changes from 0 to -20 and $\Delta x = 0$, the collector efficiency is increased by 1.3% because of increase in heat transfer due to the widespread of heat flux on the outer surface of the absorber tube as seen in Fig. 4.4. When $\Delta x = 0$, the collector efficiency for $\Delta y = 30$ mm is 14% lower than the collector efficiency when $\Delta y = -30$ mm, even though the optical efficiency is same for both the cases. This is mainly because of a pattern of distribution of heat flux on the absorber tube as seen in Fig. 4.4.

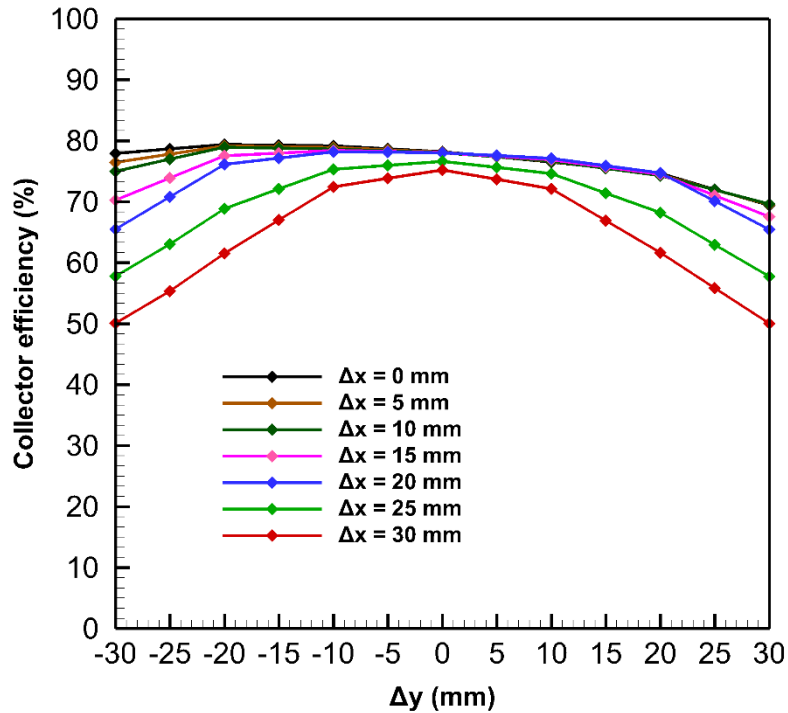


Fig. 4.16 Collector efficiency for $\Delta x = 0$ to 30 mm and $\Delta y = -30$ to 30 mm

Fig. 4.17 to Fig. 4.20 shows the variation in collector efficiency for different inlet fluid temperature ranging from $T_{in} = 323$ K to 523 K for receiver position error $\Delta x = 0, 10$ mm, 20 mm and 30 mm where the value of Δy ranges from -30 to 30 mm. The collector efficiency decreases with the increase of inlet fluid temperature for all the receiver position errors considered in this study. In all the cases approximately 7% fall in the efficiency is observed when inlet temperature increases from 323 to 573 K due to a decrease in the temperature difference between absorber tube wall temperature and HTF temperature. It is also observed that irrespective of Δx value, the difference between the collector efficiency for all Δy values remains the same along the temperature axis. Therefore, it can be concluded that the effect of inlet temperature and receiver position error on collector efficiency are independent.

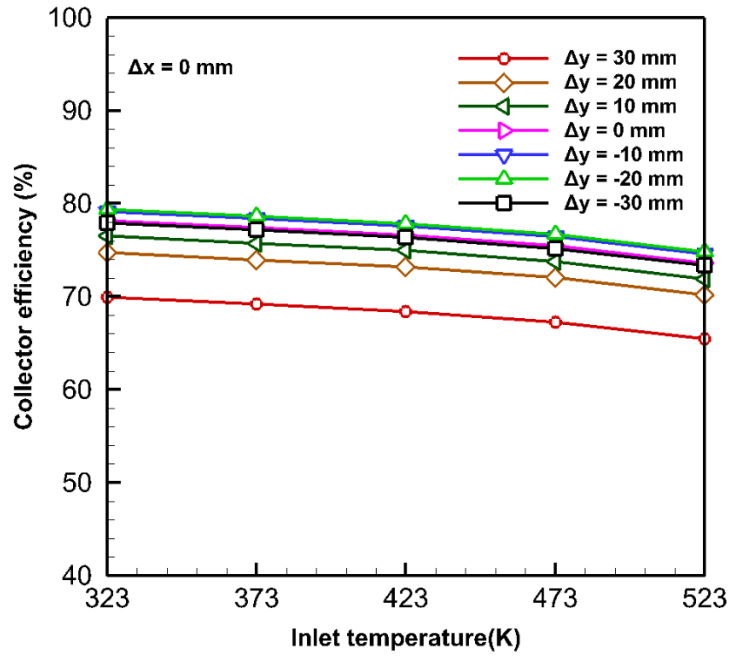


Fig. 4.17 Variation of collector efficiency with respect to inlet HTF temperature for $\Delta y = -30$ to 30 mm and $\Delta x = 0$

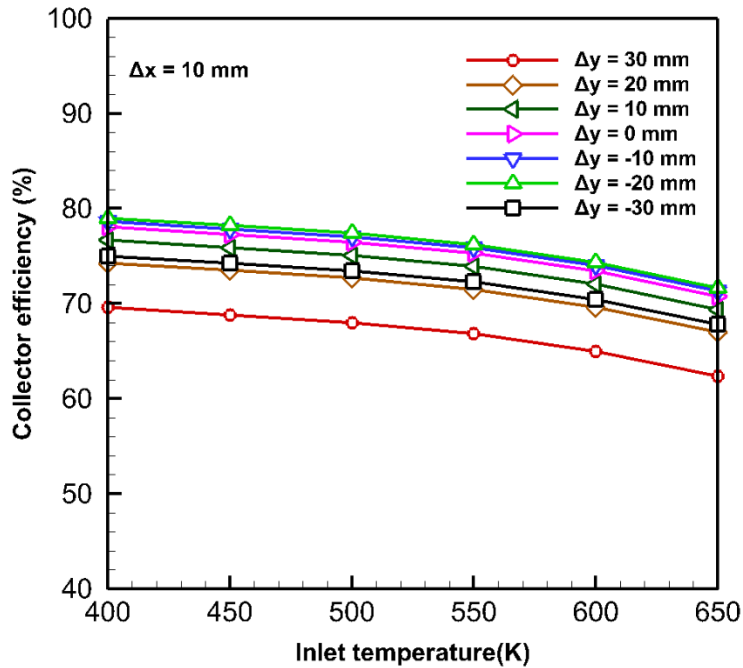


Fig. 4.18 Variation of collector efficiency with respect to inlet HTF temperature for $\Delta y = -30$ to 30 mm and $\Delta x = 10$ mm

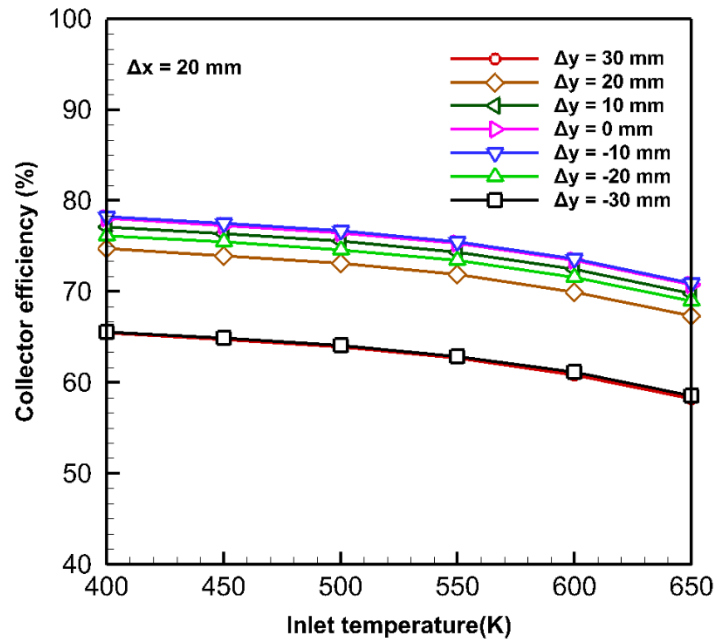


Fig. 4.19 Variation of collector efficiency with respect to inlet HTF temperature for $\Delta y = -30$ to 30 mm and $\Delta x = 20$ mm

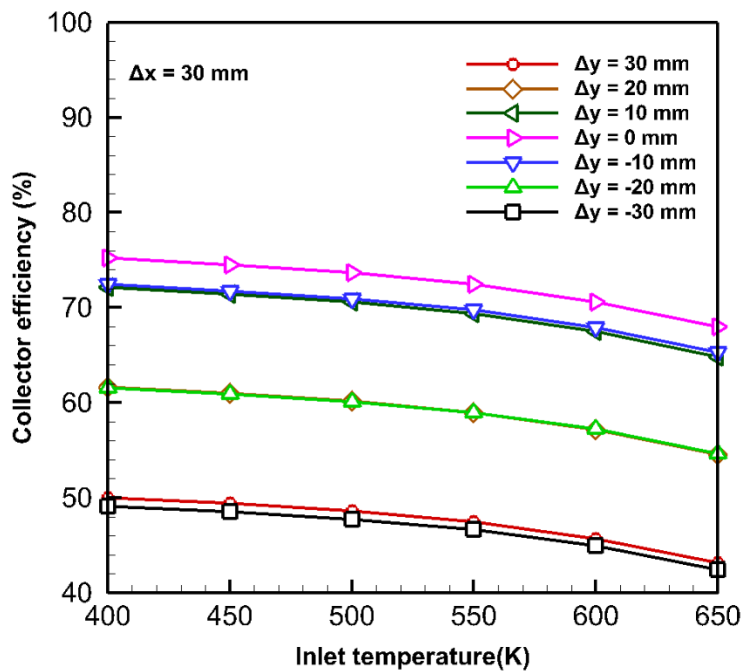


Fig. 4.20 Variation of collector efficiency with respect to inlet HTF temperature for $\Delta y = -30$ to 30 mm and $\Delta x = 30$ mm

CHAPTER 5

EFFECT OF ABSORBER TUBE MISALIGNMENT AND SLOPE ERROR IN SENER TROUGH -2

This chapter presents the effect of absorber tube misalignment and reflector surface slope error on the optical and thermal performance of the Sener trough 2 collector. The Sener trough 2 collector is a high aperture width parabolic trough collector with an aperture width of 6.868 m. The parameters of the Sener trough 2 collector are presented in Table 5.1. A numerical study has been conducted for the Sener trough 2 collector with two different diameters of the absorber tube, 70 mm and 80 mm. Simulations have been done for slope error and mass flow rate in the range of 0 to 3 mrad and 1 to 6 kg s⁻¹ respectively. The absorber tube misalignment up to 15 mm each in two directions i.e. along the optical axis and lateral direction has been considered. The intercept factor, circumferential temperature gradients in the absorber tube and overall collector efficiency of the PTC have been evaluated. Discussions on the results are presented in subsequent sections.

Table 5.1 Parameters of the Sener Trough 2

Parameter	Value	Parameter	Value
A	6.868 m	α_{at}	0.96
L	4 m	ρ_m	0.96
d_{gti}	115 mm	τ_{gt}	0.97
d_{gto}	125 mm	Ψ	81.3 ⁰
d_{ato}	70 mm & 80 mm	GC (Based on circumference of tube)	27.3 & 31.2
T	3 mm	F	2 m

5.1 Optical analysis

Optical performance of the Sener Trough 2 has been analyzed by using SolTrace software. The simulations have been performed by considering the parameters of the PTC specified in Table 5.1. The sun shape is modeled as a Gaussian distribution with a cone angle of 2.6 mrad and direct normal irradiation of 1000 w/m^2 is assumed for all the simulations as considered in the study of Mwesigye, Huan [22]. To obtain an accurate heat flux profile, the number of ray interactions and the maximum number of generated sunrays have been set to 10^6 and 10^8 respectively. Slope error of the mirror is considered from 0 to 3 mrad and the tracking error is assumed zero.

5.2 Thermal analysis

The thermal analysis of the Sener Trough 2 is carried out using the same method used in the thermal analysis of the LS-2 collector. The details of the steps involved in the thermal analysis are discussed in section 3.2. The governing equations specified in the section 3.2.1 have been solved using FVM with boundary conditions specified in section 3.2.2. As shown in Fig. 5.1 a structured mesh with hexahedral elements has been developed to achieve higher accuracy and faster convergence. The very fine mesh is generated near the inner surface of the absorber tube to capture the high velocity and temperature gradients of the HTF. The non-dimensional distance (y^+) near the wall has been maintained less than one for all simulations.

Mesh independent test has been carried out for the HCE with 70 mm and 80 mm diameter absorber tubes. The meshes with 1,310,720 and 1,351,680 hexahedral cells have been found optimal for 70 mm and 80 mm diameter respectively.

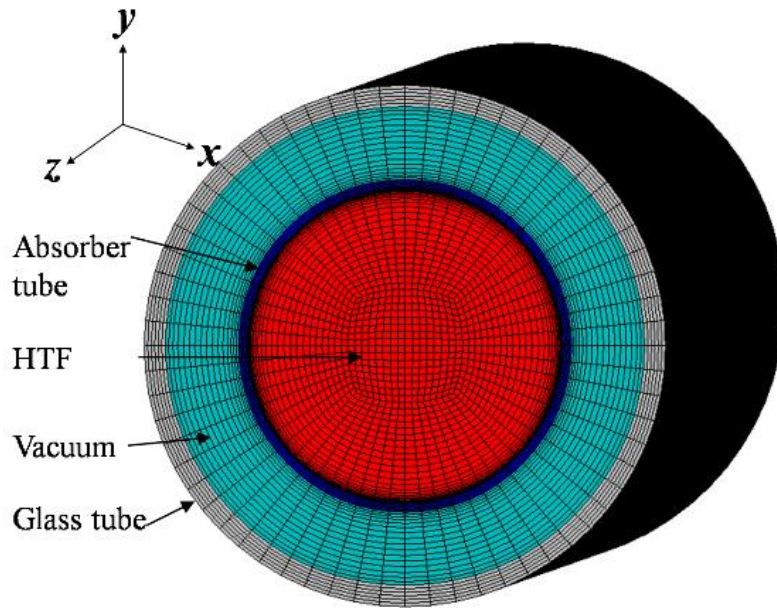


Fig. 5.1 Mesh of HCE

Pressure based coupled algorithm has been used to couple the velocity and pressure fields for faster convergence and high stability. The momentum and energy equations are discretized by using second-order upwind and pressure is discretized by using PRESTO scheme. First order upwind scheme has been used for discretizing the discrete ordinates, turbulent dissipation, and turbulent kinetic energy. The convergence criteria for scaled residuals have been taken less than 10^{-6} for all the simulations.

5.3 Results and discussion

5.3.1 Intercept factor

Fig. 5.2 shows the variation of intercept factor with absorber tube misalignment and slope error for 80 mm diameter absorber tube. Two values of slope error 0 mrad and 3 mrad have been taken. It can be observed from Fig. 5.2 that in absence of slope error the intercept factor is almost the same irrespective of the range of absorber tube misalignment considered in the present study. It can be

stated that the intercept factor is not influenced at all by absorber tube misalignment in absence of slope error. However, with slope error, there is a cumulative effect on the intercept factor. In the presence of slope error (3mrad), the curves showing variation in intercept factor are almost symmetrical about $\Delta y = 0$. It indicates that the drop in the value of intercept factor is almost same for same magnitude of absorber tube misalignment in the positive y-direction ($\Delta y > 0$) and in the negative y-direction ($\Delta y < 0$) i.e. along the optical axis. For the perfectly aligned receiver, the intercept factor is reduced by up to 1.6% when slope error is 3 mrad. At slope error of 3 mrad, the intercept factor decreases with an increase in the magnitude of absorber tube dislocation in both directions. The intercept factor decreases by up to 4.4 % with slope error when absorber tube dislocation is 15 mm in y-direction only. With slope error and absorber tube dislocation of 15 mm in the x-direction only, the intercept factor decreases by up to 3.1 %. However, a maximum decrease of up to 6.5 % in intercept factor is observed when the magnitude of absorber tube misalignment is 15 mm each in both directions (optical axis and lateral direction) in presence of slope error.

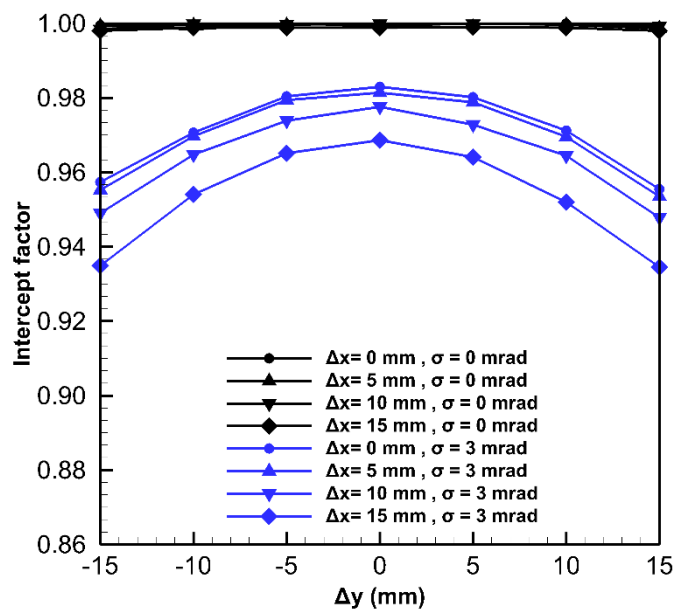


Fig. 5.2 Variation of intercept factor with absorber tube misalignment and slope error for $d_{\text{ato}} = 80$ mm

Similar trends for variation of intercept factor with absorber tube dislocation and slope error are observed for 70 mm diameter absorber tube as shown in Fig. 5.3. However, the drop in the value of the intercept factor is higher in the case of a 70 mm diameter absorber tube than 80 mm diameter absorber tube in the presence of slope error. The reason for this may be that some of the reflected rays escape the absorber due to its smaller size. For perfectly aligned absorber tube, the intercept factor is reduced by up to 3.4% when the slope error is 3 mrad. With slope error, the value of the intercept factor decreases by up to 11 % when the absorber is displaced by 15 mm each in both directions (x, y).

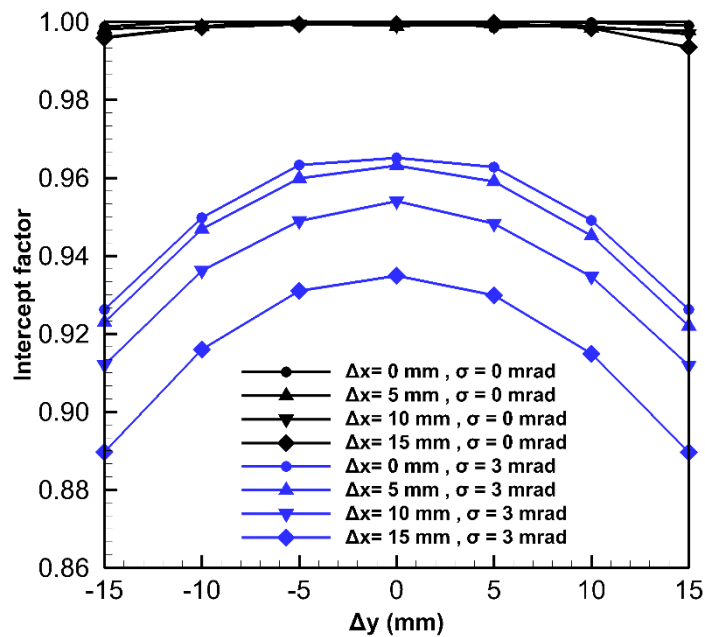


Fig. 5.3 Variation of intercept factor with absorber tube misalignment and slope error for $d_{\text{ato}} = 70$ mm

5.3.2 Heat flux distribution over the absorber tube

The distribution of heat flux over the absorber tube has been studied for two different diameters of the absorber tube. The effect of slope error and absorber

tube misalignment on heat flux distribution over the absorber tube has also been analyzed separately. Fig. 5.4 shows the circumferential heat flux distribution over the absorber tube for 70 mm and 80 mm diameters by considering slope error only. It can be seen that the absorber tube diameter and slope error affect the heat flux distribution. The peak heat flux and average heat flux decreases with an increase in slope error and diameter of the tube. In the absence of slope error, the values of peak flux and average heat flux are higher in case of 70 mm diameter tube than 80 mm diameter tube. The values of average heat flux are 31283 W/m² and 27278 W/m² for 70 mm and 80 mm absorber tube respectively with zero slope error. It may be due to higher geometric concentration ratio for 70 mm diameter absorber tube. For 70 mm absorber tube, the average heat flux is 30141 W/m² at slope error 3 mrad. Nearly constant peak heat flux is obtained with slope error on almost one-third portion of the circumference of the absorber.

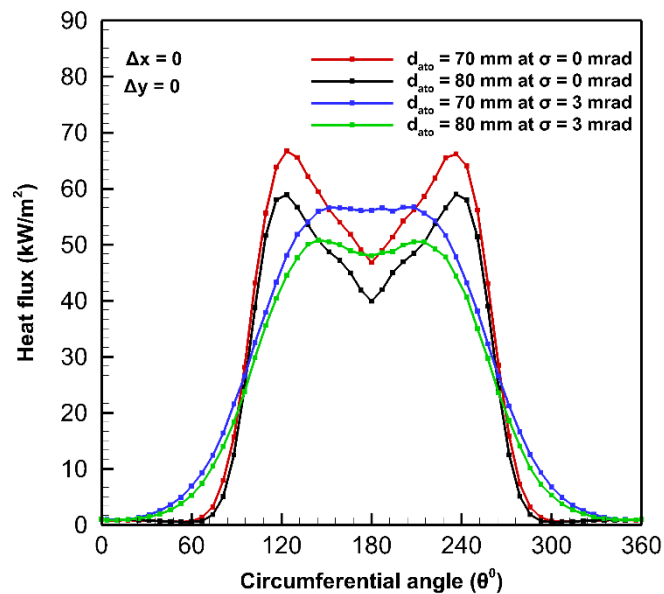


Fig. 5.4 Distribution of heat flux over the absorber tube for Δx = 0 and Δy =

0

Fig. 5.5 shows the variation in circumferential heat flux distribution over the absorber tube with absorber tube misalignment in the y-direction only (at $\Delta x = 0$) at slope error 3 mrad. As shown, the heat flux distribution is symmetrical and is significantly affected by the absorber tube dislocation. It can be observed that the peak flux over the absorber tube increases with an increase of absorber tube misalignment in the positive y-direction (at $\Delta y > 0$) and it decreases with an increase of absorber tube misalignment in the negative y-direction ($\Delta y < 0$). Due to absorber tube dislocation in the positive y-direction, the lower portion of the absorber tube comes closer to the focal point resulting in higher peak flux due to apparent higher concentration ratio. The reverse phenomenon is observed when the absorber tube is displaced in the negative y-direction.

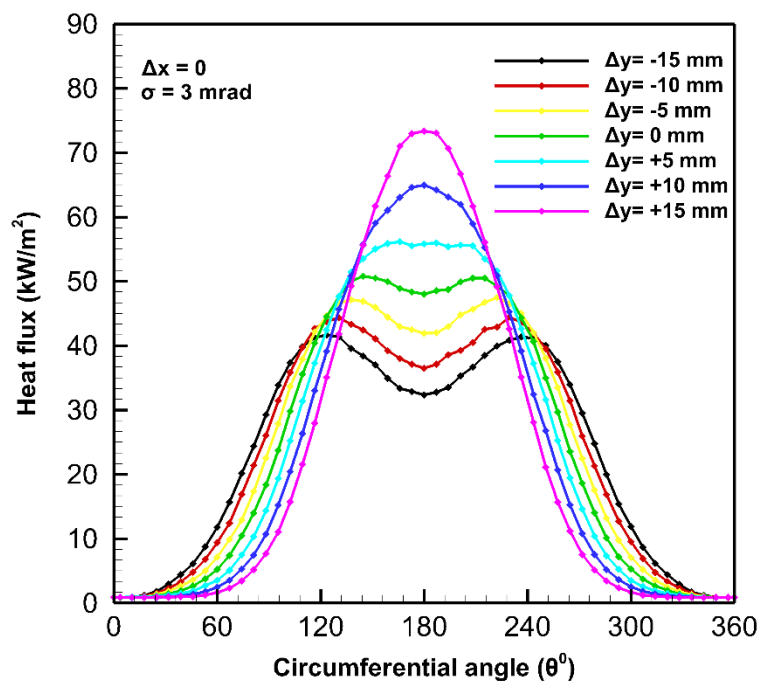


Fig. 5.5 Distribution of heat flux over the absorber tube for $\sigma = 3$ mrad at $\Delta x = 0$

Fig. 5.6 shows variation in circumferential heat flux distribution over the absorber tube with absorber tube misalignment in the x-direction with slope error 3 mrad. It can be seen that the distribution of heat flux is asymmetric in this case. The peak flux over the absorber tube increases with an increase of absorber tube misalignment in the x-direction (Δx). It is because of the fact that dislocation of absorber tube in x-direction makes the geometry of PTC asymmetric. It has also been studied that average heat flux over the absorber tube is not significantly affected by dislocation of absorber tube in either direction (x or y).

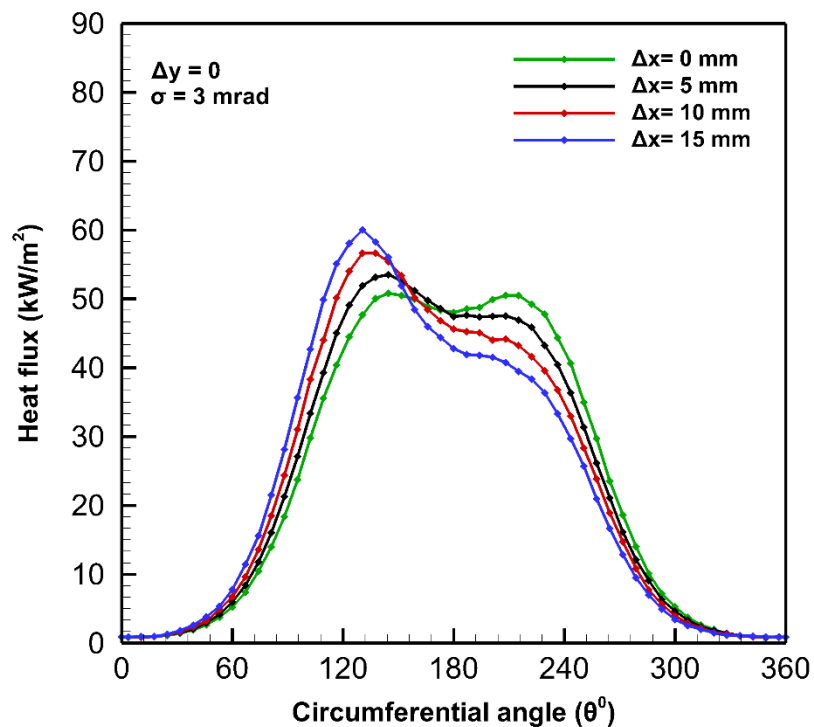


Fig. 5.6 Distribution of heat flux over the absorber tube for $\sigma = 3$ mrad at $\Delta y = 0$

5.3.3 Temperature distributions in the absorber tube

The temperature distribution in the absorber tube has been computed to know the effect of slope error and absorber tube dislocation on the temperature gradient ($\Delta T =$ difference in maximum and minimum temperature on absorber

tube surface). The results are presented in Fig. 5.7 (a) - (e). It is evident from Fig. 5.7 (a) and (b) that slope error of 3 mrad has almost no effect on the temperature gradient in the absorber tube for the perfectly aligned absorber. The absorber tube misalignment has a much greater effect on the temperature gradient in the absorber tube when slope error is zero. For example, the temperature gradient (ΔT) is 37.6 K when $\Delta x = 0$, $\Delta y = 0$, $\sigma = 0$, and the ΔT is 35.8 K when $\Delta x = 0$, $\Delta y = 0$ and $\sigma = 3$, and the ΔT is 59.7 K when $\Delta x = 15$ mm, $\Delta y = +15$ mm, $\sigma = 0$. The cumulative effect of slope error and absorber tube dislocation on temperature gradient is presented in Fig. 5.7 (c) – (d). It is observed that the temperature gradients are affected by absorber tube misalignment with slope error. The maximum temperature gradient is found for the case presented in Fig. 5.7 (e). The value of ΔT is 49 K when $\Delta x = 15$ mm, $\Delta y = +15$ mm, $\sigma = 3$ mrad. It is observed that variation in maximum temperature attained on the surface of the absorber tube is due to the heat flux distribution pattern on the tube under the influence of slope error and absorber tube dislocation.

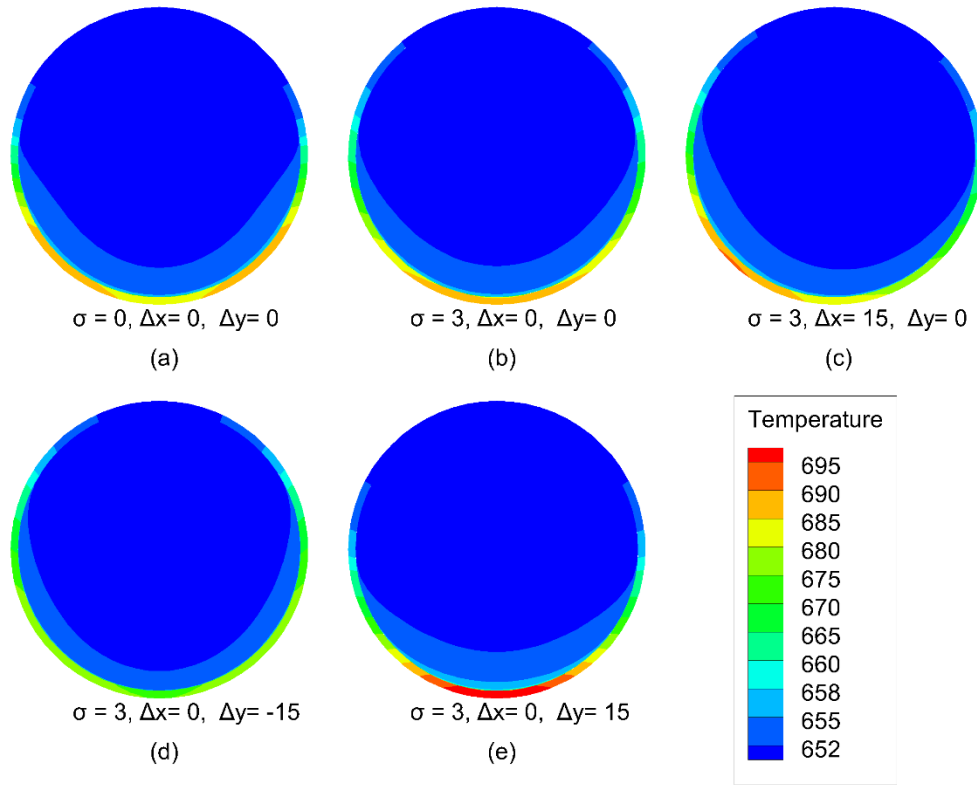


Fig. 5.7 Distribution of temperature in the absorber tube for $Re = 2.76 \times 10^5$, $T_{in} = 650$ K and $d_{ato} = 80$ mm (slope error (σ) is in mrad, Δx and Δy are in mm)

5.3.4 Collector efficiency

The thermal performance of the PTC has been evaluated. The effects of absorber tube misalignment and surface slope error on the thermal performance of PTC have been studied. The collector thermal efficiency has been calculated by using Eqn. (1.7). The overall collector efficiency has been calculated using Eqn. (1.4).

Fig. 5.8 and Fig. 5.9 show the variation of collector thermal efficiency with absorber tube misalignment and slope error for 80 mm and 70 mm diameter absorber tubes respectively (for the inlet conditions of volumetric flow rate $31.05 \text{ m}^3 \text{ h}^{-1}$ and inlet fluid temperature 650 K). It is observed that the collector thermal efficiency is slightly higher with 70 mm absorber tube than 80 mm diameter absorber tube for the range of absorber tube misalignment and slope

error considered in this study. It is because of lower heat losses from receiver to environment and higher value of average heat flux (due to higher geometrical concentration ratio) obtained with 70 mm diameter absorber tube due to its smaller size. It is found that the absorber tube misalignment in the lateral direction has almost no effect on the collector thermal efficiency. However, thermal efficiency is slightly affected by absorber tube dislocation in y-direction along the optical axis. The collector thermal efficiency increases with absorber tube misalignment in negative y-direction i.e. towards the trough and it decreases when the absorber is misaligned in positive y-direction i.e. away from the trough. It may be because of variation in the circumferential heat flux distribution over the absorber tube. It is found that the collector thermal efficiency of the PTC increases by up to 1.1% and 1.2% with 70 mm and 80 mm diameter absorber tubes respectively when Δy is -15mm. Thermal efficiency decreases by up to 3% and 2.4% with 70 mm and 80 mm diameter absorber tubes respectively for $\Delta y = 15$ mm. It is also evident from Fig. 10 that thermal efficiency drops by less than 1% for perfectly aligned absorber when surface slope error is 3 mrad.

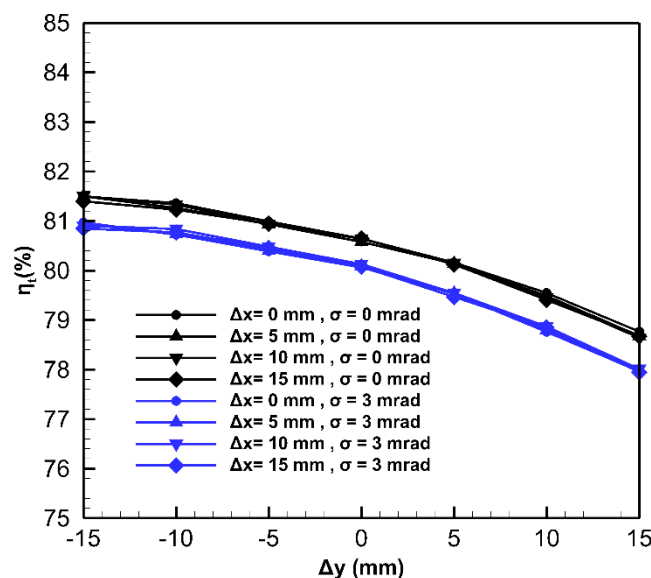


Fig. 5.8 Collector thermal efficiency Vs absorber tube misalignment for $d_{\text{ato}} = 80 \text{ mm}$

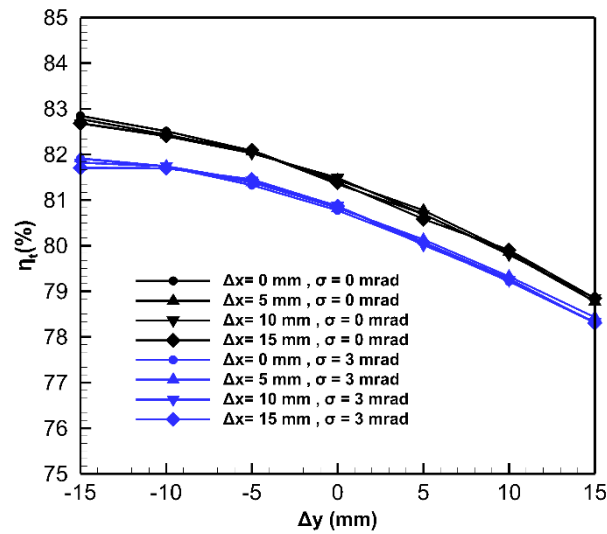


Fig. 5.9 Collector thermal efficiency Vs absorber tube misalignment for $d_{\text{ato}} = 70 \text{ mm}$

Fig. 5.10 and Fig. 5.11 show the variation in the overall collector efficiency of the PTC with absorber tube misalignment and slope error for 80 mm and 70 mm diameter absorber tubes respectively (for the inlet conditions of volumetric flow rate $31.05 \text{ m}^3 \text{ h}^{-1}$ and inlet fluid temperature 650 K). As seen, the overall collector efficiency is slightly higher with 70 mm absorber tube when the absorber is misaligned but surface slope error is zero. The effect of slope error on overall collector efficiency is greater in the case of 70 mm absorber tube than 80 mm tube in the absence of absorber tube misalignment because of the smaller size of 70 mm tube. For a perfectly aligned absorber, there is a drop of 3.5 % in overall collector efficiency with 70 mm diameter tube at slope error 3 mrad. The cumulative effect of absorber tube misalignment and slope error on overall collector efficiency is significant. But the effect is greater in 70 mm absorber tube than 80 mm diameter absorber tube. The overall collector efficiency with

70 mm tube decreases by up to about 11 % at slope error 3 mrad and $\Delta x = 15$ mm and $\Delta y = +15$ mm. Whereas for the same magnitude of slope error and absorber tube dislocation the overall efficiency decreases by up to 7 % with 80 mm diameter absorber tube.

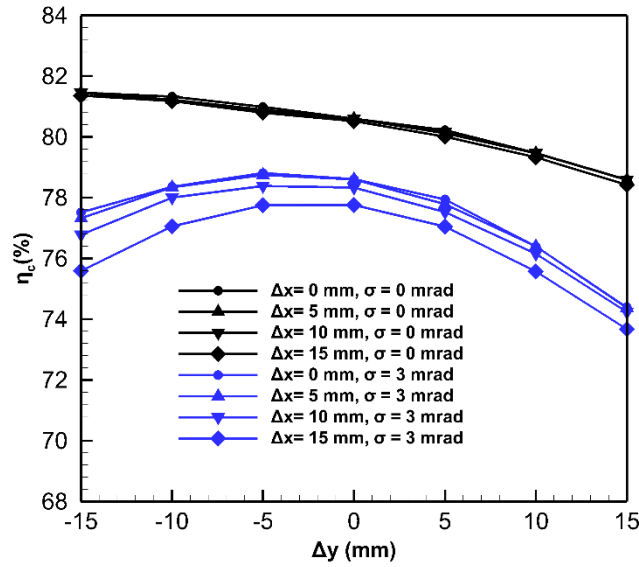


Fig. 5.10 Overall collector efficiency Vs absorber tube misalignment for $d_{\text{ato}} = 80$ mm

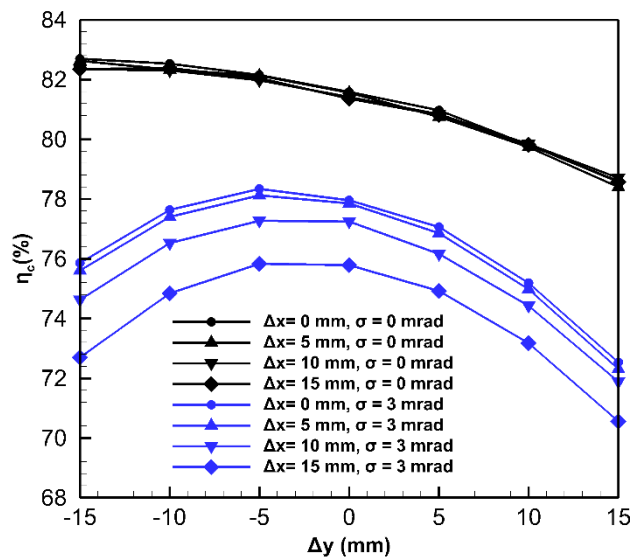


Fig. 5.11 Overall collector efficiency Vs absorber tube misalignment for $d_{\text{ato}} = 70$ mm

Fig. 5.12 shows the variation in the circumferential temperature gradients (ΔT) (the difference between the maximum and minimum temperature) in the surface of absorber tube with Reynolds number for 80 mm diameter absorber tube at a slope error of 3 mrad. It can be seen from the plot that temperature gradient decreases with an increase in the value of the Reynolds number. The absorber tube misalignment has a greater effect on temperature gradients at lower values of Reynolds number. Temperature gradient increases when the absorber tube is dislocated in the positive y-direction and it decreases with absorber tube dislocation in the negative y-direction. For example, for perfectly aligned absorber ΔT is 35 K, and ΔT is 28.2 K when dislocation of absorber tube is 15 mm in the negative y-direction and ΔT is 48.9 K for the absorber tube dislocation equal to 15 mm in the positive y-direction. The practical safe operating conditions for PTC are : $Re = 2.76 \times 10^5$ (volumetric flow rate of HTF $31.05 \text{ m}^3 \text{ h}^{-1}$ [19]) and ΔT should be lower than 50 K [22, 49, 102]. If ΔT is more than 50 K then higher thermal stresses are induced in the tube, which is much higher at higher values of ΔT may cause damage to the heat collecting element. It can be observed that at $Re = 2.76 \times 10^5$, the temperature gradient (ΔT) is about 30.1 K for $\Delta y = -15 \text{ mm}$ and ΔT is 52.9.7 K for $\Delta y = +15 \text{ mm}$. It can be stated from the results presented in Fig. 12 that absorber tube dislocation should not be more than +10 mm for practical working conditions of PTC.

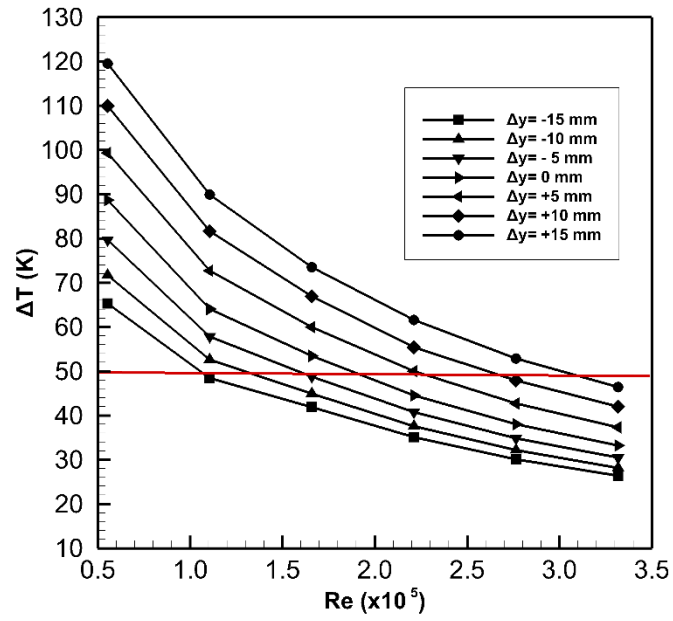


Fig. 5.12 Temperature gradient in the absorber tube Vs. Re for 80 mm diameter absorber tube at $\sigma = 3$ mrad,

CHAPTER 6

HEAT TRANSFER ENHANCEMENT IN PTC USING FINNED ABSORBER TUBE

This chapter presents the improvement of heat transfer in the absorber tube using fins. As discussed in chapter 2, the improved heat transfer in the absorber tube improves the thermal efficiency of the collector hence the overall collector efficiency.

In this work, longitudinal fins are introduced inside the absorber tube of the PTC receiver to enhance the heat transfer. Since the lower portion of the receiver receives concentrated solar power, employing the fin at this location may lead to a higher heat transfer. Therefore, the fins are introduced at the lower portion of the absorber tube. Two different finned absorber tubes along with unfinned absorber tube are studied to compare the results and estimate the improvement in the heat transfer. The three absorber tubes are termed as AT1, AT2, and AT3 as shown in Fig. 6.1 (a), (b) and (c) respectively. AT1 is an unfinned absorber tube. AT2 is a finned absorber tube with one longitudinal triangular fin employed at the inner lower portion of the absorber tube. AT3 is also a finned absorber tube but has two longitudinal rectangular fins placed at the two peak flux locations on the absorber tube [70]. The geometrical parameters of the PTC system considered for the are presented in Table 4.1

Table 6.1 Geometrical properties of the PTC system

Parameter	Symbol	Value
Aperture width	w	5 m

Length of receiver	L	4 m
Glass tube inner diameter	d_{gi}	109 mm
Glass tube outer diameter	d_{go}	115 mm
Absorber tube inner diameter	d_{ri}	66 mm
Absorber tube outer diameter	d_{ro}	70 mm
Focal length	F	1.84 m

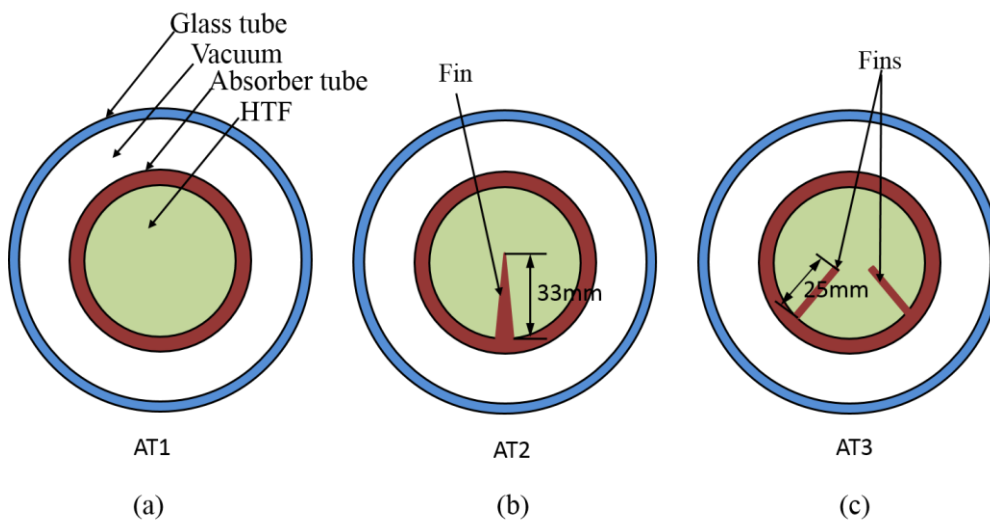


Fig. 6.1 Cross sectional view of receiver (a) AT1 (b) AT2 (c) AT3

6.1 Optical analysis

The optical simulation was carried out for the PTC system for the geometrical parameters given in Table 6.1 with the optical properties presented in Table 6.2. Sun has been modeled as a Gaussian distribution with a cone angle of 2.6 mrad [22]. An ideal tracking system of the PTC system was assumed where the direct normal irradiation was taken as 1000W/m^2 for all ray tracing simulations. Both the slope and specularity error of the mirror were considered as 3 mrad [22, 103].

Table 6.2 Optical properties of the PTC system [90]

Parameter	Symbol	Value
Absorber tube absorptivity	α_r	0.92
Absorber tube reflectivity	ρ_r	0.08
Glass tube transmissivity	τ_g	0.935
Glass tube reflectivity	ρ_g	0.045
Mirror reflectivity	ρ_m	0.93
Mirror transmissivity	τ_m	0

6.2 Thermal analysis

The thermal analysis of the PTC receiver with the three different absorber tubes is carried out using the method specified in section 3.2. The governing equations specified in the section 3.2.1 have been solved using FVM with boundary conditions specified in section 3.2.2. A structured mesh of the geometry has been generated as shown in Fig. 6.2 to carry out the FVM analysis. A very fine mesh has been generated near the wall to capture the high velocity and temperature gradients. Second order upwind scheme was used for discretizing the momentum and energy equation. Turbulent kinetic energy, turbulent dissipation rate, and discrete ordinate equations are discretized using first-order upwind scheme. The convergence criteria for scaled residuals are taken as 10^{-6} for all the equations.

Grid-independent test was carried out to determine the optimum mesh size. The mesh with 857,472, 1,003,574 and 2,386,271 cells are found to be optimum for AT1, AT2, and AT3 respectively.

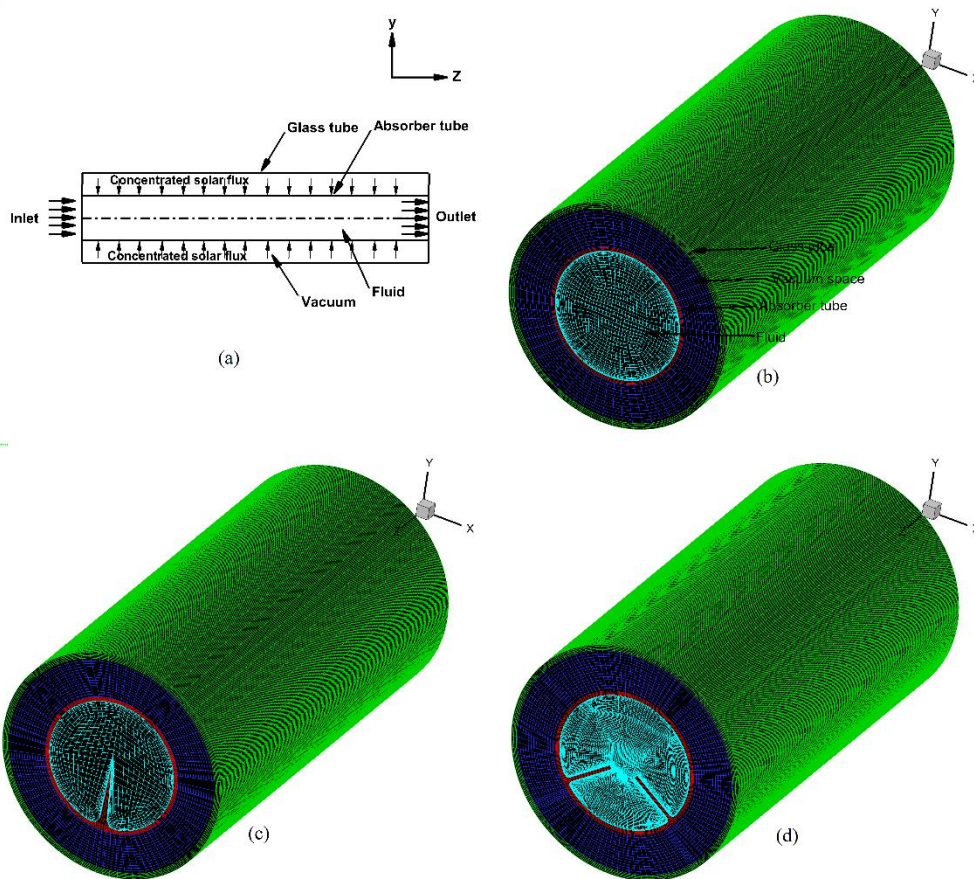


Fig. 6.2 Boundary conditions and mesh of PTC receiver (a) boundary conditions (b) AT1 (c) AT2 (d) AT3

6.3 Results and discussion

The simulated results of the PTC with the three absorber tubes are presented and compared. The slope error considered in the present study is 3 mrad as experimentally determined in the study of Wendelin [103]. Fig. 6.3 shows the heat flux distribution on the circumference of the absorber tube for the parameters of the PTC specified in Table 6.1 and Table 6.2. It can be observed that the value of heat flux is high on the lower half portion of the absorber tube due to concentrated solar flux and low on the upper half portion due to direct sunlight. A non-linear heat flux distribution is observed over the absorber tube

leads to higher temperature gradients. These higher temperature gradients cause thermal stresses, hence distortion in the absorber tube.

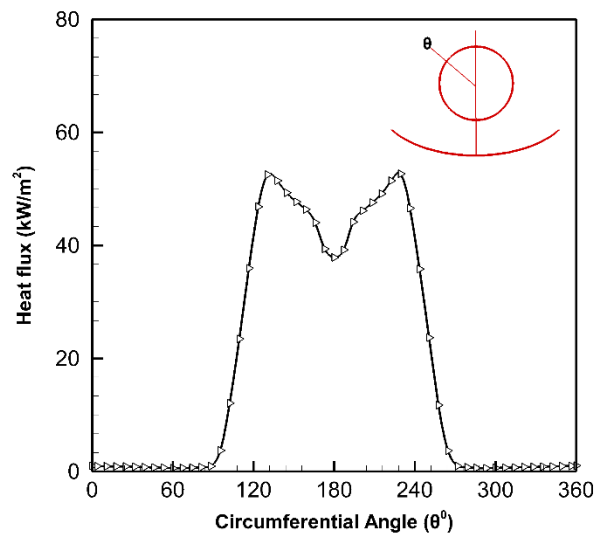


Fig. 6.3 Distribution of heat flux over absorber tube

The temperature gradients in the three absorber tubes are compared in Fig. 6.4 for the HTF volumetric flow rate $31.05 \text{ m}^3/\text{s}$ and inlet temperature 600 K as considered in studies of Mwesigye, Huan [22] and Forristall [19]. As observed the temperature gradients in the absorber tubes follow the trend of the heat flux distribution. In comparison to the upper half portion, the temperatures in the lower half portion of the absorber tube are higher for all the three cases. The reason for this is non-uniform heat flux distribution over the absorber tube. As seen in Fig. 6.4 (a), (b) and (c) the temperature gradients in the AT1, AT2 and AT3 are almost the same. However, the sizes of confederal zones having constant temperature vary in three cases. The difference between the maximum and minimum temperature in the absorber tube is 28 K for all three cases, it is within the allowable limits for the safe operation of the PTC receiver [49]. In AT3, the longitudinal fins are employed at the location of maximum heat flux

on the absorber tube the heat transfer rate is higher resulting in a narrow high-temperature zone in the AT3.

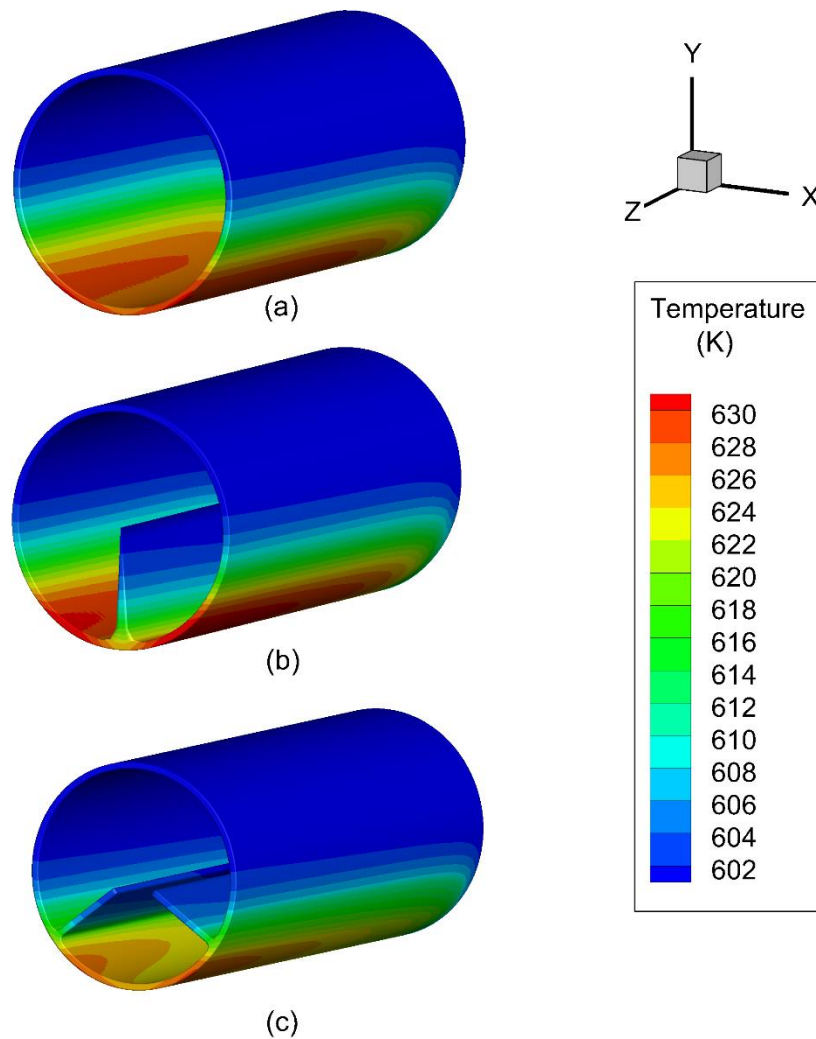


Fig. 6.4 Temperature distribution over (a) AT1 (b) AT2 (c) AT3

Fig. 6.5 shows the variation of average Nusselt number and average friction factor with Reynolds number for the inlet temperature of 600 K. The average Nusselt number is calculated by using Eqn. (6.1).

$$Nu = \frac{\bar{h} d_h}{\lambda} \quad (6.1)$$

Where \bar{h} is the average heat transfer coefficient and it is obtained by using Eqn. (6.2).

$$\bar{h} = \frac{Q_a}{A(T_{wall} - T_{htf})} \quad (6.2)$$

Where Q_a is the heat absorbed by the HTF, calculated by using Eqn. (6.3).

$$Q_a = \dot{m}C_p(\bar{T}_o - \bar{T}_i) \quad (6.3)$$

The friction factor (f) is calculated using Eqn. (6.4). Where ΔP_l is the pressure drop per unit length

$$f = \frac{\Delta P_l d_h}{\frac{1}{2} \rho u^2} \quad (6.4)$$

As shown in Fig. 6.5, for the three absorber tubes, lower average Nusselt numbers are obtained at the lower Reynolds numbers and the Nusselt number increases with increase in Reynolds number. It can be observed that the values of average Nusselt number for the finned absorber tubes (AT2 and AT3) are higher in comparison to the un-finned tube (AT1) indicating enhanced heat transfer in the finned absorber tubes. Higher values of average Nusselt number for the absorber tube AT3 (with two longitudinal fins) are obtained than the values of the Nusselt number obtained for AT2. It indicates that a higher amount of heat is transferred to the fluid in absorber tube AT3 due to the two longitudinal fins employed at the peak flux locations on the absorber tube. In comparison to AT1, the maximum increase in Nusselt number in the AT2 and AT3 is 18.3% and 40.1% respectively. For the three absorber tubes, the maximum value of a Nusselt number is obtained at Reynolds number equal to 2.82×10^5 . As shown in Fig. 6.5, for the three absorber tubes, the higher average friction factors are observed at the lower Reynolds numbers and friction factor decreases with the increase in values of Reynolds number. A similar trend for friction factor is reported in the study of Cheng, He [54]. Slightly higher values of friction factor are observed in the finned absorber tubes (AT2 and AT3) in

comparison to the un-finned absorber tube (AT1) due to the higher pressure drop in the finned absorber tubes. No significant difference in the value of the average friction factor is observed between the absorber tube with a single fin and tube with two fins.

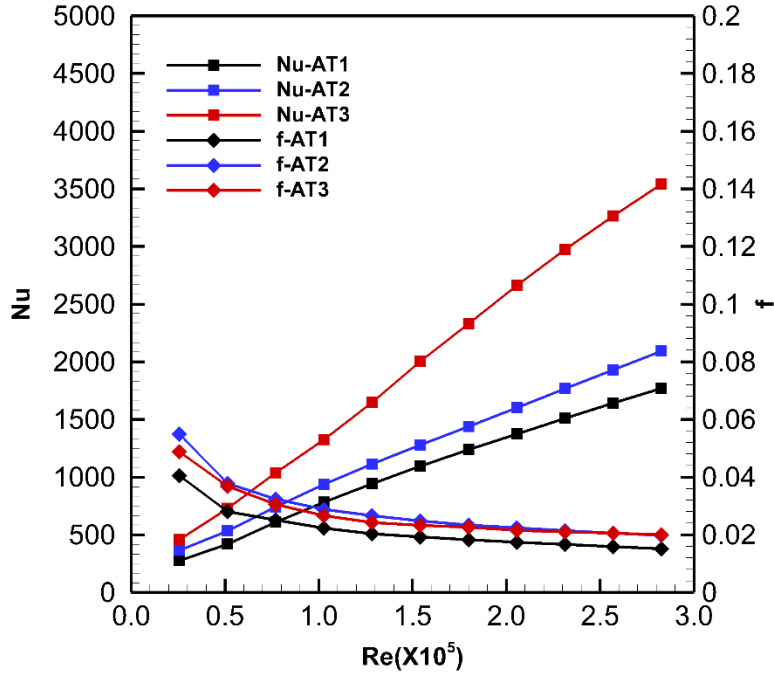


Fig. 6.5 Variation of Nu and f with Reynolds number

The overall improvement in the heat transfer performance of a PTC can be examined by using performance evaluation criteria (PEC) of the PTC receiver for a given pumping power [54, 104]. The PEC is given in equation Eqn. (6.5).

$$PEC = \frac{\left(\frac{Nu_f}{Nu_{uf}}\right)}{\left(\frac{f_f}{f_{uf}}\right)^{1/3}} \quad (6.5)$$

Where Nu_{uf} and f_{uf} are an average Nusselt number and average friction factor for the un-finned tube. Nu_f and f_f are an average Nusselt number and average friction factor for the finned tube. For a given pumping power, with the finned

absorber tubes, the comprehensive heat transfer performance of the PTC receiver improves, if the values of the PEC are above one.

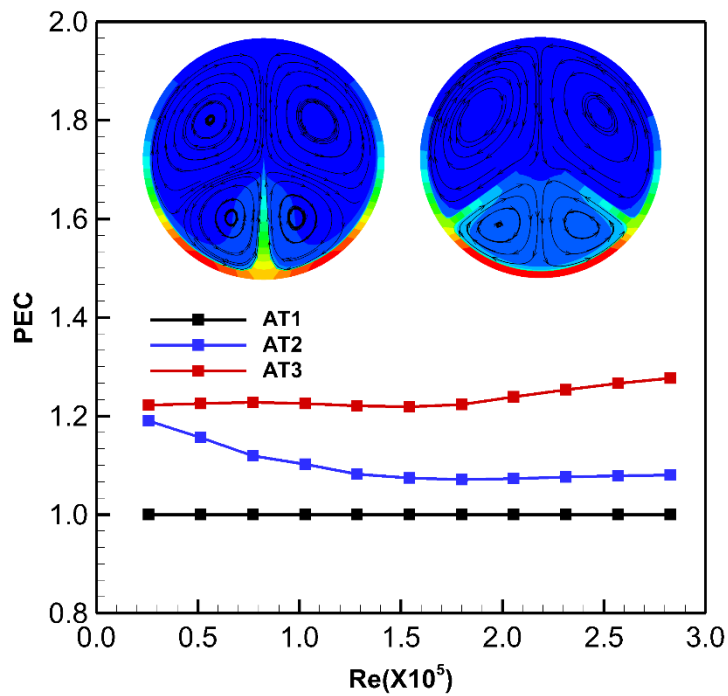


Fig. 6.6 Variation of PEC with Reynolds number.

Fig. 6.6 shows the variation of PEC with Reynolds number for the three absorber tubes. As observed, the values of the PEC for AT2 and AT3 are above one whereas the value of PEC is one for the un finned absorber. It implies that the comprehensive heat transfer performance is improved in both the finned absorber tubes. The values of the PEC for the AT3 are higher in comparison to the AT2. No significant variation in the PEC is observed with Reynolds number in case of absorber tube with two fins. The maximum value of PEC is 1.19 at the Reynolds number 0.25×10^5 in case of AT2 whereas in case of AT3 the maximum value of PEC is 1.28 at the Reynolds number 2.83×10^5 . It indicates that employing two longitudinal fins at the location of peak flux in the absorber tube is more beneficial than a single longitudinal fin.

CHAPTER 7

RHOMBUS TUBE ABSORBER

This chapter presents the improvement of the CR by using rhombus tube absorber. As the PTC is a line focused concentrated solar power collector. The PTC can be considered as a two dimensional system for the optical analysis provided Sun rays are perpendicular to the aperture area (i.e. a perfect tracking system) [12]. For simplicity, a two dimensional geometry is considered for the analysis in the present work. The cross section view of the PTC is shown in Fig. 7.1.

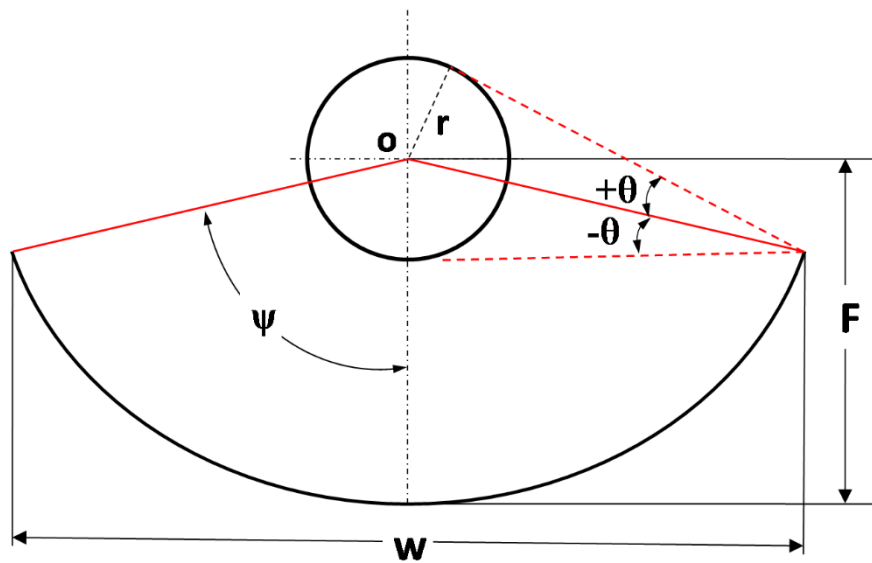


Fig. 7.1 Cross section view of the parabolic trough collector.

The concentrator follows the curvature of the parabola generated by the Eqn. (7.1) for the given coordinates (X, Y) and focal length (F) as shown in Fig. 7.1 and Fig. 7.2. Eqn. (7.2) has been obtained from the geometry of Fig. 7.2, for calculating the rim angle (ψ) . Also from the geometry of Fig. 7.2, the local rim angle (ψ_p) at any point $p (X, Y)$ on the curvature of the parabola can be obtained by using Eqn. (7.3).

$$Y = F - \frac{X^2}{4F} \quad (7.1)$$

$$\psi = \tan^{-1} \frac{w/2}{Y_w} = \tan^{-1} \frac{w/2}{\left(F - \frac{(w/2)^2}{4F}\right)} \quad (7.2)$$

$$\psi_p = \tan^{-1} \frac{X}{Y} = \tan^{-1} \frac{X}{F - \frac{X^2}{4F}} \quad (7.3)$$

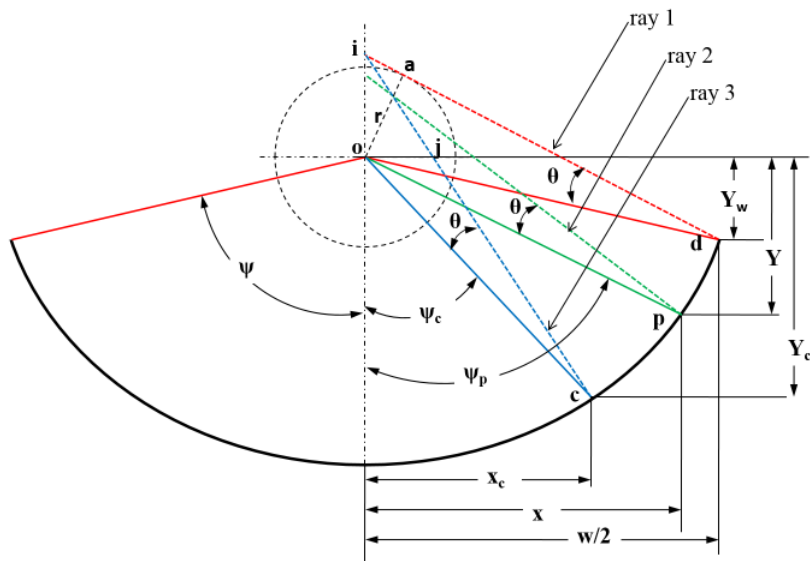


Fig. 7.2 Ray projections from the mirror.

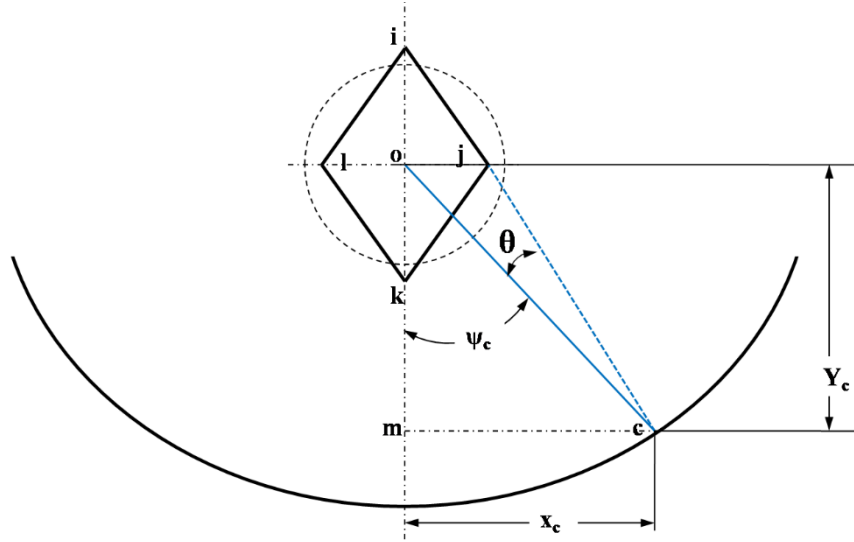


Fig. 7.3 Schematic of rhombus tube absorber.

The half acceptance angle (θ) can be defined as the maximum deviation of the ray that can be allowed in the collector while the absorber is receiving whole energy reflected from the concentrator as shown in Fig. 7.1 [12]. It is calculated by using the absorber tube radius (r), aperture width (w) and focal length (F) in the Eqn. (7.4) [12] obtained from the triangle 'doa' in Fig. 7.2.

$$\theta = \sin^{-1} \frac{r}{\sqrt{\left(\frac{w}{2}\right)^2 + Y_w^2}} = \sin^{-1} \frac{r}{\sqrt{\left(\frac{w}{2}\right)^2 + \left(F - \frac{(w/2)^2}{4F}\right)^2}} \quad (7.4)$$

From Eqn. (1.3) the CR of the PTC can be increased with smaller size circular absorber, which results in a lower acceptance angle. Thus, the amount of reflected solar energy intercepted by the absorber reduces (i.e. low intercept factor) because some of the rays escape the absorber. The possibility of improving CR of the PTC (circular absorber) by using non-circular absorber without changing the acceptance angle can be explored. In the present work, a rhombus tube absorber has been proposed. A rhombus tube absorber should be placed in such a way that the larger diagonal of the rhombus coincides with the

focal axis and its center merges with the focal point of the reflector (Fig. 7.3) so that a smaller shadow is produced on concentrator and a larger effective surface area is available for reflected rays. The design of rhombus tube absorber is discussed in subsequent sections.

7.1 Application of edge ray principle

The size of the rhombus tube absorber should be big enough to receive all the rays reflected from concentrator for better efficiency. The edge ray principle [105] is applied to define the dimensions of the rhombus tube absorber such that all the rays reflected from the concentrator fall on it. If the incoming rays are parallel and normal to the aperture area, all the rays reflect on the focus of the concentrator. In real conditions, the reflected rays deviate and spread around the focus due to the finite size of Sun, geometric and optical errors of the system [106]. The edge ray is defined as a maximum deviated ray from the focus. If the edge rays are intercepted by the absorber, it ensures that all the inner rays will also be intercepted [12]. If the deviation of edge ray is equal to the half-acceptance angle (θ) as shown in Fig. 7.1, all the reflected rays from the concentrator will fall on the absorber. Thus, the study of edge ray ($+\theta$) is sufficient to calculate the size of the absorber for the rim angle less than 90° .

As shown in Fig. 7.2, ray1 is the maximum deviated ray from the edge of the concentrator, which intersects the focal axis at point 'i'. Therefore, the point 'i' is considered as one of the corners of rhombus so that the maximum deviated ray (ray1) will intersect with rhombus tube absorber. The opposite corner of a rhombus ('k') will be the mirror image of point 'i' about focus 'o' on the focal axis so that the center of the rhombus coincides with the focus. The

distance between point 'o' and point 'i' (oi) is calculated using Eqn. (7.5) which is obtained from the triangle 'iod' in Fig. 7.2 using sine law.

$$\frac{oi}{\sin\theta} = \frac{\sqrt{\left(\frac{W}{2}\right)^2 + Y_w^2}}{\sin(\psi - \theta)} \quad (7.5)$$

As the rim angle considered in this study is less than 90° , all the reflected rays from the edge of the concentrator will lie between point 'i' and point 'k'. Also, the rays (ray 2) reflected from any point 'p' will lie between point 'i' and point 'k' for the local rim angle (ψ_p) varies between $\psi_c \leq \psi_p \leq \psi$, where ψ_c is critical rim angle at critical point 'c'. At the critical point 'c' the maximum deflected ray (ray 3) intercept with the optical axis at point 'i'. For the condition, local rim angle $\psi_p < \psi_c$, the maximum deflected ray will cross the focal axis above point 'i' hence, missing the interception with rhombus absorber. The distance 'oi' is also calculated from Eqn. (7.6) obtained from the triangle 'ioc' in Fig. 7.2 using sine law.

$$\frac{oi}{\sin\theta} = \frac{\sqrt{X_c^2 + Y_c^2}}{\sin(\psi_c - \theta)} \quad (7.6)$$

The Eqn. (7.7) is obtained by equating right-hand side terms of Eqn. (7.5) and Eqn. (7.6) where the unknown terms are X_c and Y_c . The Eqn. (7.7) is converted to a fourth order quadratic equation in terms of X_c using Eqn. (7.1). Eqn. (7.8) is the modified version of Eqn. (7.7). The steps are given in appendix B.

$$\frac{\sqrt{\left(\frac{W}{2}\right)^2 + Y_w^2}}{\sin(\psi - \theta)} = \frac{\sqrt{X_c^2 + Y_c^2}}{\sin(\psi_c - \theta)} \quad (7.7)$$

$$\begin{aligned}
& \frac{1}{16F^2} \sin(\psi - \theta) X_c^4 \\
& - \left[\frac{\sqrt{\left(\frac{W}{2}\right)^2 + Y_w^2}}{4F} \sin \theta - \sin(\psi - \theta) \right. \\
& \left. + \frac{1}{2} \sin(\psi - \theta) \right] X_c^2 \\
& - \left(\sqrt{\left(\frac{W}{2}\right)^2 + Y_w^2} \right) \cos \theta X \\
& + F \left(\sqrt{\left(\frac{W}{2}\right)^2 + Y_w^2} \right) \sin \theta + F^2 \sin(\psi - \theta) \\
& = 0
\end{aligned} \tag{7.8}$$

By solving the Eqn. (7.8) the value of X_c is obtained which is further used for calculating Y_c and ψ_c using Eqn. (7.1) and Eqn. (7.2) respectively. For the condition, $\psi_p < \psi_c$, the maximum positive deflected ray will fall outside the region between point 'i' and point 'k'. Another diagonal of the rhombus is determined in such a way that the reflected rays from the region having local rim angles below critical point ($\psi_p < \psi_c$) will also intercept the rhombus. The maximum positive deflected ray from point 'c' intersects the horizontal line passing through the focus at point 'j' as shown in Fig. 7.3. Therefore, the point 'j' is considered as another corner point of the rhombus and opposite corner 'l' will be the mirror point about the focus 'o'. Now the distance between point 'o'

and point 'j' (oj) is calculated from the similar-triangles 'ioj' and 'imc' (see Fig. 7.3) by using Eqn. (7.9).

$$\frac{oi}{im} = \frac{oj}{X_c} \quad (7.9)$$

Finally, the points i, j, k and l forms the desired corners of the rhombus where all the rays reflected from the concentrator will be intercepted. The optimum size of the rhombus can be obtained from Eqn. (7.8) by specifying values of acceptance angle, focal length and rim angle of PTC. The side of the rhombus (s) can be calculated by using Eqn. (7.10) obtained from the triangle 'ioj' using the Pythagorean theorem. The concentration ratio of the PTC with rhombus tube absorber can be calculated by using Eq. (7.11).

$$s = \sqrt{io^2 + oj^2} \quad (7.10)$$

$$CR = \frac{wL}{4sL} = \frac{w}{4s} \quad (7.11)$$

7.2 Dimensions of the rhombus tube absorber.

In the previous sections, a methodology to obtain the dimensions of the rhombus tube absorber has been described. By using the proposed method, the dimensions of the rhombus tube absorber are obtained for the commercially available troughs [12] and are presented in Table 7.1. The percentage decrease in absorber's size is calculated using Eqn. (7.12).

$$\begin{aligned} \% \text{ decrease in absorber's size} &= \frac{(2\pi rL - 4sL)100}{2\pi rL} \\ &= \frac{(2\pi r - 4s)100}{2\pi r} \end{aligned} \quad (7.12)$$

It is evident from Table 7.1 that size of rhombus tube absorber is smaller than the size of circular tube absorber for all the troughs. Percent increase in CR with rhombus tube absorber is also listed in Table 7.1.

Table 7.1 CR of commercially available troughs with circular tube absorber and rhombus tube absorber for the same acceptance angle

PTC	'w' (mm)	'f' (mm)	'r' (mm)	' ψ ' ($^{\circ}$)	' θ ' ($^{\circ}$)	CR (circular tube)	's' (mm)	CR (rhombus tube)	% decrease in absorber's size	% increas e in CR
LS1	2500	680	21	85	0.96	18.9	26.5	23.6	19.7	24.6
LS2	5000	1400	35	83.5	0.8	22.7	45.1	27.7	18.0	22.0
LS3	5760	1710	35	80	0.69	26.2	47.4	30.4	13.8	16.0
Acurex	1830	457	15.9	90	1	18.3	19	24.1	23.9	31.5

7.3 Comparison of results

Variation in concentration ratio with rim angle is plotted in Fig. 7.4 for rhombus and circular tube absorbers for LS3 trough (focal length = 1.71 m, half acceptance angle = 0.69°). Fig. 7.4 also shows the percentage change in CR. It can be observed from Fig. 7.4 that the maximum gain in concentration ratio with rhombus absorber is around 31.5% at rim angle 90° . It is also evident that the gain in concentration ratio with rhombus absorber decreases with a decrease in rim angle. The CR for both absorbers is same at rim angle 72.5° . There is no gain in concentration ratio with rhombus absorber for values of rim angle below 72.5° . It is not advisable to use rhombus tube absorber in place of the circular absorber for the values of rim angle below 72.5° . This may be because the surface area of rhombus tube absorber increases due to a decrease in rim angle hence concentration ratio is decreased. At 72.5° value of rim angle, the surface area of the rhombus tube absorber becomes equal to the surface area of the circular absorber, therefore, there is no gain in the concentration ratio. With rim angle less than 72.5° , the surface area of rhombus tube absorber will become

higher than the surface area of the circular absorber, resulting in lower concentration ratio than the circular absorber.

Ray tracing with SolTrace software is done for circular and rhombus tube absorbers employed in the LS3 collector for the parameters shown in Table 7.1. Sun shape has been modeled using Gaussian distribution, considering 2.6 mrad as sun cone angle [22, 37] for all the simulations. Specularity and tracking errors have also been considered.

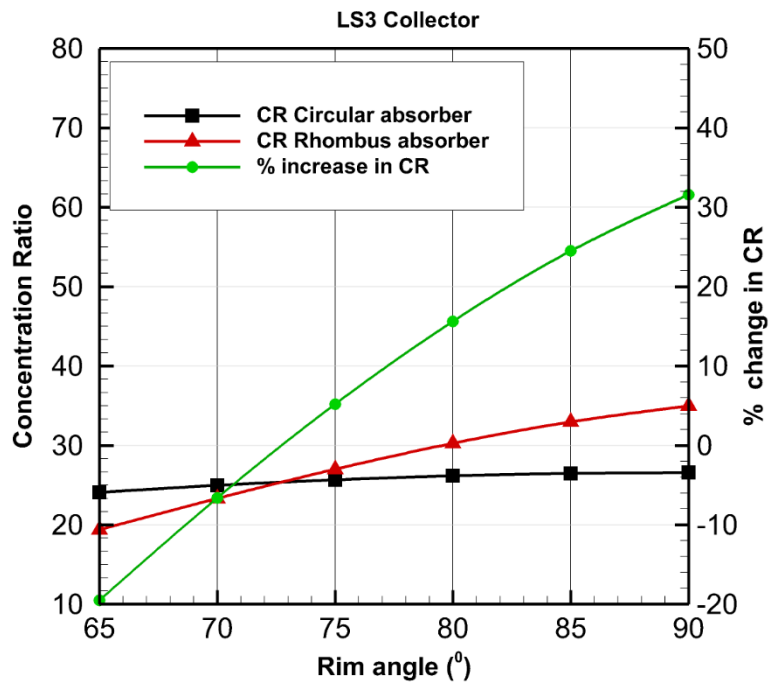


Fig. 7.4 Comparison of the concentration ratio of rhombus tube absorber with circular tube absorber for the LS3 collector, $F = 1.7\text{m}$; $\theta = 0.69^\circ$.

In Fig. 7.5 the variations in intercept factor and average flux with mirror specularity errors have been plotted for rhombus and circular tube absorbers. The range of mirror specularity error is considered from 0 to 5 mrad as mentioned in the study of (Mwesigye, Huan [22]). It is observed that there is no

significant change in intercept factor with specular error for both the absorbers. And the intercept factor is almost the same for both the absorbers. It can be seen from Fig. 7.5 that the value of average heat flux on the rhombus tube absorber is higher than circular absorber. Although the specular error has little effect on the average heat flux in case of both absorbers.

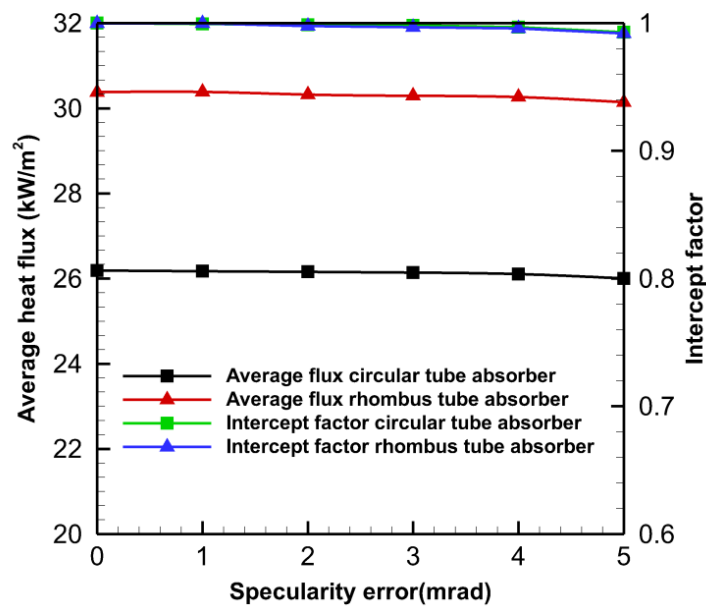


Fig. 7.5 Intercept factor and average flux Vs specularity error at tracking error zero.

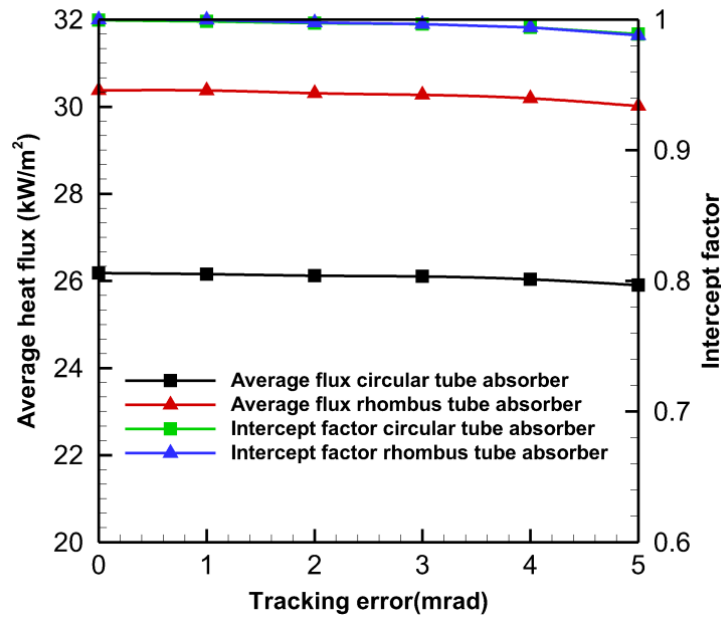


Fig. 7.6 Intercept factor and average flux Vs tracking error at specularity error of 3 mrad.

Fig. 7.6 shows the variations in intercept factor and average heat flux with tracking error at a constant value of specularity error 3 mrad. It can be seen that similar trends for intercept factor and average heat flux as observed in Fig. 7.5 are obtained.

From Fig. 7.5 and Fig. 7.6 it is observed that the specularity error and tracking error have little effect on the intercept factor and average heat flux in both absorbers. Another observation is that the higher value of average heat flux is obtained with rhombus absorber whereas the intercept factor is almost the same for both the absorbers. Thus a higher average surface temperature may be obtained with rhombus absorber with the same intensity of solar energy incident on the PTC

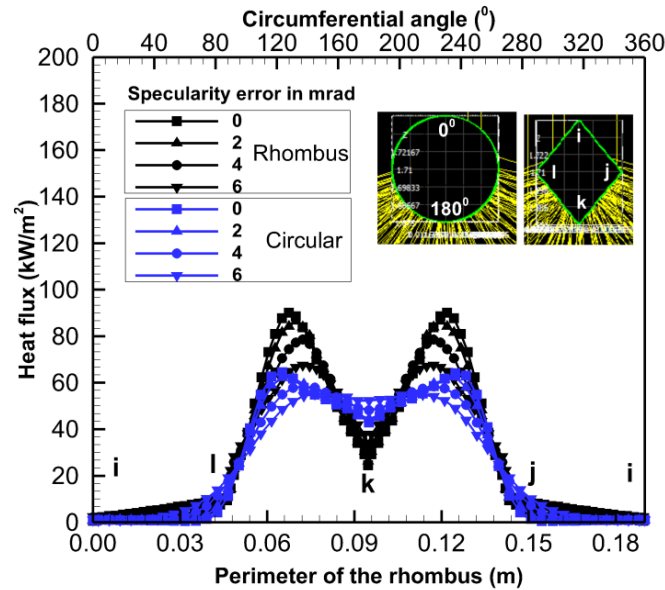


Fig. 7.7 Variation of the local heat flux over the absorber tube with specular error at tracking error zero

The variation in local heat flux over rhombus and circular tube absorbers with specular error for the LS3 collector is shown in Fig. 7.7. As observed, the peak local flux over the rhombus tube absorber is higher for a whole range of specular error considered in the present study. It is also noted that peak local flux decreases with increase in specular error in case of both the absorbers. It may be because of the widespread of the beam at high specular errors.

Fig. 7.8 shows the variation in local heat flux over rhombus and circular tube absorbers with tracking error, at 3 mrad mirror specular error, for the LS3 collector. It is observed that local heat flux distribution over both tube absorbers is symmetrical in the absence of any tracking error. Heat flux distribution becomes more asymmetrical with an increase in tracking error for both the absorbers. It is also noted that peak local flux is higher in rhombus tube absorber for all values of tracking error.

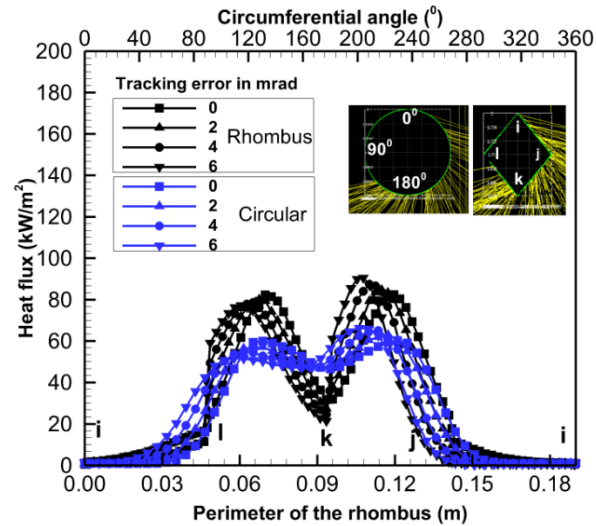


Fig. 7.8 Variation of the local heat flux over the absorber tube with tracking error at specularity error of 3 mrad.

It can be summarized that the higher value of local peak flux is obtained with rhombus tube absorber in the absence/presence of specularity and tracking errors. The high peak flux leads to higher temperature gradients in the absorber tube (Mwesigye, Huan [22]). The higher temperature gradients result in thermal stresses causing deflection in the absorber tube. But the temperature gradients are lower at higher fluid velocities in the absorber tube ([Mwesigye, Huan [22]]). Because of the smaller cross-sectional area in the rhombus tube absorber, the fluid velocity in the rhombus tube absorber may be higher than circular tube absorber, for a given fluid flow rate. The higher fluid velocity in the rhombus absorber may decrease the temperature gradients in the rhombus tube absorber. However, a detailed heat transfer analysis is required to quantify the temperature gradients in the rhombus absorber tube which is beyond the scope of the present work.

CHAPTER 8

CONCLUSION AND FUTURE RESEARCH

8.1 Conclusion

This study presents the results of optical and thermal analysis for a parabolic trough collector system with absorber tube misalignment and surface slope error of mirror. LS2 collector and Sener trough 2 collector were considered for the study. The simulations have also been performed for the parabolic trough collector with finned absorber tube. Rhombus tube absorber has been proposed for higher concentration ratio. The simulations have been performed by coupling MCRT and FVM.

It can be concluded that the receiver position error substantially influences the heat flux distribution on the absorber tube and significantly affects the thermal performance of the receiver. The temperature distribution on the absorber tube in the circumferential direction follows the pattern of heat flux distribution, but it is flatter than the heat flux distribution. The maximum temperature and the non-uniformity of the temperature on the absorber tube increase with an increase in receiver position error in the positive y-direction and these parameters decrease with increase in receiver position error in the negative y-direction.

In the case of the LS2 collector, the variations in values of the optical efficiency are negligible for the equal amount of displacement of the receiver either in positive or in the negative y-direction from the ideal position. The optical efficiency drops by 2% when the receiver is offset from the focus by

1.63% of its focal length in the y-direction. It is found that the optical efficiency decreases by 4 % when the receiver is displaced from the focus by 1.63% of its focal length in the x-direction. The maximum drop of 32% in optical efficiency is observed when the receiver is eccentric from the focus by 1.63% of the focal length in both lateral directions.

The collector efficiency is found to be around 79% when the receiver is concentric with the focus of the trough. No significant variation in the collector efficiency is observed when the receiver is displaced by 1.63% of the focal length from the focus of the trough in the negative y-direction. The variation in the thermal efficiency is high (14%) when the receiver is displaced by 1.63% of the focal length from the focus in the positive y-direction. Therefore, the displacement of the receiver in the y-direction (away from the trough) is more critical in comparison to the x-direction. The drop in the efficiency is more (28%) when the receiver is displaced by 1.63% of the focal length from the focus in both x and y-directions. Therefore, it can be concluded that the receiver position error has a significant effect on collector efficiency.

In case of Sener trough 2, it has been found that the intercept factor does not change at all under influence of absorber tube misalignment (within the range considered in the present work) in the absence of slope error. It was shown that for a perfectly aligned absorber intercept factor slightly decreases with an increase in slope error. It has also been found that the cumulative effect of both the absorber tube dislocation and slope error on the intercept factor is significant. Further, it is shown that the reduction in the intercept factor under influence of absorber tube misalignment and slope error is higher in case of 70 mm diameter absorber tube than 80 mm diameter absorber tube. The intercept

factor is found to be decreased by up to 11% with 70 mm diameter absorber tube when the absorber tube is dislocated by 15 mm in both directions and slope error is 3 mrad.

It is found that heat flux distribution over the absorber tube is slightly affected by the diameter of the absorber tube and slope error for the perfectly aligned receiver. In presence of slope error, the value of peak flux over the absorber tube increases with an increase in absorber tube dislocation in positive y-direction whereas the peak flux decreases with an increase in absorber tube dislocation in the negative y-direction.

Results have shown that the temperature gradient (the difference between the maximum and minimum temperature) on the surface of a perfectly aligned absorber tube is almost the same when slope error is 3 mrad. It is also found that the diameter of the absorber tube has no effect on the temperature gradient. Further, it has been shown that the temperature gradient is significantly affected by absorber tube dislocation with zero slope error and in the presence of slope error. It has been shown that temperature gradient is 59.7 K when $\Delta x = 15$ mm $\Delta y = +15$ mm $\sigma = 0$, whereas temperature gradient is 49 K when $\Delta x = 15$ mm, $\Delta y = +15$ mm $\sigma = 3$ mrad.

It can be concluded from results that thermal efficiency of the collector is not affected much by absorber tube dislocation in the presence of slope error. It has been found that thermal efficiency of collector reduces by up to 3% maximum with 70 mm diameter absorber tube when $\Delta x = 15$ mm $\Delta y = +15$ and slope error is zero. It is concluded that the effect of absorber tube misalignment on the overall collector efficiency is insignificant with zero slope error. However, in the presence of slope error and absorber tube misalignment, the

overall collector efficiency degrades significantly. Results have shown that maximum reduction in overall collector efficiency is 11% and 7% for the absorber tube diameters of 70 mm and 80 mm respectively.

In an approach to the enhancement of the heat transfer in the PTC receiver, numerical heat transfer simulations are performed on a PTC receiver with an un-finned absorber tube and absorber tubes with single longitudinal fin and two longitudinal fins. A detailed heat transfer analysis (including radiation) is carried out by considering the non-uniform heat flux over the absorber tube. The simulations have been performed for the range of Reynolds number from 0.25×10^5 to 2.82×10^5 .

The variation of Nusselt number and friction factor with Reynolds number is presented for the three absorber tubes. The variation of PEC with Reynolds number is also presented. PEC is used as a parameter to indicate the overall improvement in the heat transfer by taking care of both the Nusselt number and friction factor. It is found that the comprehensive heat transfer performance of the PTC is significantly improved with finned absorber tubes. However, a greater value of PEC is obtained for the absorber tube with two longitudinal fins than the absorber tube with single longitudinal fin. The maximum values of PEC obtained in the AT3 and AT2 are 1.28 and 1.19 respectively.

A rhombus tube absorber is proposed for parabolic trough collector, to improve the concentration ratio without affecting the intercept factor. Mathematical equations are developed to obtain the optimum size of rhombus tube absorber for the given trough dimensions (focal length, rim angle and acceptance angle). The concentration ratios for some of the existing commercial

collectors with rhombus tube absorber and circular tube absorber are calculated. It is concluded that the concentration ratio improves with rhombus tube absorber for all the collectors being considered.

A maximum gain of 31.5 percent is obtained in the concentration ratio at rim angle 90° for rhombus tube absorber in comparison to the circular absorber. As the rim angle decreases below 90° , the gain in concentration ratio also decreases and gain in CR is zero at rim angle 72.5° . Use of rhombus tube absorber is suggested for the values of rim angle between 72.5° to 90° preferably closer to 90° .

It is concluded that the reduction in the surface area of the absorber is 13.8% for the LS3 collector with rhombus tube. A maximum reduction of 23.9% in absorber surface area is obtained for Acurex collector with rhombus tube at rim angle 90° . The heat losses from the rhombus tube absorber may be reduced on account of the reduced surface area.

The concern may be about the installation of the rhombus tube in an evacuated glass tube in existing PTCs. The authors viewpoint is that it can easily be fitted in the glass tube with a little modification in glass-to-metal seals and metal bellows. Practical difficulties to be encountered in the installation of the rhombus tube are yet to be explored. Heat losses from rhombus tube absorber may be reduced due to a decrease in its surface area but pressure drop may be increased on account of higher fluid velocity. It is expected that the thermal performance of PTC system with rhombus tube absorber will improve but pumping power requirement will increase. A preliminary study presented in the present work suggests the employment of rhombus tube absorber to improve CR of the PTC system. However, the detailed thermal and flow analysis of the

PTC system with rhombus tube absorber may give more insight into the overall performance of the system. The detailed study about the thermal performance of the PTC with rhombus tube absorber may be the next phase of the research.

8.2 Future Research

In this study, the performance of the parabolic trough collector has been evaluated by considering the absorber tube misalignment and slope error. The tracking error is not been considered it can be considered in the future study. Two different types of longitudinal fin arrangements in the absorber tube of the PTC receiver has been studied. However, the optimization of sizes of longitudinal fins can be explored in the future study. Only the optical analysis of the parabolic trough collector with rhombus tube absorber tube has been presented in this study. The thermal analysis of the parabolic trough collector with rhombus tube collector can be carried out in the future for different operating conditions.

REFERENCES

1. Yan, J., et al., *Clean, efficient and affordable energy for a sustainable future*. Applied Energy, 2017. **185**: p. 953-962.
2. Jebasingh, V.K. and G.M.J. Herbert, *A review of solar parabolic trough collector*. Renewable and Sustainable Energy Reviews, 2016. **54**: p. 1085-1091.
3. Balat, M., *Solar Technological Progress and Use of Solar Energy in the World*. Energy Sources, Part A: Recovery, Utilization, and Environmental Effects, 2006. **28**(10): p. 979-994.
4. Yogi Goswami, D., *Solar Thermal Power Technology: Present Status and Ideas for the Future*. Energy Sources, 1998. **20**(2): p. 137-145.
5. Rabl, A., *Comparison of solar concentrators*. Solar Energy, 1976. **18**(2): p. 93-111.
6. Haddock, C. and J.S.C. McKee, *Solar Energy Collection, Concentration, and Thermal Conversion—A Review*. Energy Sources, 1991. **13**(4): p. 461-482.
7. Price, H., et al., *Advances in Parabolic Trough Solar Power Technology*. Journal of Solar Energy Engineering, 2002. **124**(2): p. 109-125.
8. <https://www.mtholyoke.edu/~wang30y/csp/PTPP.html>. [cited 2018 25/8].
9. <http://clui.org/ludb/site/kramer-junction-solar-electric-generating-station>. [cited 2018 25/8].
10. Rabl, A., *Active Solar Collectors and Their Applications*. 1985: Oxford University Press, New York.
11. <https://www.energy.gov/eere/solar/downloads/skytrough-parabolic-solar-collector>. [cited 2018 25/8].
12. Rodriguez-Sanchez, D. and G. Rosengarten, *Improving the concentration ratio of parabolic troughs using a second-stage flat mirror*. Applied Energy, 2015. **159**(Supplement C): p. 620-632.
13. <http://www.alternative-energy-tutorials.com/solar-hot-water/parabolic-trough-reflector.html>. [cited 2018 25/8].
14. Guven, H.M. and R.B. Bannerot, *Derivation of Universal Error Parameters for Comprehensive Optical Analysis of Parabolic Troughs*. Journal of Solar Energy Engineering, 1986. **108**: p. 275-281.
15. Bendt, P., et al., *Optical analysis and optimization of line focus solar collectors* SERI/TR 34-092 Solar Energy Research Institute, Golden CO., 1979.
16. Treadwell, G.W., *Design Considerations for Parabolic-Cylindrical Solar Collectors*, in *Sandia Laboratories*. 1976, Albuquerque: SAND76-0082.
17. Ratzel, A.C., *Receiver Assembly Design Studies for 2-m 90° Parabolic Cylindrical Solar Collectors*, in *Sandia Laboratories*. 1979, Albuquerque: SAND79-1026.
18. Pettit, R.B., C.N. Vittitoe, and F. Biggs, *Simplified Computational Procedure for Determining the Amount of Intercepted Sunlight in an Imaging Solar Concentrator*. Journal of Solar Energy Engineering, 1983. **105**(1): p. 101-107.

19. Forristall, R., *Heat Transfer Analysis and Modeling of a Parabolic Trough Solar Receiver Implemented in Engineering Equation Solver*. 2003: NREL Technical Report. p. 1-145.
20. Li, M. and L.L. Wang, *Investigation of evacuated tube heated by solar trough concentrating system*. Energy Conversion and Management, 2006. **47**(20): p. 3591-3601.
21. Kalogirou, S.A., et al., *Design and performance characteristics of a parabolic-trough solar-collector system*. Applied Energy, 1994. **47**(4): p. 341-354.
22. Mwesigye, A., et al., *Influence of optical errors on the thermal and thermodynamic performance of a solar parabolic trough receiver*. Solar Energy, 2016. **135**: p. 703-718.
23. Zhu, G., *Study of the Optical Impact of Receiver Position Error on Parabolic Trough Collectors*. Journal of Solar Energy Engineering, 2013. **135**(3): p. 031021.
24. Prah, C., et al., *Absorber tube displacement in parabolic trough collectors – A review and presentation of an airborne measurement approach*. Solar Energy, 2017. **157**: p. 692-706.
25. Hafez, A.Z., et al., *Design analysis of solar parabolic trough thermal collectors*. Renewable and Sustainable Energy Reviews, 2018. **82**(Part 1): p. 1215-1260.
26. Zhao, D., et al., *Influences of installation and tracking errors on the optical performance of a solar parabolic trough collector*. Renewable Energy, 2016. **94**: p. 197-212.
27. Khanna, S., S.B. Kedare, and S. Singh, *Analytical expression for circumferential and axial distribution of absorbed flux on a bent absorber tube of solar parabolic trough concentrator*. Solar Energy, 2013. **92**: p. 26-40.
28. Binotti, M., et al., *Geometric analysis of three-dimensional effects of parabolic trough collectors*. Solar Energy, 2013. **88**: p. 88-96.
29. Meiser, S., et al., *Evaluation and assessment of gravity load on mirror shape and focusing quality of parabolic trough solar mirrors using finite-element analysis*. Applied Energy, 2017. **185**: p. 1210-1216.
30. Mathur, S.S., et al., *Geometrical optical performance studies of a composite parabolic trough with a fin receiver*. Applied Energy, 1981. **9**(3): p. 223-229.
31. Thomas, A. and H.M. Guven, *Effect of optical errors on flux distribution around the absorber tube of a parabolic trough concentrator*. Energy Conversion and Management, 1994. **35**(7): p. 575-582.
32. Lüpfer, E., et al., *Parabolic Trough Optical Performance Analysis Techniques*. Journal of Solar Energy Engineering, 2007. **129**(2): p. 147.
33. Maccari, A. and M. Montecchi, *An optical profilometer for the characterisation of parabolic trough solar concentrators*. Solar Energy, 2007. **81**(2): p. 185-194.
34. García-Cortés, S., A. Bello-García, and C. Ordóñez, *Estimating intercept factor of a parabolic solar trough collector with new supporting structure using off-the-shelf photogrammetric equipment*. Applied Energy, 2012. **92**: p. 815-821.

35. Ulmer, S., et al., *Slope Error Measurements of Parabolic Troughs Using the Reflected Image of the Absorber Tube*. Journal of Solar Energy Engineering, 2009. **131**(1): p. 011014.
36. Skouri, S., et al., *Optical, geometric and thermal study for solar parabolic concentrator efficiency improvement under Tunisia environment: A case study*. Energy Conversion and Management, 2013. **75**: p. 366-373.
37. Balghouthi, M., et al., *Optical and thermal evaluations of a medium temperature parabolic trough solar collector used in a cooling installation*. Energy Conversion and Management, 2014. **86**: p. 1134-1146.
38. Gaul, H. and A. Rabl, *Incidence-Angle Modifier and Average Optical Efficiency of Parabolic Trough Collectors*. Journal of Solar Energy Engineering, 1980. **102**(1): p. 16-21.
39. Ren, L., et al., *A review of available methods for the alignment of mirror facets of solar concentrator in solar thermal power system*. Renewable and Sustainable Energy Reviews, 2014. **32**: p. 76-83.
40. Khanna, S. and V. Sharma, *Explicit Analytical Expression for Solar Flux Distribution on an Undelected Absorber Tube of Parabolic Trough Concentrator Considering Sun-Shape and Optical Errors*. Journal of Solar Energy Engineering, 2015. **138**(1): p. 011010-011010.
41. Geyer, M., et al. *EUROTROUGH-parabolic trough collector developed for cost efficient solar power generation*. in *Proceedings of the 11th SolarPACES Conference*. 2002. Zurich, Switzerland.
42. Iverson, B.D., S.M. Flueckiger, and B.D. Ehrhart, *Trough heat collection element deformation and solar intercept impact*, in *Proceedings of the 17th SolarPACES Conference*. 2011: Granada, Spain. p. 20–23.
43. Wu, Z., et al., *Structural reliability analysis of parabolic trough receivers*. Applied Energy, 2014. **123**: p. 232-241.
44. Stynes, K. and B. Ihas, *Absorber alignment measurement tool for solar parabolic trough collectors*, in *ASME 2012 6th International Conference on Energy Sustainability 2012*, American Society of Mechanical Engineers. p. 437–447.
45. Heller, P., et al., *KONTAS—a rotary test bench for standardized qualification of parabolic trough components.*, in *Proceedings of the 17th SolarPACES Conference*. 2011: Granada, Spain. p. 20–23.
46. Lüpfert, E., et al., *Parabolic Trough Optical Performance Analysis Techniques*. Journal of Solar Energy Engineering, 2006. **129**(2): p. 147-152.
47. Mousazadeh, H., et al., *A review of principle and sun-tracking methods for maximizing solar systems output*. Renewable and Sustainable Energy Reviews, 2009. **13**(8): p. 1800-1818.
48. Treadwell, G.W. and N.R. Grandjean, *Systematic Rotation and Receiver Location Error Effects on Parabolic Trough Annual Performance*. Journal of Solar Energy Engineering, 1982. **104**(4): p. 345-348.
49. Wang, P., D.Y. Liu, and C. Xu, *Numerical study of heat transfer enhancement in the receiver tube of direct steam generation with*

- parabolic trough by inserting metal foams*. Applied Energy, 2013. **102**: p. 449-460.
50. Reddy, K.S., K.R. Kumar, and G.V. Satyanarayana, *Numerical Investigation of Energy-Efficient Receiver for Solar Parabolic Trough Concentrator*. Heat Transfer Engineering, 2008. **29**(11): p. 961-972.
 51. Bellos, E. and C. Tzivanidis, *Assessment of the thermal enhancement methods in parabolic trough collectors*. International Journal of Energy and Environmental Engineering, 2018. **9**(1): p. 59-70.
 52. Fuqiang, W., et al., *Heat transfer performance enhancement and thermal strain restrain of tube receiver for parabolic trough solar collector by using asymmetric outward convex corrugated tube*. Energy, 2016. **114**: p. 275-292.
 53. Bellos, E., C. Tzivanidis, and D. Tsimpoukis, *Multi-criteria evaluation of parabolic trough collector with internally finned absorbers*. Applied Energy, 2017. **205**: p. 540-561.
 54. Cheng, Z.D., Y.L. He, and F.Q. Cui, *Numerical study of heat transfer enhancement by unilateral longitudinal vortex generators inside parabolic trough solar receivers*. International Journal of Heat and Mass Transfer, 2012. **55**(21): p. 5631-5641.
 55. Gong, X., et al., *Heat transfer enhancement analysis of tube receiver for parabolic trough solar collector with pin fin arrays inserting*. Solar Energy, 2017. **144**: p. 185-202.
 56. Collares-Pereira, M., et al., *High concentration two-stage optics for parabolic trough solar collectors with tubular absorber and large rim angle*. Solar Energy, 1991. **47**(6): p. 457-466.
 57. Brunotte, M., A. Goetzberger, and U. Blieske, *Two-stage concentrator permitting concentration factors up to 300x with one-axis tracking*. Solar Energy, 1996. **56**(3): p. 285-300.
 58. Omer, S.A. and D.G. Infield, *Design and thermal analysis of a two stage solar concentrator for combined heat and thermoelectric power generation*. Energy Conversion and Management, 2000. **41**(7): p. 737-756.
 59. O'Gallagher, J. and R. Winston, *Performance model for two-stage optical concentrators for solar thermal applications*. Solar Energy, 1988. **41**(4): p. 319-325.
 60. Bakos, G.C., et al., *Design, optimisation and conversion-efficiency determination of a line-focus parabolic-trough solar-collector (PTC)*. Applied Energy, 2001. **68**(1): p. 43-50.
 61. McIntire, W.R., *Secondary concentration for linear focusing systems: a novel approach*. Applied Optics, 1980. **19**(18): p. 3036-3037.
 62. Friedman, R.P., J.M. Gordon, and H. Ries, *New high-flux two-stage optical designs for parabolic solar concentrators*. Solar Energy, 1993. **51**(5): p. 317-325.
 63. Wirz, M., et al., *Potential improvements in the optical and thermal efficiencies of parabolic trough concentrators*. Solar Energy, 2014. **107**: p. 398-414.
 64. Gordon, J.M. and D. Feuermann, *Optical performance at the thermodynamic limit with tailored imaging designs*. Applied Optics, 2005. **44**(12): p. 2327-2331.

65. Ostroumov, N., J.M. Gordon, and D. Feuermann, *Panorama of dual-mirror aplanats for maximum concentration*. Applied Optics, 2009. **48**(26): p. 4926-4931.
66. Jeter, S.M., *Calculation of the concentrated flux density distribution in parabolic trough collectors by a semifinite formulation*. Solar Energy, 1986. **37**(5): p. 335-345.
67. Jeter, S.M., *Analytical determination of the optical performance of practical parabolic trough collectors from design data*. Solar Energy, 1987. **39**(1): p. 11-21.
68. Delatorre, J., et al., *Monte Carlo advances and concentrated solar applications*. Solar Energy, 2014. **103**: p. 653-681.
69. Cheng, Z.D., et al., *Three-dimensional numerical study of heat transfer characteristics in the receiver tube of parabolic trough solar collector*. International Communications in Heat and Mass Transfer, 2010. **37**(7): p. 782-787.
70. He, Y.-L., et al., *A MCRT and FVM coupled simulation method for energy conversion process in parabolic trough solar collector*. Renewable Energy, 2011. **36**(3): p. 976-985.
71. Cheng, Z.D., et al., *Numerical simulation of a parabolic trough solar collector with nonuniform solar flux conditions by coupling FVM and MCRT method*. Solar Energy, 2012. **86**(6): p. 1770-1784.
72. Ghomrassi, A., H. Mhiri, and P. Bournot, *Numerical Study and Optimization of Parabolic Trough Solar Collector Receiver Tube*. Journal of Solar Energy Engineering, 2015. **137**(5): p. 051003.
73. Wang, F., et al., *Thermal stress analysis of eccentric tube receiver using concentrated solar radiation*. Solar Energy, 2010. **84**(10): p. 1809-1815.
74. Roesle, M., V. Coskun, and A. Steinfeld, *Numerical Analysis of Heat Loss From a Parabolic Trough Absorber Tube With Active Vacuum System*. Journal of Solar Energy Engineering, 2011. **133**(3): p. 031015-031015.
75. Wirz, M., M. Roesle, and A. Steinfeld, *Three-Dimensional Optical and Thermal Numerical Model of Solar Tubular Receivers in Parabolic Trough Concentrators*. Journal of Solar Energy Engineering, 2012. **134**(4): p. 041012.
76. Wu, Z., et al., *Three-dimensional numerical study of heat transfer characteristics of parabolic trough receiver*. Applied Energy, 2014. **113**: p. 902-911.
77. Tim, W. and D. Aron, *SolTrace: A Ray-Tracing Code for Complex Solar Optical Systems*. 2013, ST11.3070.
78. Cheng, Z.D., Y.L. He, and F.Q. Cui, *A new modelling method and unified code with MCRT for concentrating solar collectors and its applications*. Applied Energy, 2013. **101**: p. 686-698.
79. Cheng, Z.-D., X.-R. Zhao, and Y.-L. He, *Novel optical efficiency formulas for parabolic trough solar collectors: Computing method and applications*. Applied Energy, 2018. **224**: p. 682-697.
80. Thomas, A. and S.A. Thomas, *Design data for the computation of thermal loss in the receiver of a parabolic trough concentrator*. Energy Conversion and Management, 1994. **35**(7): p. 555-568.

81. Odeh, S.D., G.L. Morrison, and M. Behnia, *Modelling of parabolic trough direct steam generation solar collectors*. Solar Energy, 1998. **62**(6): p. 395-406.
82. Liang, H., S. You, and H. Zhang, *Comparison of different heat transfer models for parabolic trough solar collectors*. Applied Energy, 2015. **148**: p. 105-114.
83. Burkholder, F. and C. Kutscher, *Heat loss testing of Schott's 2008 PTR70 parabolic trough receiver*. 2009, NREL Technical Report: NREL/TP - 550-45633. p. 1-58.
84. Burkholder, F. and C. Kutscher, *Heat-loss testing of Solel's UVAC3 parabolic trough receiver*. 2008, NREL Technical Report: NREL/TP - 550-42394. p. 1-19.
85. Padilla, R.V., et al., *Heat transfer analysis of parabolic trough solar receiver*. Applied Energy, 2011. **88**(12): p. 5097-5110.
86. Kalogirou, S.A., *A detailed thermal model of a parabolic trough collector receiver*. Energy, 2012. **48**(1): p. 298-306.
87. Yang, S., T.S. Sensoy, and J.C. Ordonez, *Dynamic 3D volume element model of a parabolic trough solar collector for simulation and optimization*. Applied Energy, 2018. **217**: p. 509-526.
88. Moghimi, M.A., K.J. Craig, and J.P. Meyer, *A novel computational approach to combine the optical and thermal modelling of Linear Fresnel Collectors using the finite volume method*. Solar Energy, 2015. **116**: p. 407-427.
89. Behar, O., A. Khellaf, and K. Mohammedi, *A novel parabolic trough solar collector model – Validation with experimental data and comparison to Engineering Equation Solver (EES)*. Energy Conversion and Management, 2015. **106**: p. 268-281.
90. Dudley, E.V., et al., *Test results: SEGS LS-2 solar collector*. 1994, Sandia National Laboratory Report: SAND94-1884.
91. Li, Z.-Y., Z. Huang, and W.-Q. Tao, *Three-dimensional numerical study on fully-developed mixed laminar convection in parabolic trough solar receiver tube*. Energy, 2016. **113**: p. 1288-1303.
92. Liang, H., et al., *A Monte Carlo method and finite volume method coupled optical simulation method for parabolic trough solar collectors*. Applied Energy, 2017. **201**: p. 60-68.
93. Chang, C., et al., *Enhanced heat transfer in a parabolic trough solar receiver by inserting rods and using molten salt as heat transfer fluid*. Applied Energy, 2018. **220**: p. 337-350.
94. Mwesigye, A., T. Bello-Ochende, and J.P. Meyer, *Numerical investigation of entropy generation in a parabolic trough receiver at different concentration ratios*. Energy, 2013. **53**: p. 114-127.
95. ANSYS, *ANSYS Fluent Theory Guide*. 2016b, ANSYS Inc: ANSYS Inc.
96. ANSYS, *ANSYS Fluent User's Guide*. 2016a: ANSYS Inc.
97. Shih, T.-H., et al., *A New K-epsilon Eddy Viscosity Model for High Reynolds Number Turbulent Flows: Model Development and Validation*. Computers Fluids, 1995(24(3)): p. 227-238.
98. ANSYS, *ANSYS Fluent UDF Manual*. 2016c, ANSYS Inc.: ANSYS Inc.

99. Mullick, S.C. and S.K. Nanda, *An improved technique for computing the heat loss factor of a tubular absorber*. Solar Energy, 1989. **42**(1): p. 1-7.
100. ANSYS, *ANSYS ICEM CFD User's Manual*. 2016d, ANSYS Inc.: ANSYS Inc.
101. Neumann, A., et al., *Representative Terrestrial Solar Brightness Profiles*. Journal of Solar Energy Engineering, 2002. **124**(2): p. 198.
102. Eck, M. and W.D. Steinmann, *Direct Steam Generation in Parabolic Troughs: First Results of the DISS Project*. Journal of Solar Energy Engineering, 2002. **124**(2): p. 134-139.
103. Wendelin, T., *Parabolic trough VSHOT optical characterization in 2005-2006 [electronic resource] / Tim Wendelin*. NREL (PR) ; 550-40024., ed. E. United States. Department of Energy. Office of Energy, et al. 2006, [Washington, D.C.] : [Golden, Colo.]: U.S. Dept. of Energy, Energy Efficiency and Renewable Energy ; National Renewable Energy Laboratory.
104. Wang, S., Z.Y. Guo, and Z.X. Li, *Heat transfer enhancement by using metallic filament insert in channel flow*. International Journal of Heat and Mass Transfer, 2001. **44**(7): p. 1373-1378.
105. Benitez, R.W.J.M.P., *Nonimaging optics*. 2005.
106. Güven, H.M. and R.B. Bannerot, *Determination of error tolerances for the optical design of parabolic troughs for developing countries*. Solar Energy, 1986. **36**(6): p. 535-550.